

## **INFORMATION TO USERS**

**This manuscript has been reproduced from the microfilm master. UMI films the text directly from the original or copy submitted. Thus, some thesis and dissertation copies are in typewriter face, while others may be from any type of computer printer.**

**The quality of this reproduction is dependent upon the quality of the copy submitted. Broken or indistinct print, colored or poor quality illustrations and photographs, print bleedthrough, substandard margins, and improper alignment can adversely affect reproduction.**

**In the unlikely event that the author did not send UMI a complete manuscript and there are missing pages, these will be noted. Also, if unauthorized copyright material had to be removed, a note will indicate the deletion.**

**Oversize materials (e.g., maps, drawings, charts) are reproduced by sectioning the original, beginning at the upper left-hand corner and continuing from left to right in equal sections with small overlaps. Each original is also photographed in one exposure and is included in reduced form at the back of the book.**

**Photographs included in the original manuscript have been reproduced xerographically in this copy. Higher quality 6" x 9" black and white photographic prints are available for any photographs or illustrations appearing in this copy for an additional charge. Contact UMI directly to order.**

# **UMI**

**A Bell & Howell Information Company  
300 North Zeeb Road, Ann Arbor MI 48106-1346 USA  
313/761-4700 800/521-0600**



# **Durability of Polymeric Composites After Elevated Temperature Aging**

by

Eric L. Poole

A dissertation submitted in partial fulfillment  
of the requirements for the degree of

Doctor of Philosophy

University of Washington

1997

Approved by \_\_\_\_\_



(Chairperson of the Supervisory Committee)

Program Authorized  
to Offer Degree \_\_\_\_\_

Department of Aeronautics and Astronautics

Date \_\_\_\_\_

January 17, 1997

**UMI Number: 9730065**

---

**UMI Microform 9730065**  
**Copyright 1997, by UMI Company. All rights reserved.**

**This microform edition is protected against unauthorized  
copying under Title 17, United States Code.**

---

**UMI**  
**300 North Zeeb Road**  
**Ann Arbor, MI 48103**

In presenting this dissertation in partial fulfillment of the requirements for the Doctoral degree at the University of Washington, I agree that the Library shall make its copies freely available for inspection. I further agree that extensive copying of this dissertation is allowable only for scholarly purposes, consistent with "fair use" as prescribed in the U. S. Copyright Law. Requests for copying or reproduction of this dissertation may be referred to University Microfilms, 1490 Eisenhower Place, P. O. Box 975, Ann Arbor MI 48106, to whom the author has granted "the right to reproduce and sell (a) copies of the manuscript in microform and/or (b) printed copies of the manuscript made from microform."

Signature *C. J. Roll*

Date *January 17, 1997*

University of Washington

Abstract

**Durability of Polymeric Composites After  
Elevated Temperature Aging**

by Eric L. Poole

Chairperson of the Supervisory Committee: Professor Kuen Y. Lin

Department of Aeronautics and Astronautics

The Compression After Impact (CAI) strength of polymeric composites after long term elevated temperature aging is studied. Aging temperatures range from 149°C to 204°C (300°F to 400°F). Two types of matrix material are studied, a thermoset bismaleimide (5260) and a thermoplastic polyimide (K3B). Glass transition temperature ( $T_g$ ) and fracture toughness are measured after aging. Microscopy and Secondary Ion Mass Spectroscopy (SIMS) are used to evaluate the aged composites. Out-of-plane bending of the CAI specimens during compression is measured by shadow moiré. Moiré interferometry is used to determine in-plane displacement and strain fields around the impact damage.

Results show that the CAI strength degrades with aging for both K3B and 5260. The 5260 matrix suffers from thermo-oxidative degradation at higher temperatures. Surface decomposition causes weight loss and reduces mechanical properties. The CAI strength of the K3B matrix composite also decreases after aging. Evidence of an oxidation reaction is found in the K3B polymer by SIMS, but no weight loss is associated with this chemical reaction. Measured changes in fracture toughness and  $T_g$  do not correlate with CAI strength degradation. Stiffness changes due to aging are insignificant in this study.

The degradation region is measured by microscopy near the surface of composites after long aging times. The depth of the degradation zone is dependent on aging time. Degradation growth is modeled with finite elements using diffusion/reaction governing equations. Finite element results agree well with the experimental data.

# TABLE OF CONTENTS

<b>List of Figures</b>	<b>iv</b>
<b>List of Tables</b>	<b>viii</b>
<b>Chapter 1 Introduction</b>	<b>1</b>
1.1 Motivation	1
1.2 Background	3
<b>Chapter 2 Aging of Polymeric Materials</b>	<b>7</b>
2.1 Processing of polymeric materials	7
2.2 Physical aging	11
2.3 Chemical aging	12
<b>Chapter 3 Material Properties Testing</b>	<b>16</b>
3.1 Fracture toughness	17
3.1.1 Mode I fracture toughness	20
3.1.2 Mode II fracture toughness	32
3.2 Microscopy studies	34
3.3 Discoloration depth in aged composites	38
3.4 Glass transition temperature	44
3.5 ESCA analysis	46
3.6 TOF-SIMS tests	47
3.7 Four point bend strength	53
<b>Chapter 4 Diffusion/Reaction Model</b>	<b>56</b>
4.1 Formulation using conservation of mass	56
4.1.1 Analytical solution	56
4.1.2 Experimental parameters	61

4.2	Finite element model	64
4.2.1	Governing equations	64
4.2.2	Finite element formulation	67
4.2.3	Modeling results	71
<b>Chapter 5 Compression After Impact Strength Theories</b>		<b>76</b>
5.1	Impact damage	77
5.1.1	Impact modeling	77
5.1.2	Damage characterization	78
5.2	Sublaminar stability	81
5.3	Failure criteria	83
5.3.1	Delamination growth	83
5.3.2	Localized strength failure	83
<b>Chapter 6 Compression After Impact Strength Testing</b>		<b>85</b>
6.1	Failure strength	85
6.1.1	Experimental procedure	85
6.1.2	Results from unaged specimens	96
6.1.3	CAI strength of aged specimens	100
6.1.4	Impact damage in aged specimens	109
6.2	Out-of-plane displacement	113
6.2.1	Results of shadow moiré testing	113
6.2.2	Specimen bending	116
6.3	Near damage strain fields	119
<b>Chapter 7 Aging Effects on Compression After Impact Strength</b>		<b>123</b>
7.1	Post-cure of the matrix material	123
7.2	Matrix stiffness changes	124
7.3	Changes in impact resistance	124
7.4	Changes in fracture toughness	125
7.5	Oxidation zone growth	126
7.6	Ply failure strength degradation	127

<b>Chapter 8 Conclusions and Recommendations</b>	<b>130</b>
8.1 Material properties testing	131
8.2 CAI strength	132
8.3 Compression strength of sandwich panels	133
<b>Bibliography</b>	<b>134</b>
<b>Appendix A Shadow Moiré</b>	<b>142</b>
<b>Appendix B Moiré Interferometry</b>	<b>145</b>
B.1 Theoretical background	145
B.2 Experimental procedure	150
<b>Appendix C Finite Element Subroutines</b>	<b>156</b>
C.1 One dimensional degradation	156
C.2 Two dimensional degradation	159

## LIST OF FIGURES

Figure 1.1	Conceptual drawing of the High Speed Civil Transport .....	3
Figure 2.1	Example of a monomer and the resulting polymer molecule.....	7
Figure 2.2	Condensation polymerization of K3B .....	10
Figure 2.3	Cure cycle for IM7/K3B composite materials .....	10
Figure 2.4	Chain scission due to photo-oxidation .....	13
Figure 3.1	Modes of crack propagation .....	17
Figure 3.2	Schematic diagram of fracture toughness specimens.....	18
Figure 3.3	DCB testing of mode I fracture toughness .....	21
Figure 3.4	Load-displacement curves for a DCB test .....	22
Figure 3.5	$G_{Ic}$ for a DCB test using various calculation methods .....	23
Figure 3.6	Scanning electron micro-graph of fiber bridging .....	24
Figure 3.7	$G_{Ic}$ as a function of crack extension .....	25
Figure 3.8	$G_{Ic}$ for unaged IM7/5260 .....	26
Figure 3.9	$G_{Ic}$ for unaged IM7/K3B .....	26
Figure 3.10	$G_{Ic}$ at the crack tip of aged IM7/5260 specimens .....	28
Figure 3.11	Comparison of aged and unaged DCB data for IM7/5260 ....	28
Figure 3.12	$G_{Ic}$ in the interior of aged IM7/5260 specimens .....	29
Figure 3.13	$G_{Ic}$ at the crack tip of aged IM7/K3B specimens .....	31
Figure 3.14	$G_{Ic}$ of the interior of aged IM7/K3B specimens .....	31
Figure 3.15	Comparison of aged and unaged DCB data for IM7/K3B ....	32
Figure 3.16	$G_{IIc}$ for unaged IM7/K3B .....	33
Figure 3.17	Mode I and II fracture surfaces of IM7/K3B .....	35
Figure 3.18	Tool surfaces of unaged and aged IM7/5260 .....	35
Figure 3.19	End surfaces of unaged and aged IM7/K3B .....	36
Figure 3.20	Cross section of unaged and aged IM7/5260 .....	36
Figure 3.21	Discolored region in IM7/K3B aged at 149°C .....	37
Figure 3.22	Discolored region in IM7/K3B aged at 204°C .....	37
Figure 3.23	Fracture surface of an aged ENF specimen .....	38

Figure 3.24	Discoloration depth parallel to the fibers in IM7/5260 .....	40
Figure 3.25	Discoloration depth transverse to the fibers in IM7/5260 ....	40
Figure 3.26	Discoloration depth parallel to the fibers in IM7/K3B .....	42
Figure 3.27	Discoloration depth transverse to the fibers in IM7/K3B ....	42
Figure 3.28	Degradation around an open hole in IM7/5260 .....	43
Figure 3.29	Glass transition temperature for IM7/5260 .....	45
Figure 3.30	Glass transition temperature for IM7/K3B .....	45
Figure 3.31	Typical SIMS spectrum for unaged IM7/K3B .....	48
Figure 3.32	Chemical structure of K3B monomer .....	49
Figure 3.33	Chemical structure of secondary ions in K3B .....	49
Figure 3.34	Scan of high mass groups on an unaged mode II surface ....	51
Figure 3.35	Scan of high mass groups on an aged mode II surface .....	52
Figure 3.36	Schematic diagram of four point bend testing .....	53
Figure 3.37	Degradation of compressive strength in four point bend specimens aged at 149°C .....	54
Figure 3.38	Degradation of compressive strength in four point bend specimens aged at 204°C .....	55
Figure 4.1	Concentration of diffused oxygen at the surface of an aged polymeric composite .....	57
Figure 4.2	Temperature dependence for the reaction rate of thermo- oxidative degradation parallel to the fibers in IM7/5260 ....	62
Figure 4.3	Temperature dependence for the reaction rate of thermo- oxidative degradation parallel to the fibers in IM7/K3B ....	63
Figure 4.4	Differential element within the material .....	66
Figure 4.5	Profile of diffused oxygen saturation near the surface .....	72
Figure 4.6	Degradation along the fibers in IM7/5260 aged at 204°C ...	72
Figure 4.7	Degradation transverse to the fibers in IM7/5260 aged at 204°C .....	73
Figure 4.8	Degradation along the fibers in IM7/K3B aged at 204°C ....	73
Figure 4.9	Degradation transverse to the fibers in IM7/K3B aged at 204°C .....	74
Figure 4.10	Interior ply of an aged open hole specimen .....	75
Figure 4.11	Degradation boundary around an open hole from FEM .....	75

Figure 5.1	Strain fields, principal strains, and crack propagation for an element in the K-rule damage analysis .....	79
Figure 5.2	K-rule prediction of delamination region connecting two different ply elements with transverse cracks .....	79
Figure 5.3	Delaminations between plies of a (45/0/-45/90) <sub>3s</sub> laminate ..	80
Figure 5.4	Reduced modulus calculation and simulated damage zone used in the sublaminates stability model .....	82
Figure 5.5	Edgewise view of compression failure in the 0° ply .....	84
Figure 6.1	$\Delta T_g$ used to select aging times for IM7/5260 .....	86
Figure 6.2	Image of loss of back signal for an impacted laminate .....	91
Figure 6.3	Damage area idealization from loss of back signal .....	91
Figure 6.4	Internal signal from C-scan with time-of-flight .....	92
Figure 6.5	Test fixture for CAI specimens .....	94
Figure 6.6	Typical CAI stress-strain data .....	95
Figure 6.7	Failure stress for CAI specimens with zero aging .....	96
Figure 6.8	Damage diameter for CAI specimens with zero aging .....	98
Figure 6.9	CAI failure stress versus damage width .....	98
Figure 6.10	Damage before and after loading to 90% of failure .....	99
Figure 6.11	CAI failure stress for IM7/5260 specimens aged at 149°C	101
Figure 6.12	CAI failure stress for IM7/5260 specimens aged at 177°C	103
Figure 6.13	CAI failure stress for IM7/5260 specimens aged at 204°C	104
Figure 6.14	CAI failure stress for IM7/K3B specimens aged at 149°C	106
Figure 6.15	CAI failure stress for IM7/K3B specimens aged at 177°C	107
Figure 6.16	CAI failure stress for IM7/K3B specimens aged at 204°C	108
Figure 6.17	Damage area for IM7/5260 specimens impacted with 22.6 J of energy after aging .....	110
Figure 6.18	Example of symmetric and asymmetric damage .....	111
Figure 6.19	Damage area for IM7/K3B specimens impacted after aging at 177°C .....	112
Figure 6.20	Shadow moiré fringes of a CAI specimen near failure .....	114
Figure 6.21	Loading sequence showing outer ply buckling in IM7/5260 .....	115
Figure 6.22	Out-of-plane deflection along the centerline of a CAI specimen near failure .....	116

<b>Figure 6.23</b>	<b>Center deflection during loading of CAI specimens .....</b>	<b>118</b>
<b>Figure 6.24</b>	<b>Strains near the impact damage during loading .....</b>	<b>118</b>
<b>Figure 6.25</b>	<b>Axial strains for an IM7/K3B CAI specimen at 80% of failure stress, measured by moiré interferometry .....</b>	<b>121</b>
<b>Figure 6.26</b>	<b>Axial strains for an IM7/K3B CAI specimen at 80% of failure stress, calculated by finite element methods .....</b>	<b>122</b>
<b>Figure 7.1</b>	<b>Normalized failure strength for IM7/5260 CAI and four point bend specimens .....</b>	<b>128</b>
<b>Figure 7.2</b>	<b>Normalized failure strength for IM7/K3B CAI and four-point-bend specimens .....</b>	<b>129</b>
<b>Figure A.1</b>	<b>Diagram of shadow moiré .....</b>	<b>144</b>
<b>Figure B.1</b>	<b>Regions of constructive and destructive interference in space where two coherent beams intersect .....</b>	<b>147</b>
<b>Figure B.2</b>	<b>Two beam interference resulting from diffraction of incident beams which produces the moiré image .....</b>	<b>149</b>
<b>Figure B.3</b>	<b>Optical generation of a mold for producing specimen gratings .....</b>	<b>151</b>
<b>Figure B.4</b>	<b>Steps in transferring the thin metallic grating to the specimen surface .....</b>	<b>152</b>
<b>Figure B.5</b>	<b>Positioning of optical equipment used for moiré measurement of in-plane and out-of-plane displacement fields .....</b>	<b>154</b>
<b>Figure B.6</b>	<b>Displacement fringes and the resulting strain field .....</b>	<b>155</b>

## **LIST OF TABLES**

<b>Table 3.1</b>	<b>Fracture toughness test matrix for IM7/5260 .....</b>	<b>19</b>
<b>Table 3.2</b>	<b>Fracture toughness test matrix for IM7/K3B.....</b>	<b>19</b>
<b>Table 4.1</b>	<b>Experimental parameters for degradation growth .....</b>	<b>62</b>
<b>Table 4.2</b>	<b>FEM parameters for 1-D degradation growth .....</b>	<b>71</b>
<b>Table 6.1</b>	<b>Test matrix for CAI testing of IM7/5260 .....</b>	<b>88</b>
<b>Table 6.2</b>	<b>Test matrix for CAI testing of IM7/K3B .....</b>	<b>88</b>

## ACKNOWLEDGMENTS

I wish to express my sincerest thanks to Professor Kuen Y. Lin, committee chairman, for his assistance, support, and guidance throughout the course of this research project. His knowledgeable help has shown me how to work effectively on this project and will be a guide for projects to come. Professor Mark Tuttle has also provided advice throughout my research at the University of Washington, and I thank him for his assistance. I would like to thank Professor Keith Holsapple for his help in finite element modeling and Professor Buddy Ratner for his consultation on chemical analysis.

I would like to acknowledge Craig Barwell, Rufeng Li, and Scott Carpenter for their work and discussions which contributed to the project. Also, John Williams and Patrick Headstrom, for the many hours of tedious labor they contributed.

This work was supported by Boeing and NASA. I thank Patrick Roark and Eric Cregger for their exceptional support and benevolent supervision. Their efforts to smoothly administer the ongoing effort were greatly appreciated.

Finally, I wish to express my deepest gratitude to my wife, Jamie, and son, Emery. Jamie was instrumental in the completion of this dissertation, providing understanding and giving me unconditional love throughout. With his exuberance and inquisitive mind, Emery supplied a constant source of joy.

## Chapter 1

# INTRODUCTION

### 1.1 Motivation

The advantages of using composite materials are well known by design engineers in every area of manufacturing. Composite materials are defined as any material that consists of two distinct constituent materials. The advantage of composites is that the beneficial aspects of distinctly different materials can be incorporated, while the detrimental aspects of the constituent materials are diminished. This process is generally more difficult than using a homogenous material would be, but the benefits often justify the required additional effort.

In the aerospace industry, the most common composite materials are continuous fiber reinforced plastics (CFRP's). The stiffness and strength of the material is provided by the continuous fibers, most commonly made from glass, graphite or boron. Thousands of these fibers, smaller in diameter than a human hair, are held together into a structural entity by the 'plastic,' or matrix material. The graphite fibers are stiffer and stronger along their length than the commonly used aluminum alloys. The graphite fibers are even stiffer than titanium, while having a comparable strength and much lower density. When the fibers are embedded in a matrix material, the unidirectional CFRP's have roughly twice the specific strength of steel or titanium, and over three times greater specific stiffness [1]. These higher properties translate directly into substantially reduced weight for the structure, an obviously beneficial gain for aerospace applications.

The superiority noted above is for properties of unidirectional composites along the axis parallel to the fibers. A unidirectional composite has all fibers aligned in the same direction. In such a configuration, the properties perpendicular to the fiber will be drastically lower than for the

isotropic metals. Completely unidirectional structures are not used in practice because of the poor transverse properties, but strength and stiffness can be tailored to correspond to the principal loading directions.

The use of CFRP's in U. S. aircraft dates back to around 1970. Demonstration components made of boron/epoxy were flown and, once proven, incorporated into the production of both the F-14 and F-15. After this, graphite/epoxy replaced boron/epoxy because of the high cost of boron composites, but the use of CFRP's continued to grow. In the F-16, graphite/epoxy accounts for 3% of the structural weight, the F/A-18 9%, and the structure of the AV-8B contains 26% CFRP's by weight [2]. Commercial aircraft have lagged behind military aircraft in terms of the percentage of CFRP structure, but are following a similar trend.

Early use of composites in aircraft was limited to secondary structure. These are components which do not carry large loads, such as elevators, ailerons, rudders and other aerodynamic surfaces. Even though the advantages of using CFRP's were readily apparent, the difficulties associated with the new systems and a lack of knowledge about their reliability limited their use. Only after experience was gained did designers make use of composites in primary, load bearing, structure beginning with the tail of the aircraft. The role of CFRP's in aerospace structures continues to grow in incremental steps. However, most modern aircraft are still primarily constructed from aluminum alloys.

For the next generation of supersonic passenger aircraft, polymeric composites are candidate materials for use in the entire structure. The Boeing Company is currently conducting a program to develop a supersonic aircraft, called the High Speed Civil Transport (HSCT). A conceptual drawing is presented in Figure 1.1. A design for this aircraft using primarily aluminum alloys was analyzed and found unacceptable. The weight of the aircraft needed to be reduced. A joint research effort is being conducted by NASA, Boeing, and other industry partners to provide the understanding necessary to build a lightweight structure entirely of composite materials. This research is a part of that effort.



Figure 1.1 Conceptual drawing of the High Speed Civil Transport

## 1.2 Background

Elastic and visco-elastic response of polymeric composite structures can be modeled with very good accuracy during loading, even with the considerable number of variables associated with each composite. A set of variables for a composite includes elastic stiffness and failure strength variables for each constituent material, coefficients of thermal expansion, visco-elastic parameters for the polymer, cure cycle for the polymer, void content, fiber fraction, fiber waviness, and laminate stacking sequence. Extensive research has gone into understanding the behavior of composite structures under operating conditions, and a general theory has been established.

The main drawback of these materials has been the lack of predictability in fatigue and failure. The complex, heterogeneous internal structure leads to complex failure mechanisms that are difficult to measure or predict. A single fiber failure is generally of no concern, since load will be transferred to the surrounding fibers. Intraply cracking will only be a problem in areas of high shear. Delaminations between plies cause problems only if they are large enough to lead to a buckling instability. Under very high loads, these small failures absorb energy and relieve strain concentrations on the local scale. Continued loading of the structure will cause an increasing number of local failures until the small failures coalesce into a large scale component failure. Predicting the exact failure load is difficult, because each individual component can fail in a slightly different way. Most theories are based on average, or 'smeared,' properties across the thickness of individual plies. Average values can thus be predicted accurately. But the scatter in failure data limits engineers to using conservative designs, reducing the weight savings and cost effectiveness of polymeric composites.

Another aspect of the use of polymeric composites in the HSCT is that the composite structural components are exposed to elevated temperature environments. Because of stagnation heating caused by the Mach 2.4 cruise, the skin of the aircraft will be exposed to temperatures in the range of 122°C to 177°C. Exposure times will reach 60,000 hours over the life of the aircraft. Under these conditions the polymeric matrix material may undergo chemical and physical changes, or 'aging', resulting in property degradation. The degradation process must be well understood for all candidate materials before they can be used in the production aircraft. Ideally, the properties of the composite after 60,000 hours should be predicted after only a short duration of aging, so that new materials can be screened quickly as they are produced.

One important aspect of composite durability is the Compression After Impact (CAI) strength of a laminate or sandwich panel. A laminate is a stack of individual polymeric composite plies, formed into a single structure

by a curing process. A sandwich panel is formed from two laminates with a lighter but softer core material between them, again joined by a curing process. These structures are particularly susceptible to large reductions in compression strength, because of the tendency for delaminations to occur between the plies after an impact perpendicular to the surface. These delaminations buckle at lower compressive strains than the undamaged laminate, therefore lowering the compressive strength of the structural component.

Experimental studies on the effect of elevated temperature aging on CAI strength are an ongoing research effort in the Department of Aeronautics and Astronautics at the University of Washington. In 1991 a program was begun to investigate the degradation of a thermoset matrix composite (IM7/5260) when exposed to elevated temperature environments. The resulting data showed a significant decrease in residual strength properties of impacted laminates, with accelerating degradation as temperature increased [3]. Damage size was also seen to increase dramatically for laminate panels that were aged before impact.

Thermoplastic matrix materials have shown better damage resistance than comparable thermoset materials, and are thought to be more resistant to aging effects because they do not show significant weight loss with aging. However, the influence of elevated temperature on strength and toughness characteristics had not been explored in a thermoplastic composite. Therefore, a study was begun in 1994 to ascertain how elevated temperature affected the durability of thermoplastic composite (IM7/K3B) laminates. CAI strength was found to be significantly higher for the K3B system than in the 5260 material. The CAI strength of the K3B material also showed significant decreases after relatively short aging times.

Aging mechanisms have been investigated throughout the research effort. This dissertation focuses on the aging of polymeric composites, and the effects of aging on durability. A background of polymer science as it applies to thermal aging of polymeric composites is reviewed in Chapter 2.

Experiments on the material changes occurring during aging are presented in Chapter 3, along with observations on the aging mechanisms. A numerical model of the diffusion-reaction process is put forth in Chapter 4, and compared to experimental data. The remaining chapters discuss CAI strength. Current theories for predicting CAI strength are reviewed in Chapter 5. Experimental procedures and results of this research are given in Chapter 6. The effects of elevated temperature aging mechanisms on CAI strength are discussed in Chapter 7. Finally, Chapter 8 summarizes the entire work and makes recommendations for future efforts.

## Chapter 2

### AGING OF POLYMERIC MATERIALS

The graphite fibers commonly used in aerospace structural components remain unchanged at temperatures in the range of 149°C to 204°C, even after very long aging times. However, the matrix material surrounding the fibers is susceptible to chemical and physical changes at these elevated temperatures. The changes in the matrix material can alter the transverse and shear stiffnesses of a ply, and also the resistance of the composite to delamination and fracture. Changes in these basic ply properties lead to changes in the performance of the structure. Therefore, any study in the aging of polymeric composites must include an explanation of polymer chemistry. This chapter gives a brief background on the polymer science involved in processing the matrix material, and then describes changes to the polymers caused by thermal aging.

#### 2.1 Processing of polymeric materials

Monomers, defined as the smallest structural repeat unit, are the basic building blocks of polymers. A polymer is a long string of monomers linked together with covalent bonds. These strings are on the order of thousands to hundreds of thousands of monomers long. Figure 2.1 shows the chemical structure of the well known polyvinyl chloride, or P.V.C.

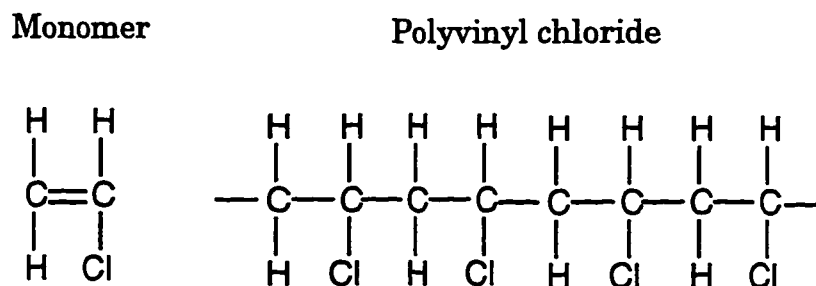


Figure 2.1 Example of a monomer and the resulting polymer molecule

The extent of polymerization in plastics is highly variable. The type and proportion of reactants, the curing temperature and pressure, and the curing time all influence the length of the polymer chains. In addition, the length of the polymer chains within a given polymer sample is very non-uniform. Polymer molecules have a large range of lengths in a real material, ranging from a single monomer to hundreds of thousands of monomers in length. Several definitions for the average molecular length of a polymer and the statistics of the formation process have been developed [4-6]. For this research, numerical measures of molecular weight and the statistical aspects of polymerization are not needed. Only the concept, that polymeric material is composed of individual molecules varying in length but containing the same basic monomer unit, is important.

The bonds joining the monomers along the polymer chain are all covalent bonds, which is the strongest type of inter-atomic bond. Bonds between chains are of many types. When the intermolecular bonds are chemical bonds, known as cross-links, the polymers are joined into a web of interconnected strands and individual polymers cannot be separated out of the material. Materials with a high density of chemical cross-links are known as thermosets. This term arises from the fact that these materials are set in their chemical structure by the curing process. Returning the material to high temperatures results only in degradation, not melting.

Polymers with few chemical cross-links are held together by secondary bonding forces, principally Van der Waals forces. This type of material is known as a thermoplastic. The best analogy to describe a thermoplastic polymer is a mass of cooked spaghetti. At low enough temperatures, the individual strings stick together in a large clump. At high temperatures, the strings can slide across one another relatively easily, thus greatly reducing the stiffness of the mass. The temperature at which the viscosity of the material drastically changes is termed the glass transition temperature ( $T_g$ ) and will be described in greater detail in Section 3.4.

In reality, there are not distinct classes of polymer material. Most thermoplastics contain some covalent cross-links, and most thermosets have some amount of plasticity. But dividing polymers into the two general groups is a useful way of categorizing the materials. Thermosets are easier to produce, with good stiffness and strength to weight ratios. Thermoplastics are more resistant to damage and have greater thermo-oxidative stability at elevated temperatures [7].

Polymers are formed from monomers in several ways. The simple example of P.V.C. shown earlier was formed by addition polymerization, in which a monomer attaches to the end of the nearest polymer until further polymerization is not possible. Ring opening polymerization, which is the method used to form Nylon, uses a catalyst to break open ring structure molecules which then bond together in a long string. Condensation polymerization is the most commonly used process for aerospace materials. During condensation polymerization, two or more types of monomer are mixed together along with a catalytic agent. The mixture is heated, and the monomers react to form the polymer chain and residual chemical products which are unwanted in the final material and must be removed.

In CFRP's, the polymer matrix must be incorporated with the fiber reinforcement. The first step is to mix the monomers with a catalytic agent and partially cure the material. The monomers form oligomers, which are polymers averaging tens of units in length. The oligomers are then combined with the graphite fibers into large sheets. The sheets are unidirectional, meaning all fibers are parallel to one another, and on the order of 0.0125 cm thick. The prepreg sheets are then assembled into a specific structural configuration. The component is cured using pressure and heating cycles designed to produce optimum qualities. Pressure is used to remove voids and unwanted volatile products. Figure 2.2 shows the basic steps for producing IM7/K3B laminates, with the initial monomers, the partially cured prepreg, and the fully cured material. Figure 2.3 gives parameters for the final cure of the material. These high temperatures are typical of the new class of thermoplastic composites.



Producing the 'optimum' result is not always an easy task. Volatiles are often difficult to remove completely. Voids form within the matrix material. The length of polymers varies throughout the matrix, as does the degree of cross-linking and other parameters. The material is a complicated mixture of varying length molecules and monomers with pockets that can never be modeled exactly, only in the average sense.

## 2.2 Physical Aging

As with any material, polymeric composites can undergo changes in the microstructure during operation. Physical aging is the process of changing the polymer structure without altering any of the chemical bonds. At room temperature, the polymer chains of the materials studied in this research are essentially frozen in place, lacking the energy to change their conformation. When raised to higher temperatures, the molecules gain the energy necessary to rotate about their chemical backbone. If the material is in an equilibrium configuration, the net sum of the countless individual conformation changes is zero. However, the polymers are not in equilibrium. Above the glass transition temperature, the polymers have the energy to obtain equilibrium conformation almost instantly. As temperature is lowered, the equilibrium conformation is a more dense packing structure. At the glass transition temperature, the polymer mobility drops significantly but the equilibrium density continues to decrease at the same rate. The end result is a polymeric material 'frozen' in a higher equilibrium position. When the polymer is raised from room temperature to nearer  $T_g$ , the material will slowly move towards equilibrium conformation. The new conformation is more tightly packed, and so the material becomes more dense.

The greater density will affect matrix dominated stiffnesses of the composite structure. The matrix dominated stiffness properties are the transverse, meaning perpendicular to the fibers, and shearing stiffnesses. Shrinkage is also important in physical aging, possibly altering the stress state of the composite laminate. Experimental studies concerning the effect

of physical aging have found shrinkage to occur, even under tensile loading [9]. The increased density can also be detrimental to the toughness of the material [10], reducing the compliance and thus the ductility of the matrix material.

Creep behavior refers to the slow strain increase over time when held at constant stress, or the relaxation of stress under constant strain. Under the proper thermal and loading conditions, the long term behavior of polymers is like a fluid with very high viscosity [11]. Modeling the creep behavior after aging has received most of the attention of recent studies concerning physical aging. Experimental studies have found that effective time theory accurately predicts long term creep behavior [12]. This method allows long term creep behavior of composites at moderate temperature to be predicted based on short term creep data at higher temperatures. Brinson and Tuttle have used this method to form a general model with predictive capabilities [13-14]. The ply level creep behavior can be built up into a model for response of a polymeric composite structure.

### 2.3 Chemical Aging

Chemical aging alters the molecular bonding of the polymers. Chemical aging is a broad category which covers all changes in the atomic structure of the molecules. For polymers, this is a very important aspect of the aging process.

The first type of reaction a polymer undergoes when exposed to elevated temperature is continued curing. The curing cycle is designed to produce polymers having material properties that are considered optimum. The curing cycle may also be optimized for processing time, and so the material may not be completely cured for manufacturing reasons. High molecular weights usually yield stiffer and stronger materials, but too many cross-links or a very high molecular weight material can be brittle and have low fracture resistance. Even at temperatures below the curing temperature, additional cross-linking and chain growth can occur. Only a

limited amount of post-cure reaction will usually take place, since a saturation point is quickly reached as the reactants are consumed. But the post-cure reaction to elevated temperature may cause a change in the properties of materials after short aging times.

A more detrimental process which occurs at elevated temperature is the formation of chemical radicals and subsequent chain scission. Chain scission is the process whereby covalent bonds in the polymer are broken, reducing the molecular weight of the polymer and ultimately the stiffness and strength of the material. Returning to the example given previously, ultraviolet radiation causes chlorine atoms to break away from the polymer chain. Atoms in the resulting molecule are chemically unstable, having unfilled outer electron shells. The polymer stabilizes by chain scission, as shown in Figure 2.4. For each chain scission, there are two resultant free radicals. These free radicals can combine, terminating the degradation, or cause further chain scission, propagating the degradation.

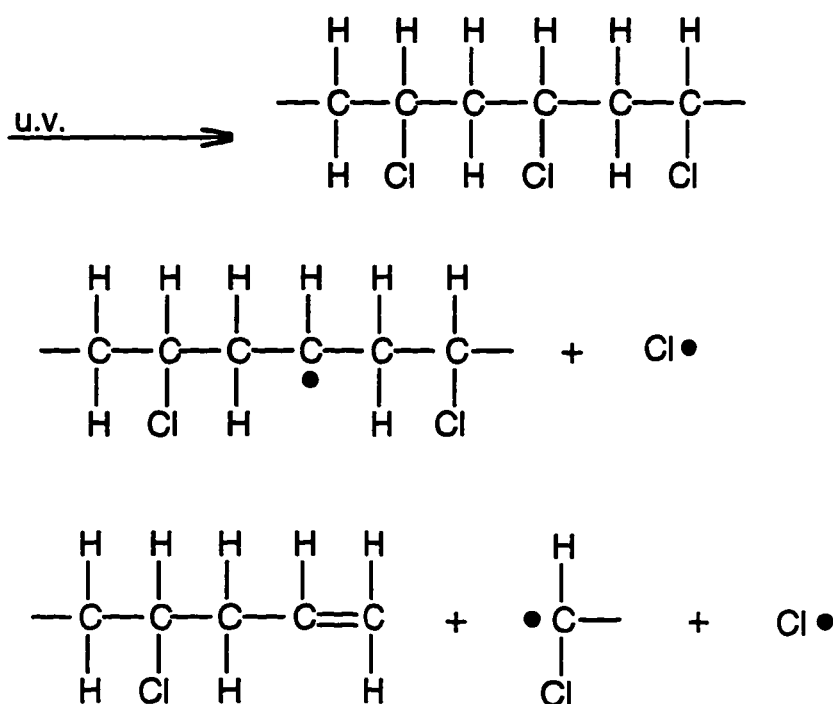


Figure 2.4 Chain scission due to photo-oxidation

Photo-oxidation has largely been negated in aerospace applications by the use of coatings to protect the polymeric materials from ultraviolet radiation. However, a much larger problem for these applications is thermo-oxidation, the chemical decomposition of polymer chains due to the presence of atmospheric oxygen at elevated temperatures. The oxygen combines with the polymer, breaking the chains and reducing the molecular weight. Very low molecular weight polymers can then be leached into the environment, causing weight loss. As the polymer chains are broken and weight loss occurs, mechanical properties decrease. The connection between decreasing molecular weight and decreasing mechanical properties is difficult to model on a molecular level, although some theories have been presented [15, 16].

There is a substantial amount of experimental data on the detrimental effects of aging on composite properties, and a few examples are given here. Bismaleimide composites have shown a 40% decrease in CAI strength after one year of aging at 204°C [17]. Transverse flexural strength was shown to be a good measure of degradation in PMR-15 [18]. Glass transition temperature also receives a good deal of attention. In almost all cases, the  $T_g$  is shown to increase with aging [19] through a combination of physical and chemical changes.

The aging process is a combination of physical aging, oxidation degradation, and post-curing of the matrix material. Physical aging and post-curing occur homogeneously throughout the material, while oxidation is limited by the availability of oxygen. Microscopy studies are very helpful in determining the location of the oxidation degradation process [20]. Thermo-oxidative degradation begins at the surface of the structure and grows into the interior over time. This is verified experimentally by studies on the effect of specimen thickness on shear properties. Shear strength of thin composite specimens was shown to decrease by roughly 60% during thermal aging, while thick specimens maintained their original strength [21]. Other research indicates that the interphase between fiber and matrix is the critical region for degradation of shear properties [22].

Efforts to model weight loss in polymeric composites due to aging have been fairly successful. The rate of weight loss is essentially proportional to the exposed surface area. However, the calculation of the surface area must be performed with great care. The interaction of fiber and matrix will effect the weight loss, with the degradation proceeding more rapidly in the direction of the fibers [23]. The anisotropic effect was modeled successfully by calculating the area around fibers near the exposed surfaces of the composite material [24]. Cracks sometimes develop in the polymer during aging, accelerating the degradation by increasing the exposed surface area [25]. Time-temperature equivalence is applicable to the weight loss process as well [26, 27]. In all of these cases, a degradation layer develops growing into the composite from the exposed surface.

Modeling of changes in the mechanical properties of composite structures due to chemical aging has received little attention from the research community. Efforts have been made by Shah & Patni [28] to model the process using cumulative damage theory, first proposed by Miner in 1945 [29]. The basis of this theory is to use simple equations to model the individual degradation processes, deduced largely from experimental data. The results are combined using linear superposition to predict the total effect of aging on mechanical properties during the lifetime of the material. McManus uses a similar approach [30], but with equations appropriate to composite laminates. These methods are simple but effective first steps in the modeling of aging.

## Chapter 3

### **MATERIAL PROPERTIES TESTING**

There is a wealth of experimental data on the degradation of mechanical properties for coupon sized specimens. The physical and chemical processes which occur during elevated temperature aging are fairly well understood. Modeling of laminate properties using degradation metrics has begun, and models of physical aging have been developed. However, modeling of mechanical property degradation based on chemical aging is limited. Therefore, material property studies and chemical analyses were used to better understand the link between chemical aging and mechanical property deterioration. The data provided insights into the most significant aspects of aging, but also raised questions which must be answered in future studies.

Fracture toughness, degradation depth around an open hole, and uniaxial compressive strength from four point bend testing were studied in this research. Fracture toughness is a very important measure of durability of composite laminate materials, and showed degradation with aging. Open hole specimens provided a simple geometry for use in modeling the size of the degraded region during aging. Four point beam testing was investigated as a simple measure of the degradation of compressive strength for polymeric composites.

Microscopy, Electron Spectroscopy for Chemical Analysis (ESCA), Differential Scanning Calorimetry (DSC), and Secondary Ion Mass Spectroscopy (SIMS) were used to analyze the chemistry of the material. Microscopy showed differences in fracture surfaces and degradation in surfaces exposed to air during aging. ESCA analyzed the chemical structure of the matrix material along the fracture surface of mode I and mode II specimens. DSC showed increases in glass transition temperature ( $T_g$ ) and evidence of physical aging. SIMS also analyzed the chemical structure, and found evidence of chemical aging in K3B.

### 3.1 Fracture toughness

Fracture toughness refers to the ability of a material to resist crack propagation. Fracture toughness can be divided into three components, representing the three modes of cracking. Mode I is an opening of the crack, mode II represents in-plane shear, and mode III is a tearing motion (Figure 3.1). For composite materials, cracks generally propagate along the fibers. These cracks can be interlaminar, occurring between plies, or matrix cracks, occurring within a single ply. An accepted test for the mode I interlaminar fracture toughness of composites uses the Double Cantilever Beam (DCB) specimen [31]. The two beams are pulled apart, and a crack grows into the laminate while Crack Opening Displacement (COD), load, and crack length data are recorded. The data is used to calculate  $G_{Ic}$ , the change in strain energy with respect to crack extension. Mode II fracture toughness is generally measured using an End Notch Flexure (ENF) specimen [32], although the validity of this test method is still debated. ENF testing uses a three point bend to place an existing crack tip under mode II loading. The load and center deflection of the beam are measured at the point of crack growth, and then beam theory is used to calculate the change in strain energy with crack extension. Mode III tests are under development, but no commonly accepted test method exists today. Mode III fracture toughness was not studied in this research.

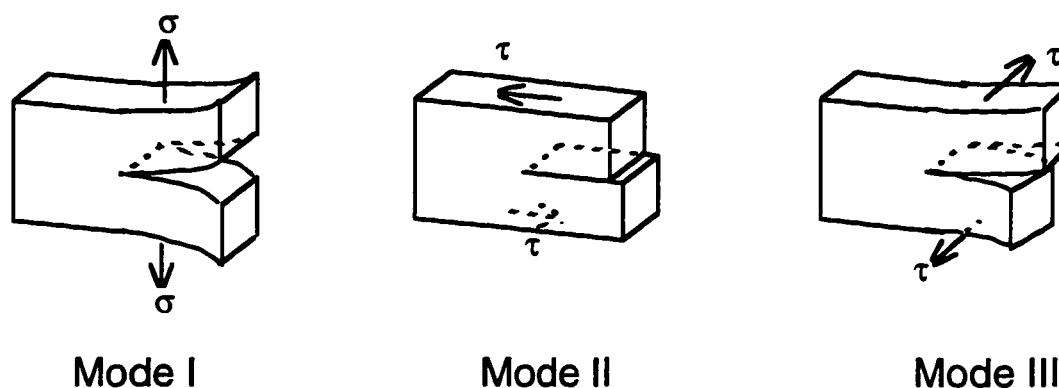


Figure 3.1 Modes of crack propagation

DCB and ENF specimens were fabricated from IM7/K3B, a graphite fiber polyimide matrix composite, and IM7/5260, a graphite fiber bismaleimide matrix composite. The layup for the fracture toughness specimens was  $(0_{10}/D/0_{10})$ , where D indicates a Kapton delamination insert at the mid-plane, used to simulate an existing crack.

The large panels were cut into 2.5 cm wide test coupons with the length parallel to the  $0^\circ$  fiber direction. The trimmed length of the mode I DCB specimens was 23 cm with a 5 cm initial crack length, and the mode II ENF specimens were 15 cm with a 2.5 cm initial crack length. A diagram of the fracture toughness specimens is provided in Figure 3.2. The material was cut using a fluid cooled diamond cutting wheel.

Aging temperatures were chosen to simulate the expected operating environment of the HSCT. The  $204^\circ\text{C}$  aging temperature was chosen to study accelerated aging. Aging time was a maximum of two years, or 17,500 hours. This is less than the 60,000 hour life of an aircraft, but certainly represents a sufficient percentage of the lifetime to draw meaningful conclusions about the aging process. Complete test matrices for mode I and mode II testing are presented in Tables 3.1 and 3.2.

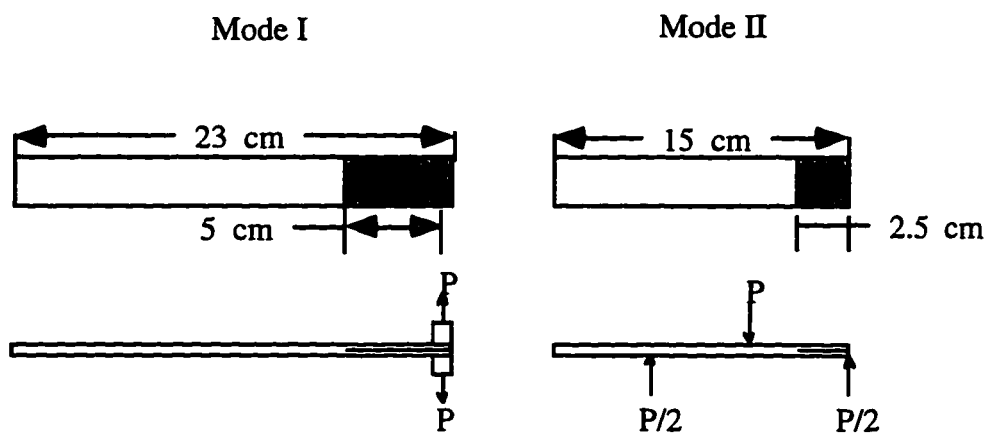


Figure 3.2 Schematic diagram of fracture toughness specimens



Before aging, all fracture toughness specimens were given a mode I pre-crack by forcing a wedge along the delamination insert. Cracking was controlled by clamping the specimen with a vise 0.3 cm ahead of the delamination tip. Pre-cracking was performed in order to move the crack tip beyond the resin rich region at the end of the delamination insert. The crack tip resulting from pre-cracking was defined as the origin for all crack growth calculations.

Isothermal aging of all specimens was performed in three air-circulating ovens. Once the specimens were placed inside, the ovens were programmed to reach aging temperature at a controlled rate of 2°C/min. The ovens were then set to continuously maintain the desired aging temperature. After aging of a set of specimens was completed, the ovens were allowed to cool and the specimens were removed. Cooling rates could not be controlled electronically, but were maintained at less than 2°C/min by controlling the amount of room temperature air flowing into the ovens. Time spent during the removal process was not counted toward the total aging time of the specimens.

After aging, the specimens were removed from the ovens and all pertinent dimensions measured. The exact location of the crack tip at the edge was marked on the specimen. White paint was applied to the edges of the specimens to aid in crack tip location during testing. End blocks were attached to mode I specimens for load application, using a high temperature cure adhesive system. The adhesive cured under pressure at 175°C for 4 hours. The pressure was then removed, and the adhesive post-cured at 150°C for 8 hours. Marks were scribed into the sides of the specimens at 0.25 cm increments from the crack tip, to provide reference lines for crack tip location during testing.

### *3.1.1 Mode I fracture toughness*

Prepared DCB specimens were placed in the testing oven at room temperature. Load was applied to the end blocks using a displacement controlled motor. The crosshead deflection was measured using a COD clip

gage installed outside the testing chamber on the displacement arm. A load cell and the COD gage were connected to a personal computer with a data acquisition board installed. Using data acquisition software, the computer performed as a virtual instrument, taking readings of load cell output voltage and clip gage output voltage two times per second.

Once the DCB specimen was mounted in the testing chamber, the oven was heated to test temperature. An internal fan stabilized the chamber temperature within  $\pm 1\%$  of the set point. The specimen temperature was monitored at all times using a mercury thermometer placed near the crack tip. The testing equipment is shown in Figure 3.3.

The displacement arm was lowered at 0.3 cm/min until the crack length grew 0.25 cm, as measured by the scribed lines on the side of the specimen. The specimen was unloaded, and the load versus displacement curve recorded. Each crack tip was photographed under magnification for accurate crack length measurement. The unloading/loading process was repeated until 6 loading curves had been recorded.

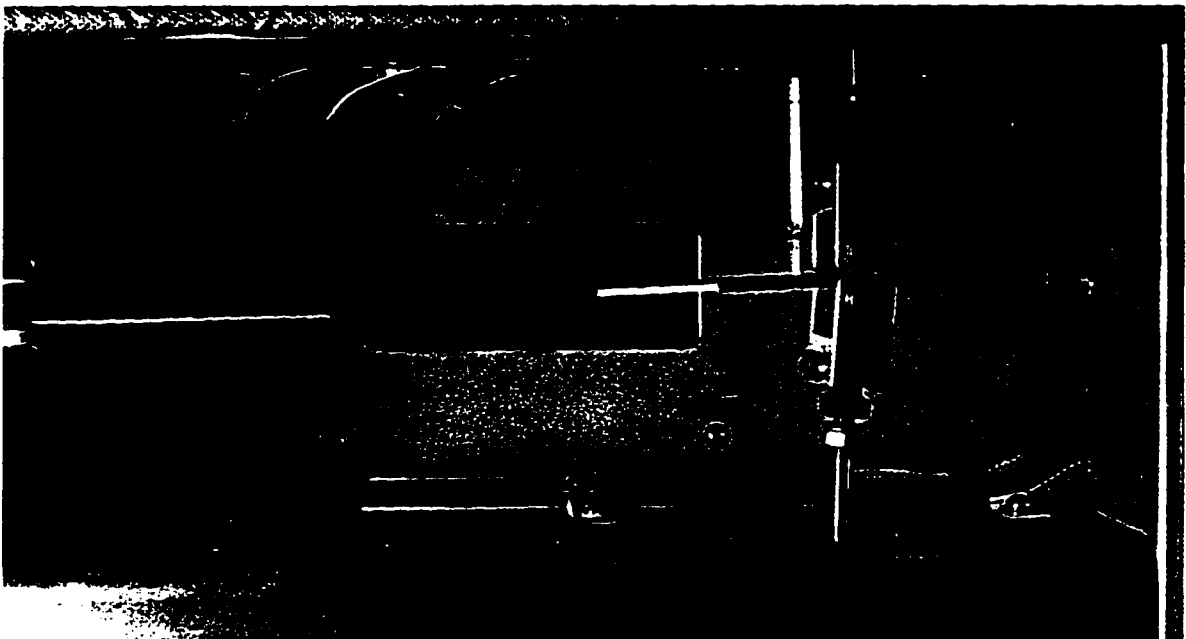


Figure 3.3 DCB testing of mode I fracture toughness

Upon completion of the test, the six plots of load versus displacement were compiled onto one graph. The intercept of the initial load-displacement curve and the x-axis was found, and the displacement data was then shifted so that the intersection point coincided with the origin. This shifting was necessary because of varying slack in the load line upon test inception. The displacement data recorded by the clip gage outside the testing chamber was converted to COD by accounting for extension of the load line using a measured correction factor. A typical plot of the final load versus COD data is given in Figure 3.4.

Calculation of  $G_{Ic}$  was initially accomplished using the area method [33]. In this method,  $G_{Ic}$  is equal to  $dU/da$ , where  $dU$  is the area of one loading/unloading region, and  $da$  is the width of the specimen multiplied by the corresponding crack extension.  $G_{Ic}$  for a specimen was determined by

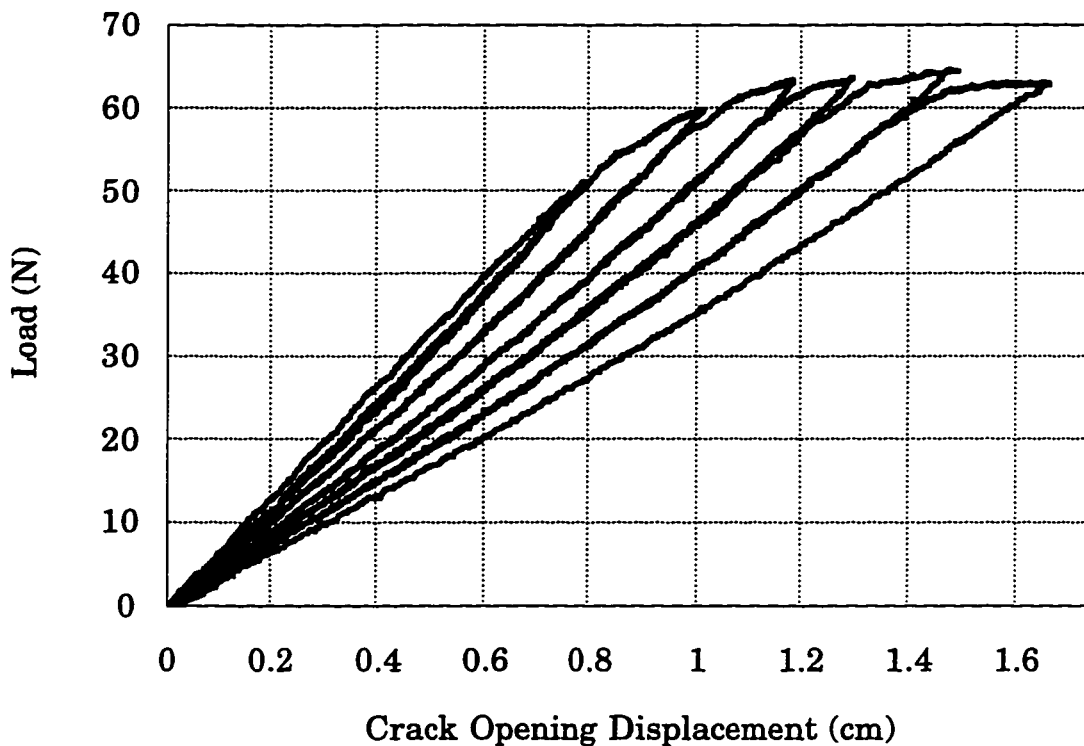


Figure 3.4 Load-displacement curves for a DCB test

averaging the values obtained for individual loading curves. The area method of calculating  $G_{Ic}$  produced inconsistent data. The beam theory equations [31, 32] are better methods of determining  $G_{Ic}$ . A comparison of the various methods of calculation for one specimen is shown in Figure 3.5. All of the beam theory methods showed improved repeatability over area method calculations. Modified beam theory was chosen for use in this study.

Modified beam theory method calculates critical fracture toughness as

$$G_{Ic} = \frac{3P_c \delta_c}{2b(a + \Delta)} \quad (4-22)$$

where  $P_c$  is the load at crack extension,  $\delta_c$  is the COD at crack extension,  $b$  is the width of the specimen, and  $a$  is the crack length.  $\Delta$  is the intercept of

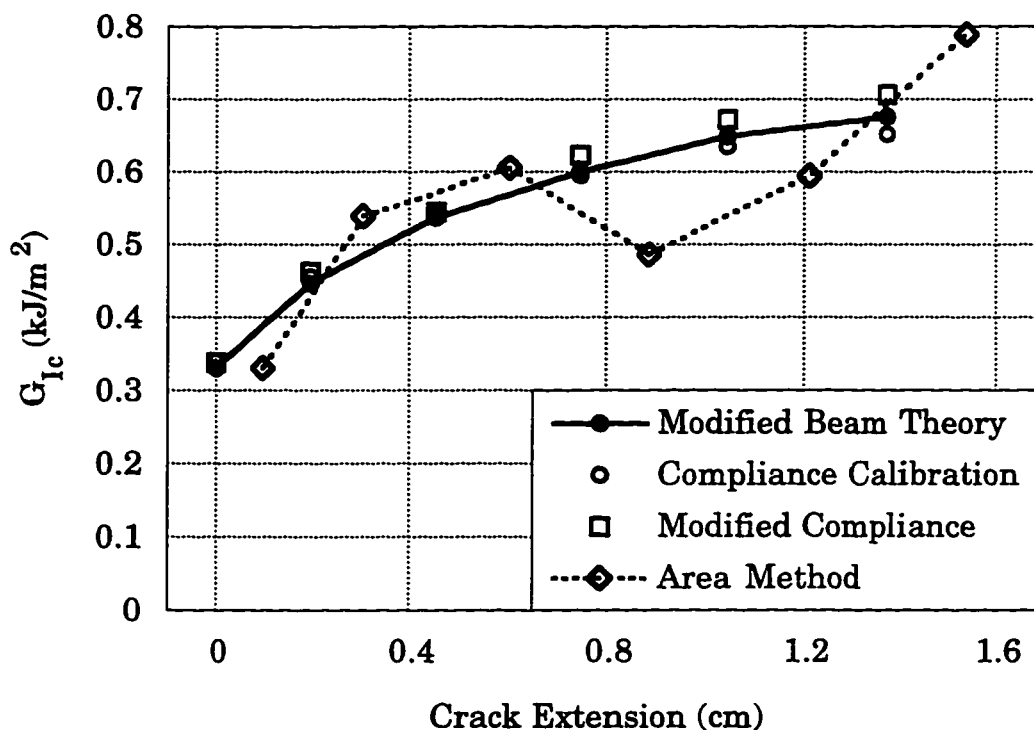


Figure 3.5  $G_{Ic}$  for a DCB test using various calculation methods

a least squares linear fit to the cube root of compliance versus crack length curve. Beam theory assumes that the cantilever beams are perfectly clamped at the crack tip. For real specimens, some rotation will occur due to shear stresses, and  $\Delta$  accounts for this error. Correction factors for end block effects and large displacement effects [34] were calculated, but found to be insignificant for this study.

A problem encountered in all fracture toughness testing was fiber bridging. The initial crack was created with a delamination insert, providing a clean crack tip. When the crack extended into the specimen, sometimes fibers remained connected between the top and bottom surface. Instead of remaining parallel to the crack, the fibers bridged the gap between top and bottom surface. This provided a measurable [35] closing force, and raised the load required to open the crack. Figure 3.6 shows the fiber bridging across the crack of a DCB specimen.

The effect of fiber bridging changed as the crack grew into specimens tested at elevated temperature, and thus the calculated  $G_{Ic}$  was a function of crack length. To better understand the data,  $G_{Ic}$  was plotted as a function of crack growth. The tip of the pre-crack was used as the origin. A curve fit of the form  $G_{Ic} = C_1 - C_2 \cdot \exp(C_3/\Delta a)$  was calculated for the data. From this fit, initial  $G_{Ic}$  and fracture toughness after fiber bridging were calculated. An example of this curve fit is given in Figure 3.7, showing data for IM7/K3B specimens tested at 149°C with no aging.



Figure 3.6 Scanning electron micro-graph of fiber bridging

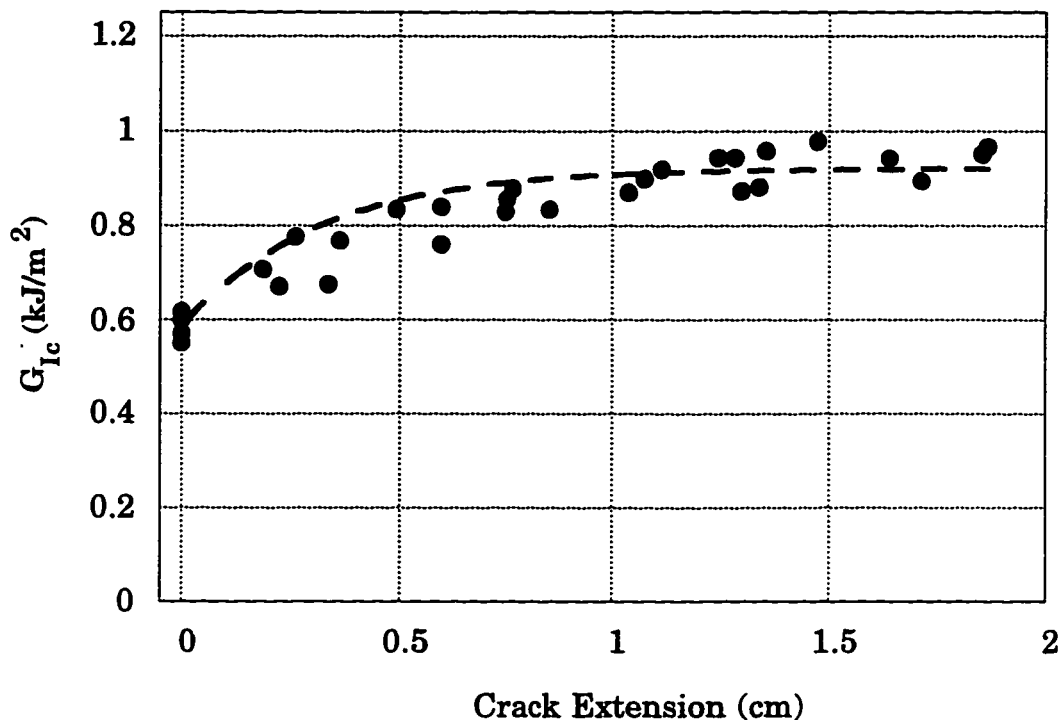
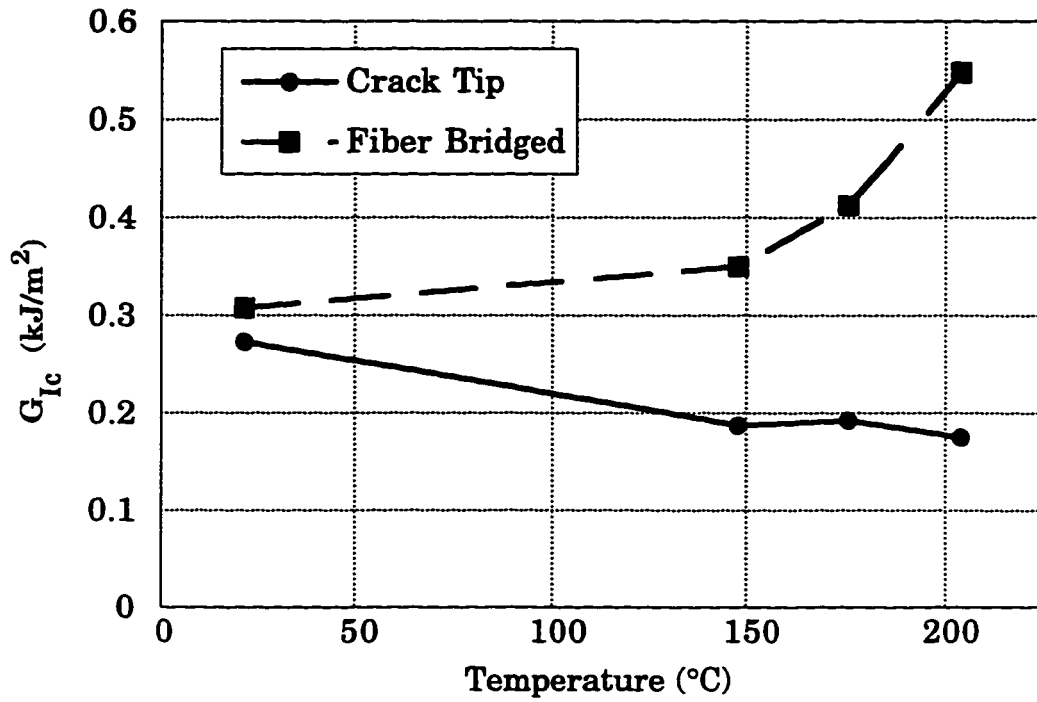
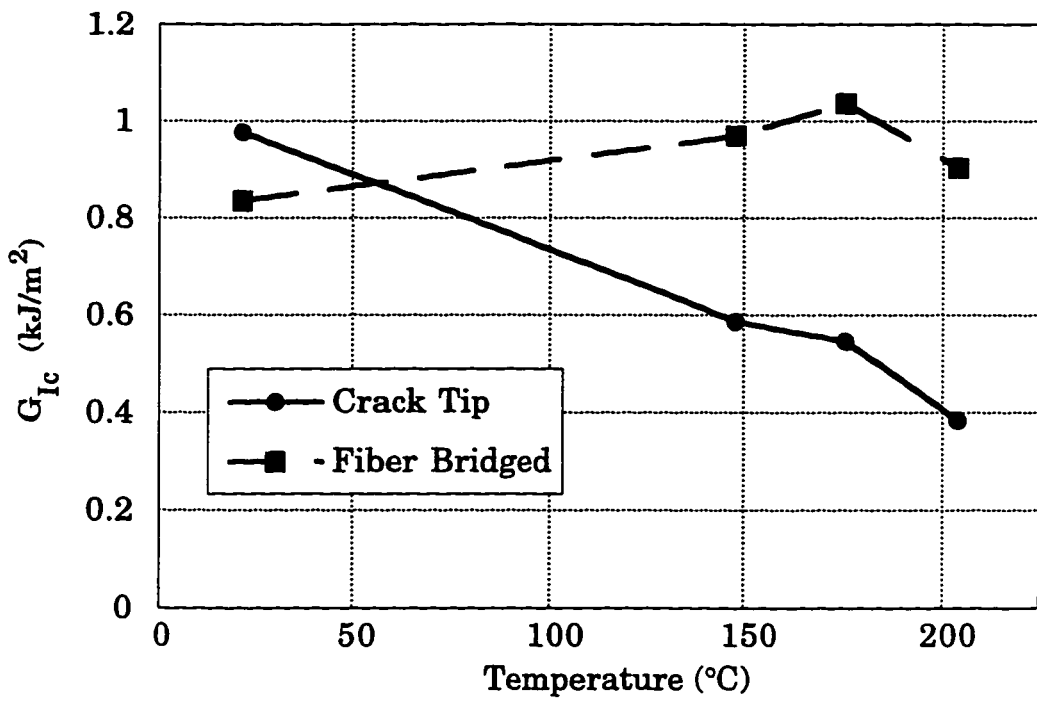


Figure 3.7  $G_{Ic}$  as a function of crack extension

The dependence of  $G_{Ic}$  on testing temperature is plotted in Figures 3.8 and 3.9 for unaged specimens. As the testing temperature increases, the matrix material becomes more compliant and therefore the critical fracture toughness goes down. However, the influence of fiber bridging increases with temperature. Fibers at higher temperatures tend to pull out of the matrix material and remain connected across the crack, rather than remaining embedded in the matrix and breaking. These two trends explain the differences in data for fracture toughness at the crack tip and within the specimen. At the crack tip, there is little fiber bridging and the properties of the polymer dominate  $G_{Ic}$ . As the crack grows, the number of fibers bridging the crack increases, and therefore measured fracture toughness within the specimen increases with temperature.

Figure 3.8  $G_{Ic}$  for unaged IM7/5260Figure 3.9  $G_{Ic}$  for unaged IM7/K3B

Fiber bridging also influenced the fracture toughness of aged specimens. The calculated  $G_{Ic}$  at the crack tip of IM7/5260 specimens increases with aging time, as shown in Figure 3.10. Aging seems to be improving the fracture toughness of the matrix material. However, examination of the crack tip region after testing revealed a different cause for the increase in calculated  $G_{Ic}$ . In a unidirectional laminate, interlaminar cracks often cross over individual fibers so that the fiber is connected across the top and bottom surfaces of the laminate. In unaged material, the number of bridged fibers is small. Oxidation degradation of the bismaleimide matrix is so severe that the fibers at the surface have little matrix material surrounding them. With no matrix material at the crack tip, the fiber bridging is significant. The effect is shown by the comparison of load vs. crack opening displacement for unaged and aged specimens (Figure 3.11). The fiber bridging in the unaged material remains constant throughout the specimen, whereas the load is much higher near the crack tip of aged material. This higher load does not represent an improvement in matrix properties. Rather it is an effect of the change in fiber orientation during testing.

After the crack tip has grown past the degraded region, fiber bridging decreases and the measured fracture toughness decreases as well. The  $G_{Ic}$  values represent the change in fracture toughness without the effect of oxidation degradation. As can be seen in Figure 3.12, the fracture toughness of material without oxidation degradation remains relatively unchanged with respect to time in 5260.

The severe oxidation degradation does not occur in K3B, and therefore the effect of fiber bridging in this material is the same as for unaged materials. Fiber bridging at the crack tip is negligible, and thus the  $G_{Ic}$  value at the crack tip represents fracture toughness of the matrix material. Fiber bridging increases as the crack grows into the specimen, artificially raising the measured  $G_{Ic}$ .

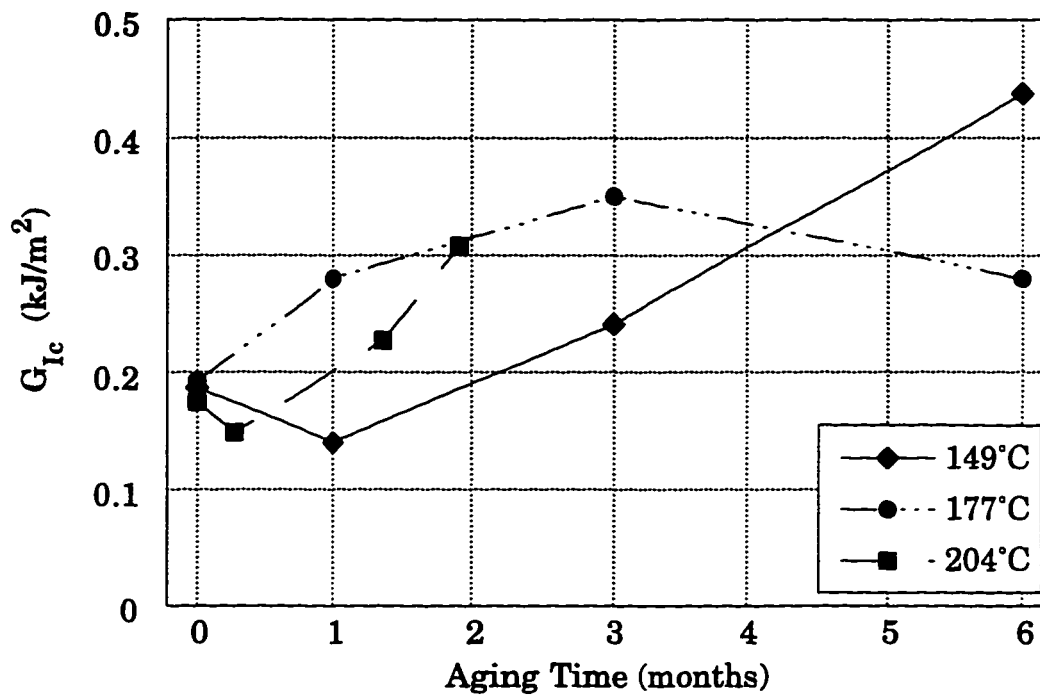


Figure 3.10  $G_{Ic}$  at the crack tip of aged IM7/5260 specimens

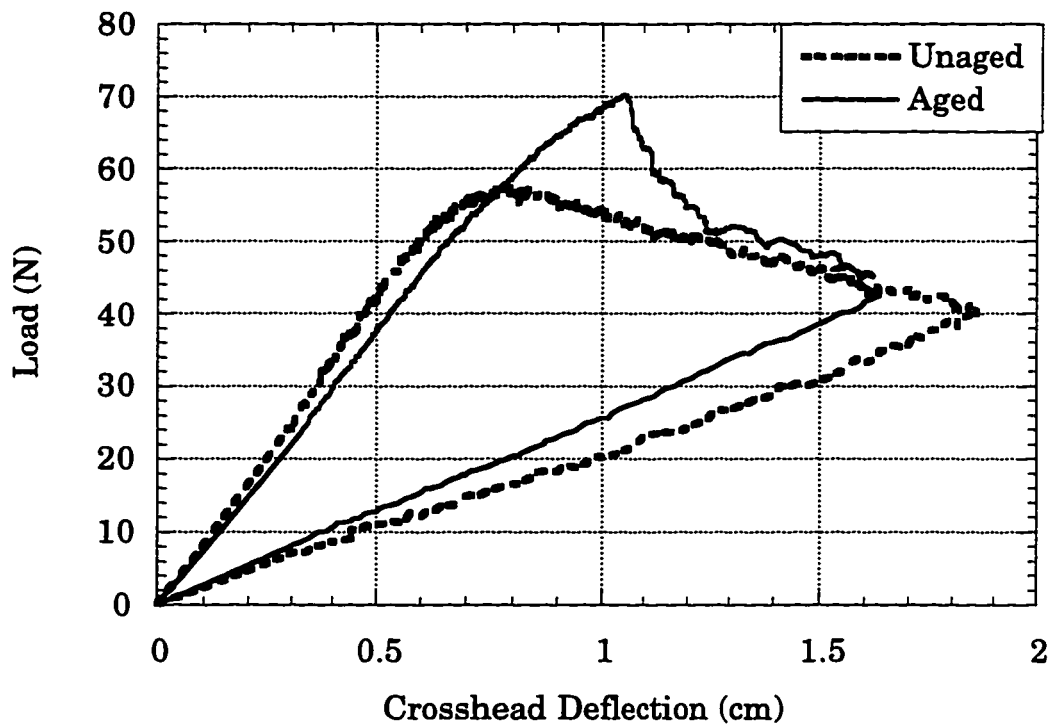


Figure 3.11 Comparison of aged and unaged DCB data for IM7/5260

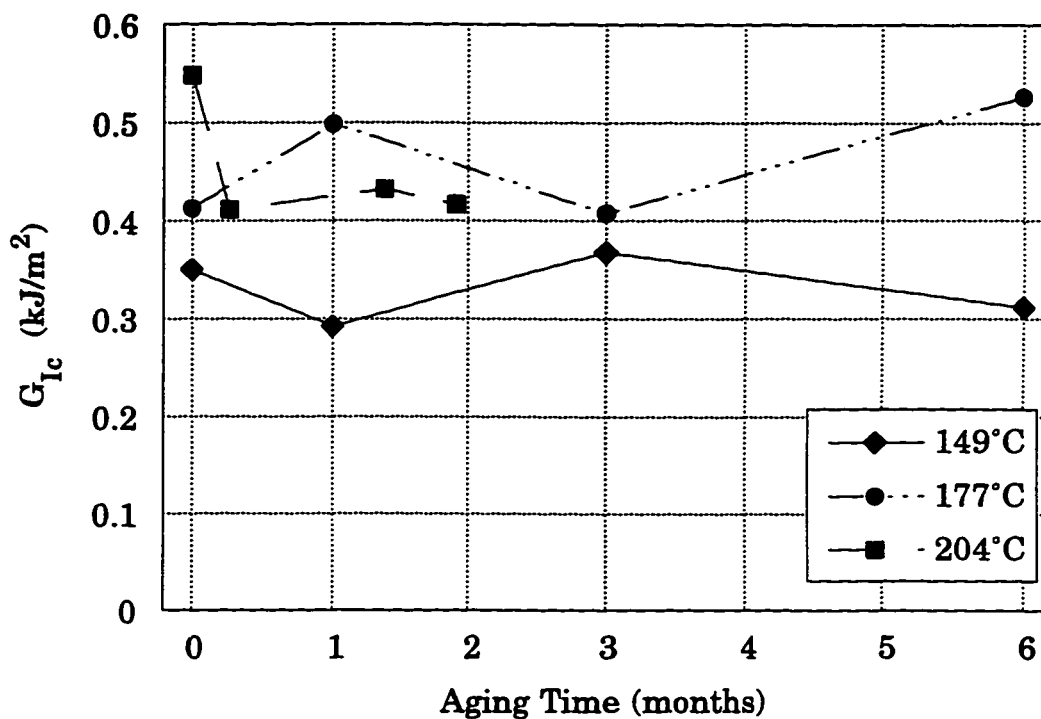


Figure 3.12  $G_{Ic}$  in the interior of aged IM7/5260 specimens

Fracture toughness of K3B decreases with aging time. Looking at the results plotted in Figure 3.13, the decrease is very clear for specimens aged longer than six months. From six months of aging to thirteen months of aging, the calculated  $G_{Ic}$  values drop approximately 30%. The decrease is also clear for specimens aged at 177°C and subsequently tested at room temperature, which have little influence from fiber bridging. Aging beyond thirteen months does not appear to cause further degradation. Examination of the test specimens after testing has shown that degradation penetrated through the thickness of specimens aged thirteen months (see Section 3.2), and so further penetration is not possible.

The data for specimens aged less than six months appears to be conflicting. The specimens aged at 177°C show a steep decrease from zero aging to one month, and then increase from three to six months. In

contrast, specimens aged at 204°C show an increase from zero to one month of aging. All test data and testing variables were examined carefully, and no errors were found in the testing or specimen preparation procedure. Possibly, the fracture toughness is sensitive to the curing procedure. After long aging times the material will be completely cured. But at short aging times, differences in the amount of cure between groups could still exist.

The trends in data for  $G_{Ic}$  at internal regions of the material are much more difficult to determine from the data, shown in Figure 3.14. The amount of fiber bridging varied greatly between specimens, causing very large data scatter and masking the effects of aging at high temperatures. However, trends can be determined by looking at the  $G_{Ic}$  for tests conducted at lower temperatures, where fiber bridging is limited. The room temperature and 1549°C tests show a progressive, downward trend. Data from tests conducted at 177°C is more scattered, but also shows steady decreases with aging time.  $G_{Ic}$  decreases roughly 10% every six months at all three testing temperatures. At the highest test temperature, the K3B polymer is approaching the glass transition temperature. The material is very soft, and fiber bridging has a very strong influence. This creates the large data scatter shown for specimens tested at 204°C.

Comparison of the load-displacement data for K3B specimens tested at room temperature shows the lowered fracture toughness at the crack tip. Specimens tested at this temperature have little variation in  $G_{Ic}$  along the crack length due to fiber bridging. For unaged specimens, the load was highest at crack initiation and then was reduced as the crack grew. However, the aged specimens reached their load peak after the crack had grown into the specimen (see Figure 3.15). The difference in loads at crack initiation are quite significant, resulting in a 40% drop in calculated  $G_{Ic}$  for the aged specimens. This drop is attributed to oxidation degradation at the crack tip, penetrating into the specimen as aging time increases. The oxidation at the crack tip will be discussed further in the section on degradation depth.

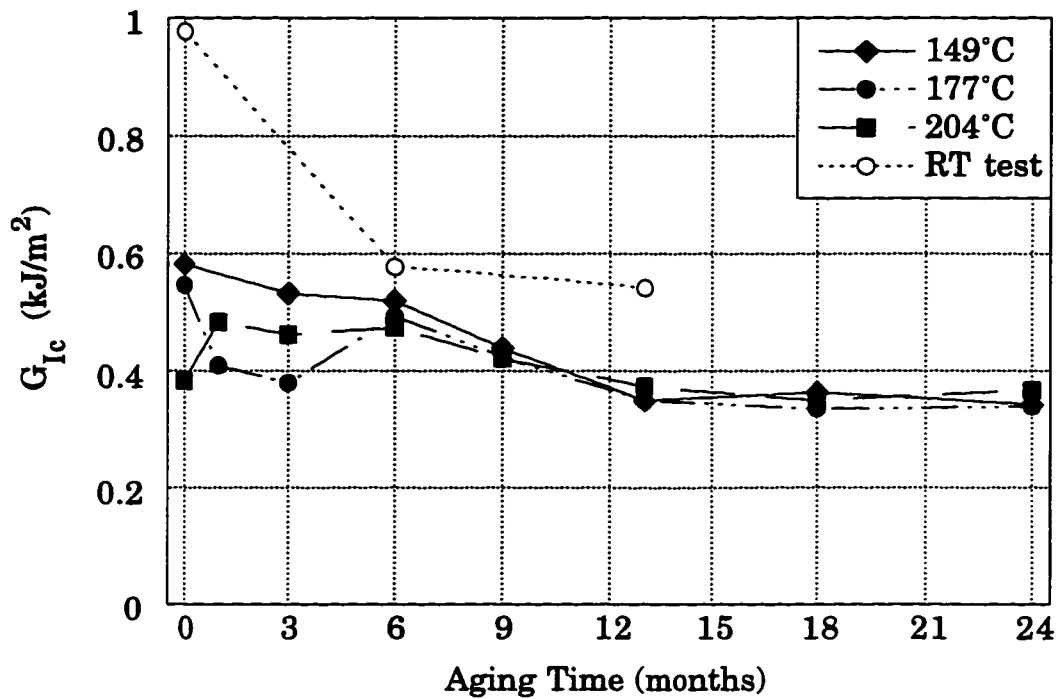


Figure 3.13  $G_{Ic}$  at the crack tip of aged IM7/K3B specimens

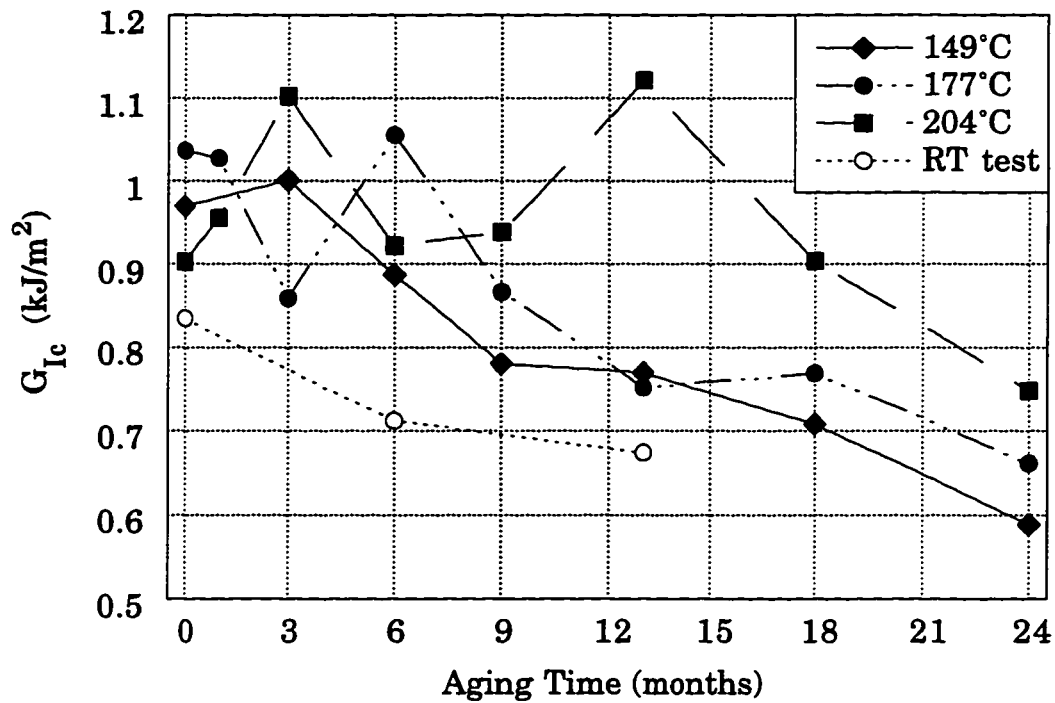


Figure 3.14  $G_{Ic}$  of the interior of aged IM7/K3B specimens

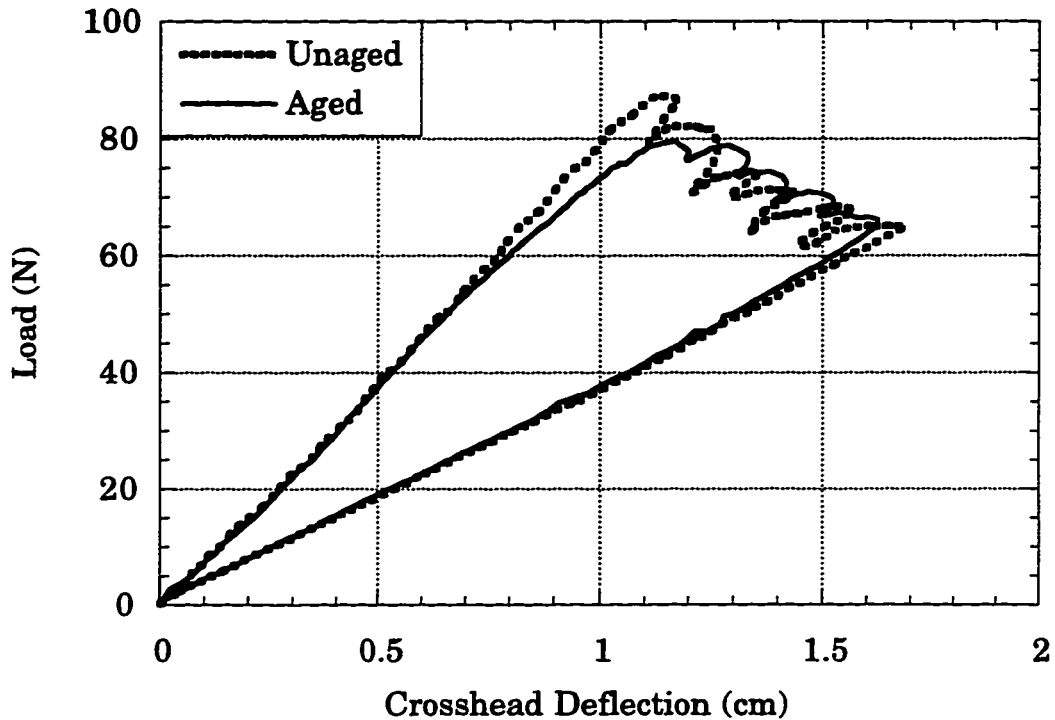


Figure 3.15 Comparison of aged and unaged DCB data for IM7/K3B

### 3.1.2 Mode II fracture toughness

Mode II fracture toughness specimens were tested using an ENF test specimen [32]. Calculation of  $G_{IIc}$  was made by using an analytical equation derived from linear beam theory. The equation is

$$G_{IIc} = \frac{9P_c^2 a^2 C}{2b(2L^3 + 3a^3)} \quad (3-2)$$

where  $P_c$  is the critical load,  $a$  is the initial crack length,  $C$  is the loading compliance,  $b$  is the specimen width, and  $L$  is the half span. Crack length was measured by splitting the specimen after the test and finding the initial crack tip, visible because of the distinctive appearance of the mode I pre-crack and the mode II fracture surface. A correction term for shearing effects was also added.

Data for  $G_{IIc}$  of specimens with no aging is shown in Figure 3.16. These data show fracture toughness for the thermoplastic K3B to decrease at higher temperature. The matrix material becomes more compliant at higher temperatures, which causes the critical load to decrease. The lower critical load directly causes lower  $G_{IIc}$ . For the thermoset 5260, the temperature effect is small.

Data for specimens that have experienced elevated temperature aging is difficult to interpret. Aging appears to cause both increases and decreases in mode II fracture toughness during the aging process. No significant trends could be observed from the data. The validity of measured  $G_{IIc}$  using the ENF method for polymeric materials at elevated temperatures is questionable. Therefore, data for the mode II fracture toughness of aged materials has not been included. Further discussion of the aging effects on mode II fracture toughness is published [36].

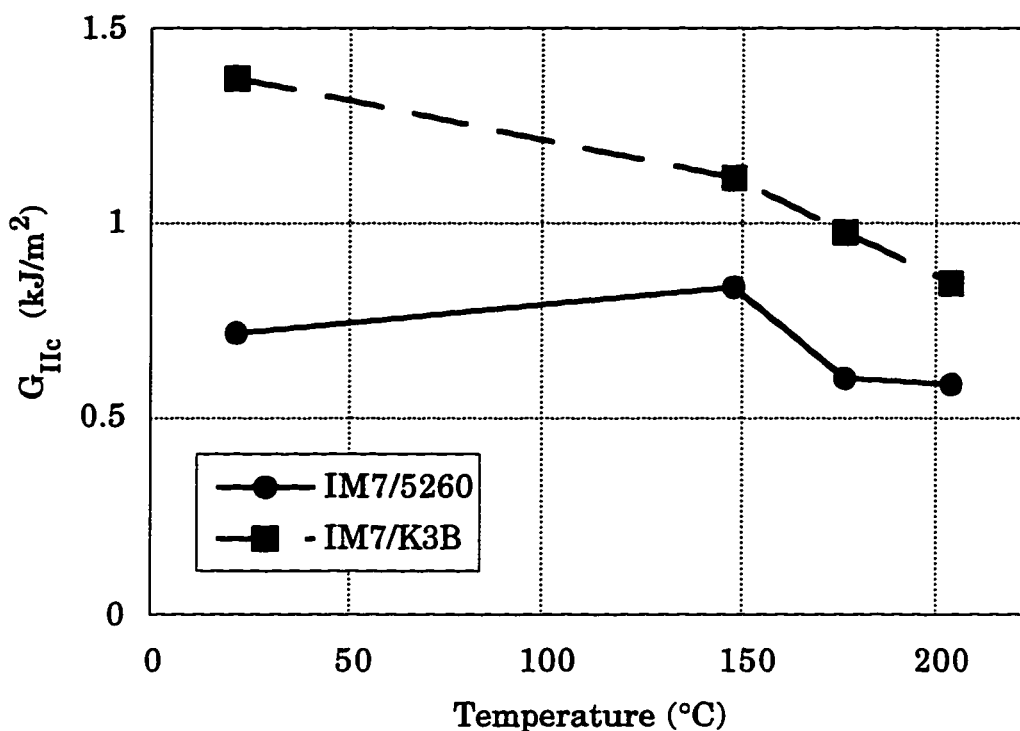


Figure 3.16  $G_{IIc}$  for unaged IM7/K3B

### 3.2 Microscopy studies

A study of the fracture surface discoloration was performed by microscopy [37]. Mode I and mode II fracture surfaces look distinct due to their surface textures. Mode I fracture surfaces have more matrix residue, with a broken appearance and large pieces of matrix material remaining attached to the fibers. Mode II fracture surfaces are more uniform, with the matrix broken in smooth surfaces and little residue. The difference between mode I and mode II surfaces is readily apparent in Figure 3.17.

The surface of discolored regions in 5260 specimens shows the degradation of the matrix material. The matrix is simply broken down and leached away during the aging process. This degradation is visible on all surfaces exposed to air. Figures 3.18 through 3.20 show unaged and aged tool surfaces, end surfaces, and cross section of the specimen surface, respectively. In each case, the aged surface shows bare fibers, stripped of matrix material. Also, cracks begin to develop in the matrix, which will accelerate the degradation process.

K3B does not suffer from this type of degradation. Most aged and unaged surfaces are very similar in appearance. Only in the case of aged mode II fracture surfaces is discoloration apparent. Under the microscope, the discolored region is still difficult to detect, but differences exist. For specimens aged at 149°C, the discoloration is due to increased smoothness of the fracture surface. The aged mode II fracture surface has even less material close to the fiber and fewer rough areas than the unaged mode II fracture surface. The discolored region is more difficult to define after aging at 204°C. Aging at this temperature causes an increase in the roughness of the surface, giving the appearance of a degraded plastic material. There is also change in color of the material, with the polymer becoming darker and more red in color. Specimens aged at 177°C show a combination of characteristics, having both a smoother surface and the reddish color. The discolored regions for IM7/K3B aged at 149°C and 204°C are shown in Figures 3.21 and 3.22.



Figure 3.17 Mode I and II fracture surface of IM7/K3B, 250X



Figure 3.18 Tool surfaces of unaged and aged IM7/5260, 500X



Figure 3.19 End surfaces of unaged and aged IM7/5260, 250X

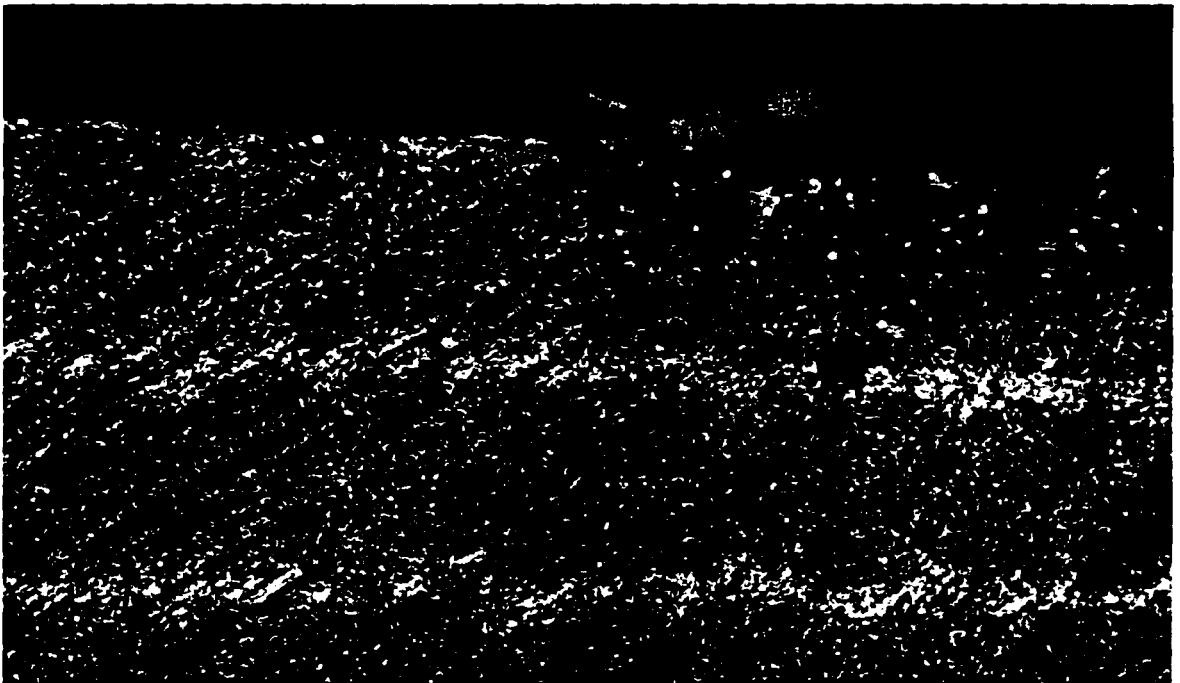


Figure 3.20 Cross section of unaged and aged IM7/5260, 500X

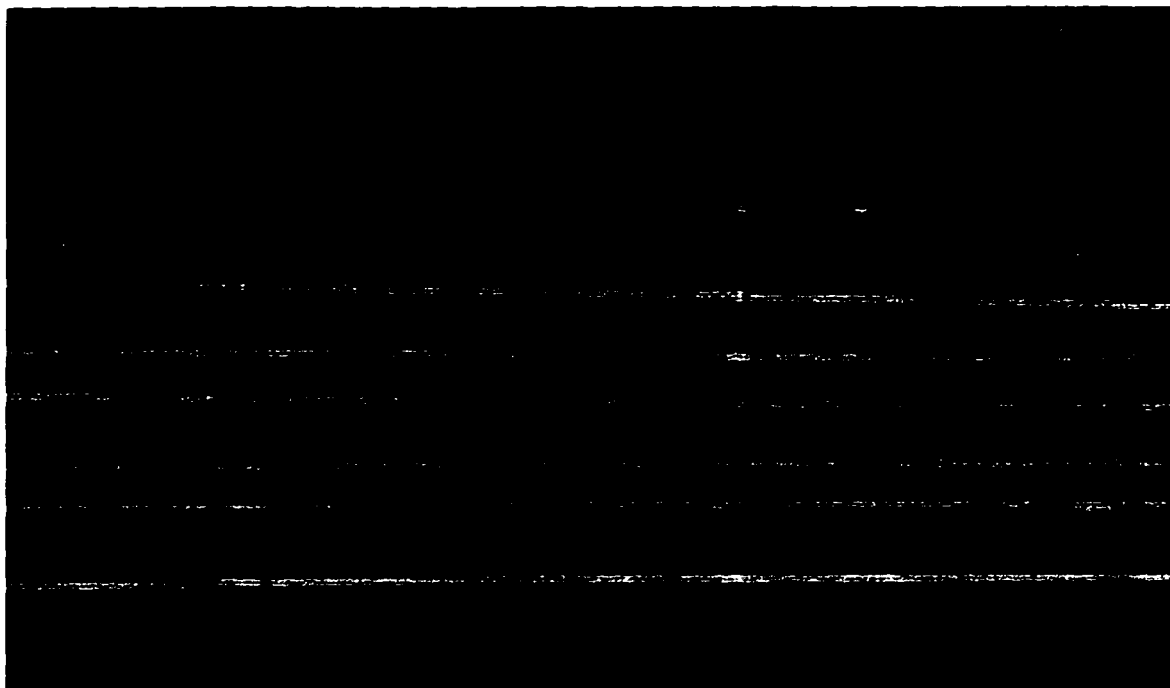


Figure 3.21 Discolored region in IM7/K3B aged at 149°C, 500X

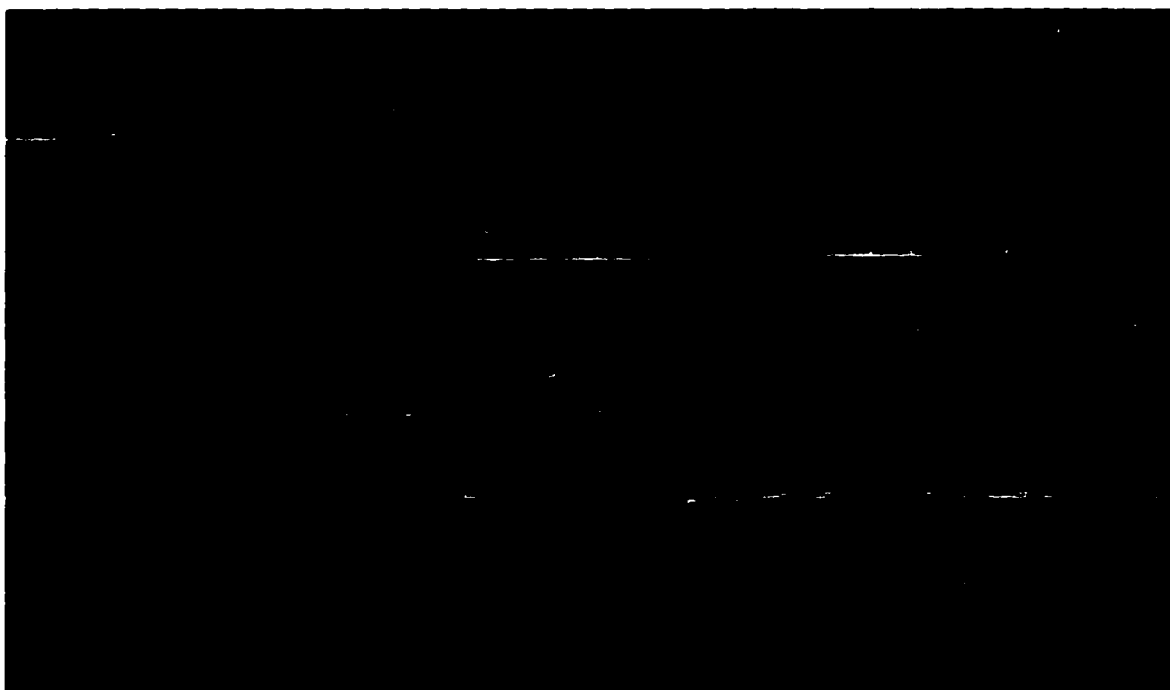


Figure 3.22 Discolored region in IM7/K3B aged at 204°C, 500X

### 3.3 Discoloration depth in aged composites

As mentioned in the previous subsection, ENF specimens were split after testing in order to locate the crack tip and analyze the fracture surface. The fracture surface for unaged material contained three distinct regions: the smooth surface from the delamination insert, the mode I pre-crack, and the mode II fracture surface. Aged specimens contained a fourth region, as shown in Figure 3.23. This region appeared within the mode II fracture surface, along all edges that had been exposed to air during aging. The surfaces were examined under high magnification to find the causes of the different appearance. In the interior regions, a thick coating of matrix material indicates fracture has occurred through the resin, away from the fibers. Regions near the edges of specimens aged at 149°C appear different because the fracture surface is along the interface between fiber and matrix. The edge discolored regions in specimens aged at 204°C fracture in the matrix, but have a different color. Specimens aged at 177°C showed a mixture of both types of discoloration.

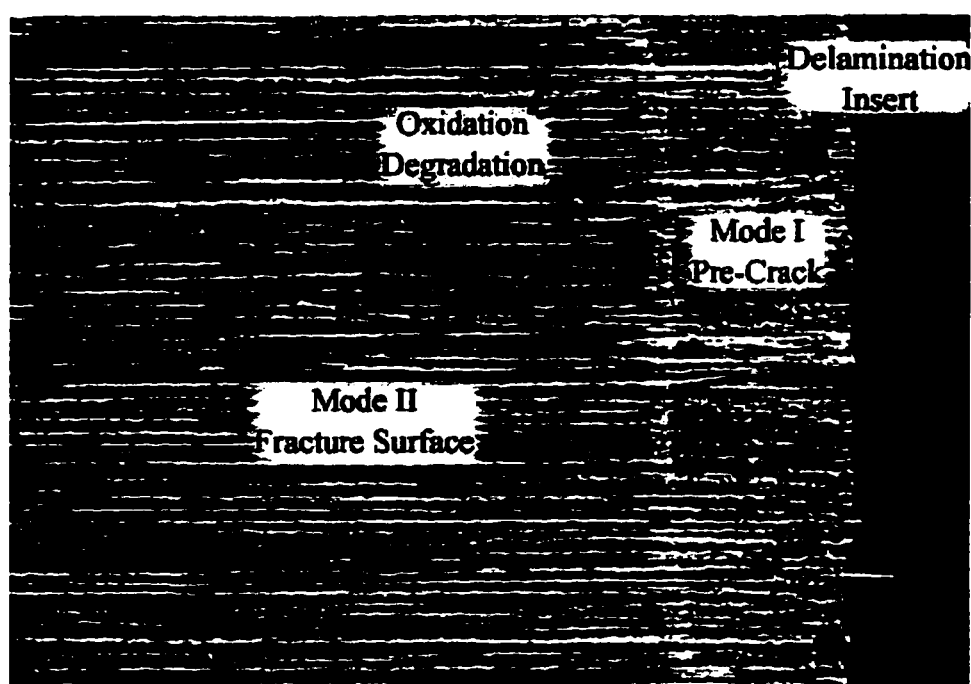


Figure 3.23 Fracture surface of an aged ENF specimen

The depth of the discolored region was measured for aged ENF specimens. Three different depth locations were measured: depth from the crack tip along the fibers, depth from the sides of the specimen transverse to the fibers, and depth from the end of the specimen parallel to the fibers. Discoloration depth parallel to the fibers was the same at the crack tip and at the specimen end. Therefore, only the crack tip location was studied.

To study the oxidation diffusion behavior, the discoloration depth parallel to the fibers at the crack tip and transverse to the fibers at the side of the specimen were measured for all ENF specimens. Discoloration depths parallel to the fibers for aged 5260 ENF specimens are shown in Figure 3.24. Depth transverse to the fibers is shown in Figure 3.25. Discoloration depth grows fastest along the fibers, a phenomena which correlates with the anisotropic weight loss behavior discussed in Chapter 2. The influence of fibers causes degradation parallel to the fibers to be roughly five times faster than degradation transverse to the fibers.

Degradation depth growth in 5260 is nearly linear with time, indicating reaction dominated oxidation behavior. That is, the diffusion is very fast compared to the chemical reaction and so reaction rate is the limiting factor in degradation depth growth.

Degradation depth in the third direction, perpendicular to the plane of the laminate plies, could not be measured. Polished sections were examined under a microscope, but degradation depth could not be determined accurately. Growth rate in this direction could be determined by observing the aging time of specimens with uniform discoloration over the fracture surface. This surface would indicate penetration through the thickness from the top or bottom of the specimen.

This type of discoloration was not observed in any 5260 specimens. Figure 3.25 shows that the largest degradation depth transverse to the fibers is roughly 0.06 cm. Specimen half thickness was 0.127 cm. Thus degradation growth in the third direction is less than in-plane degradation growth transverse to the fibers.

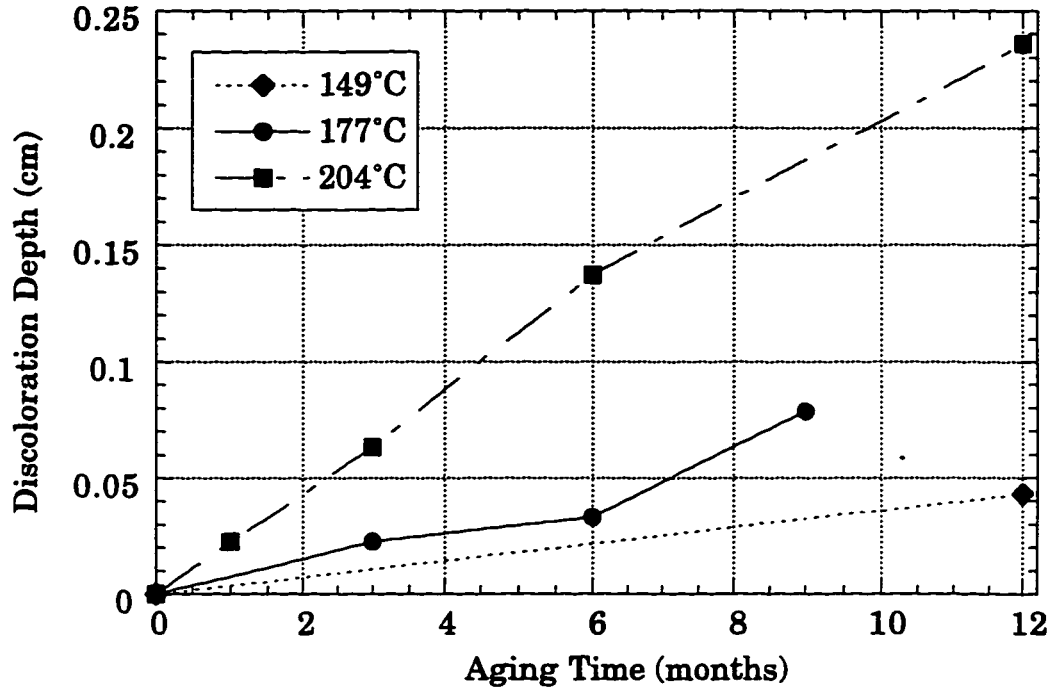


Figure 3.24 Discoloration depth parallel to the fibers in IM7/5260

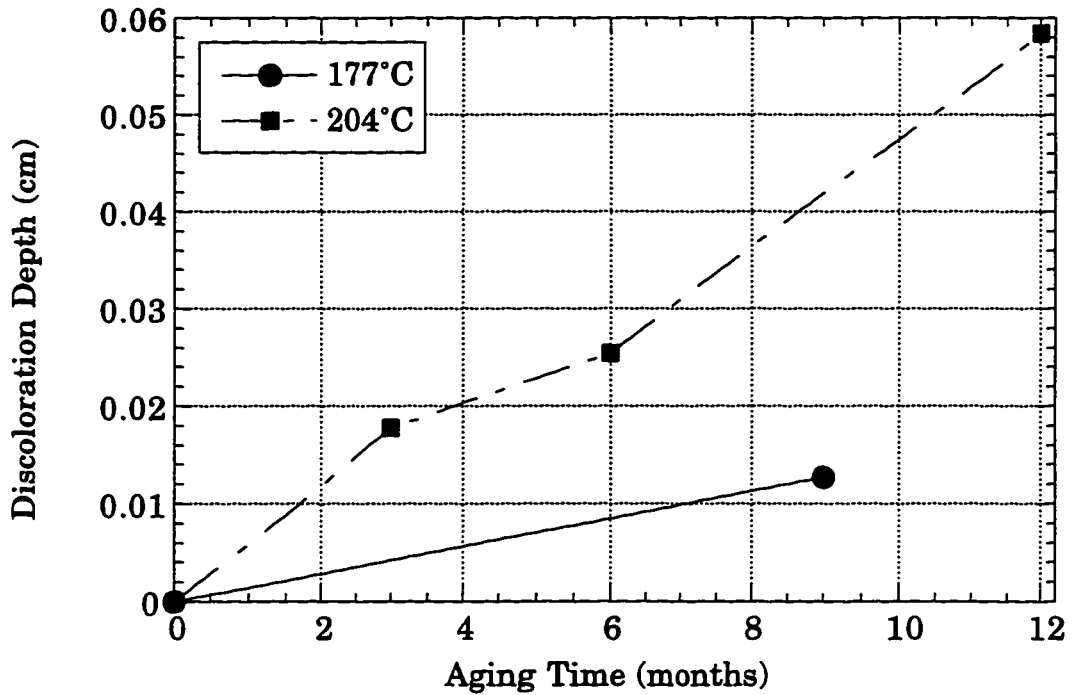


Figure 3.25 Discoloration depth transverse to the fibers in IM7/5260

Discoloration depth for K3B is shown in Figures 3.26 and 3.27. The depth of the discoloration zone grows faster than in 5260, but the reaction is not as distinct for the thermoplastic. For K3B, discoloration is found only on the mode II fracture surface while the degradation in 5260 is apparent in every type of specimen. The influence of fibers in K3B is small. The ratio of discoloration depth parallel to the fibers compared to the transverse direction ranges from twice as deep for two years of aging at 149°C to nearly equivalent for aging times less than six months. Discoloration depth growth in K3B is parabolic with time, indicating diffusion dominated oxidation behavior. That is, the diffusion is slow compared to the chemical reaction and so diffusion is the limiting factor in degradation depth growth.

Attempts to measure degradation growth through the thickness by viewing discoloration on cut edges of specimens were also unsuccessful in K3B. However, the fracture surfaces of K3B specimens aged at 149°C for 18 months appear discolored over most of the interior, indicating that degradation through the thickness had reached the midplane of the 20-ply specimens. This indicates that degradation in K3B at 149°C proceeds roughly half as fast in the z directions as in the y direction, and one quarter as fast as in the x direction.

In order to investigate the growth of the discoloration zone in CAI laminates, tested CAI specimens were depled and inspected. Deply was performed at room temperature by driving a wedge into the edge of the specimen and peeling off individual plies. The resulting surface showed delaminations due to impact, and discoloration due to aging in IM7/5260 specimens. Quasi-isotropic specimens with open-holes were also aged, and then depled to view the discoloration depth at the edge of the hole. K3B specimens showed no visible degradation, since discoloration was only seen on mode II fracture surfaces and the deply technique gives a mode I fracture. However, 5260 specimens had visible discoloration around the hole and edges of the specimen. Figure 3.28 shows a series of plies in a specimen aged at 204°C for seven months.

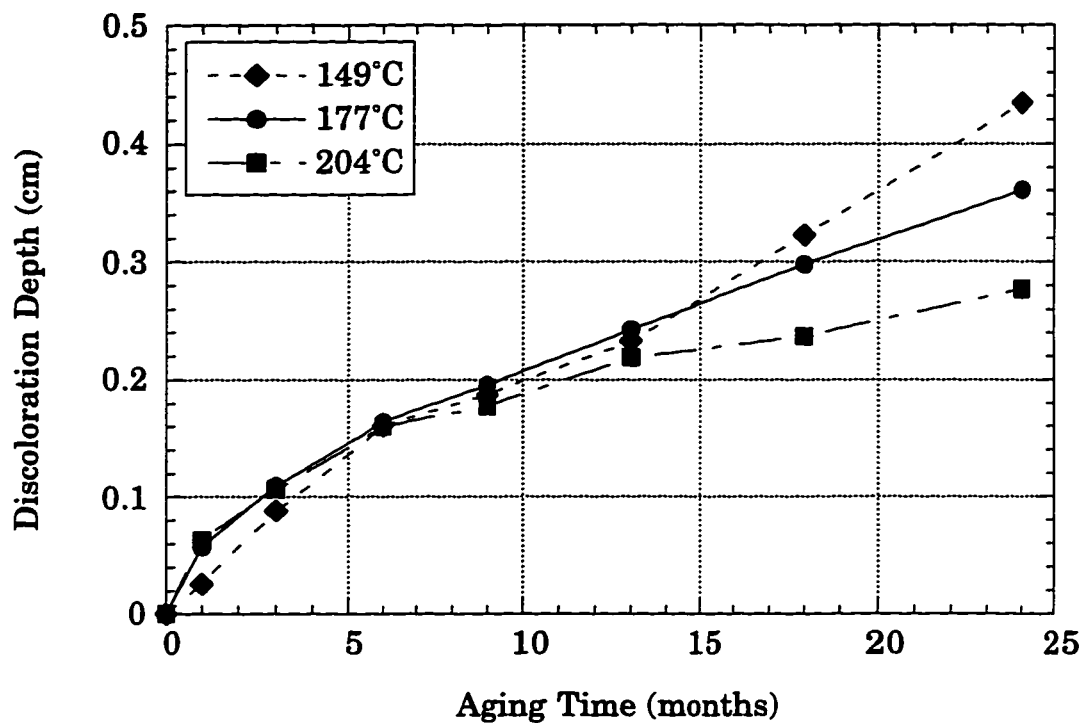


Figure 3.26 Discoloration depth parallel to the fibers in IM7/K3B

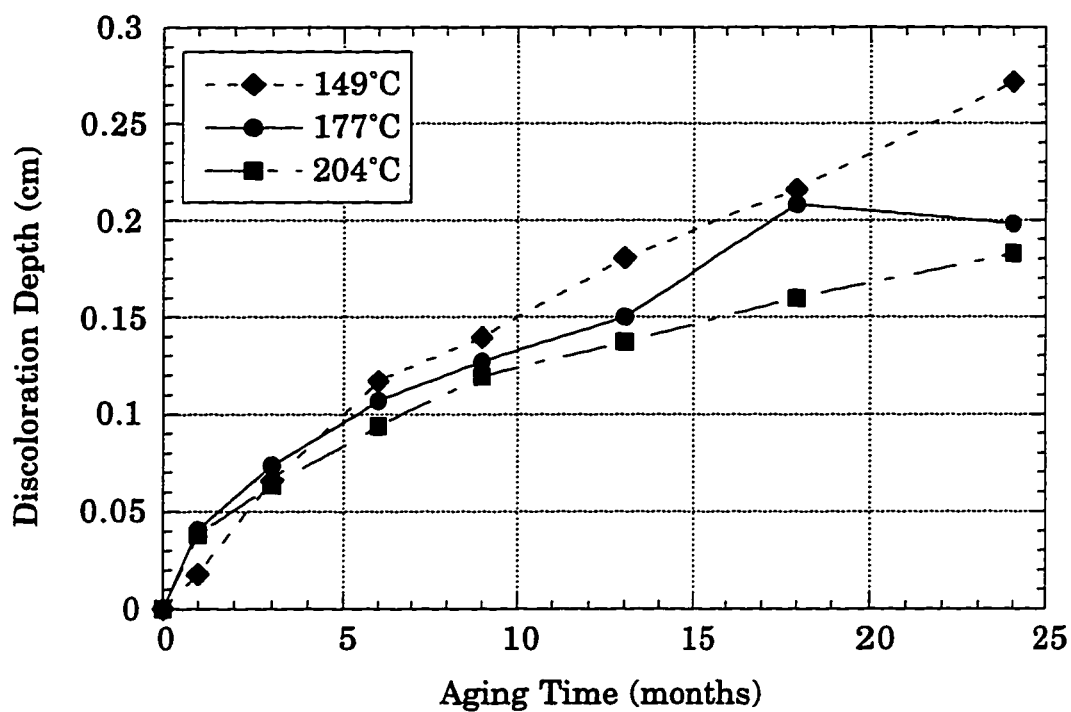


Figure 3.27 Discoloration depth transverse to the fibers in IM7/K3B

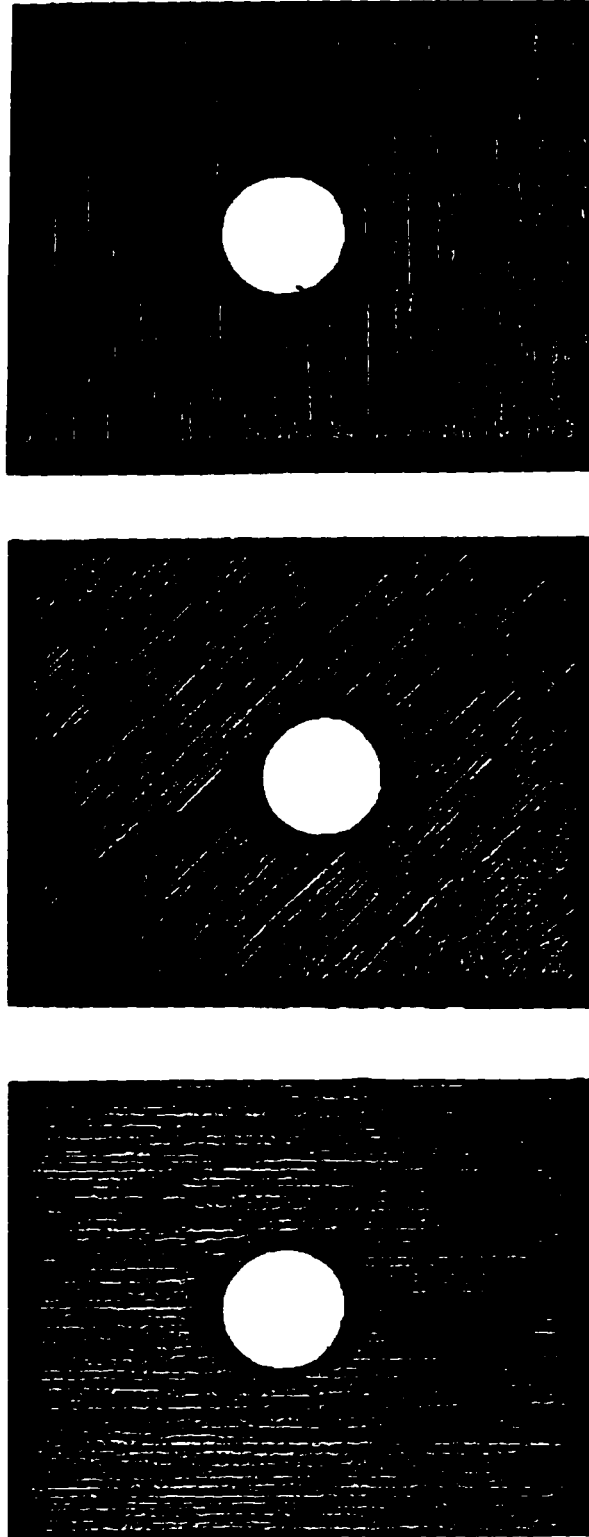


Figure 3.28 Degradation around an open hole in IM7/5260

### 3.4 Glass transition temperature

Measurements of the glass transition temperature ( $T_g$ ) of the aged specimens were obtained by Differential Scanning Calorimetry (DSC) [37]. This type of test determines the  $T_g$  by measuring the heat flux required to increase the temperature of a small (approximately 20 mg) sample at a specified temperature ramp rate. For most of the test, the heat flux will be a constant. However, when the material changes from the glassy state to the rubbery state, a different heat flux will be required to maintain the constant temperature rate, because of the change in molecular structure. This flux change is measured directly by DSC equipment.

The transition does not occur at a specific temperature. Rather, the transition occurs over a finite temperature range. There are several methods used to assign a specific  $T_g$  to this range [38]. The first point of flux increase is referred to as the onset temperature. This is useful for engineering applications, since this is the highest temperature attainable before stiffness properties begin to rapidly decrease. However, an endothermic peak occurred at the  $T_g$ . Therefore, the temperature at the peak of the endotherm was used for  $T_g$ .

The  $T_g$  can also be used as a measure of the completeness of cure for polymeric materials. As the material cures, polymer chain length increases and consequently the mobility of the polymers decreases. More energy is required to change the phase of the material, and thus the  $T_g$  increases. The thermoset 5260 has a higher  $T_g$  than the thermoplastic K3B because of the much higher cross-link density.

The change in  $T_g$  with aging is similar for both the thermoplastic and thermoset materials. The data in Figures 3.29 and 3.30 show that the manufactured material is not completely cured. Aging at 204°C completes the cure after a few months of aging. Post cure proceeds more slowly at lower temperatures. Complete cure would require several years of aging at 177°C, and material aged at 149°C is not likely to achieve a complete cure in the lifetime of the aircraft.

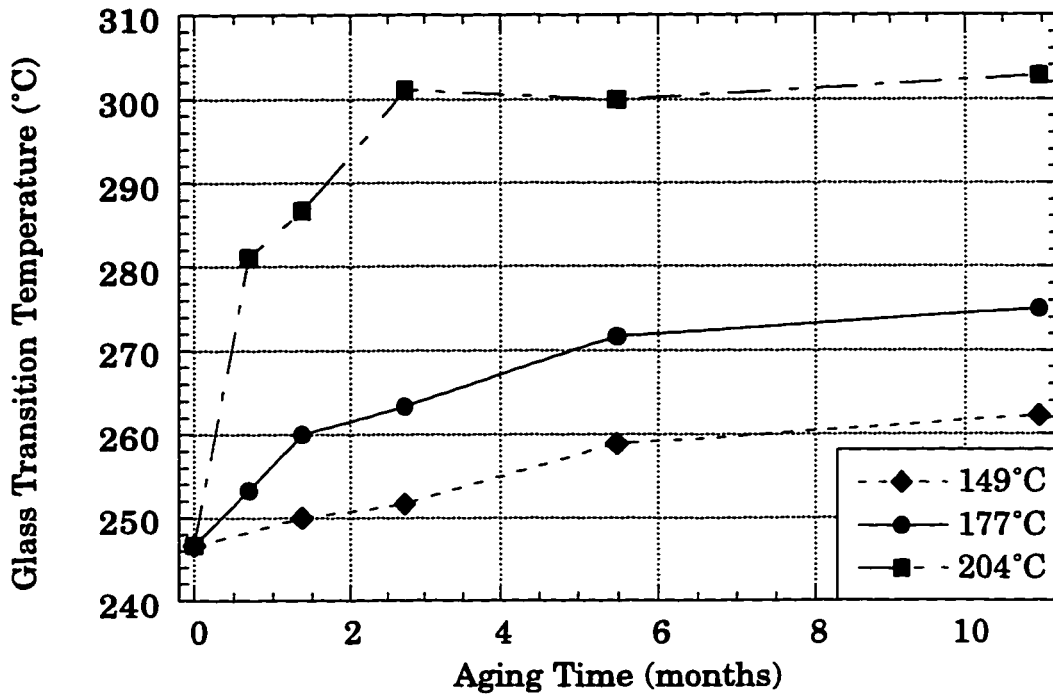


Figure 3.29 Glass transition temperature for IM7/5260

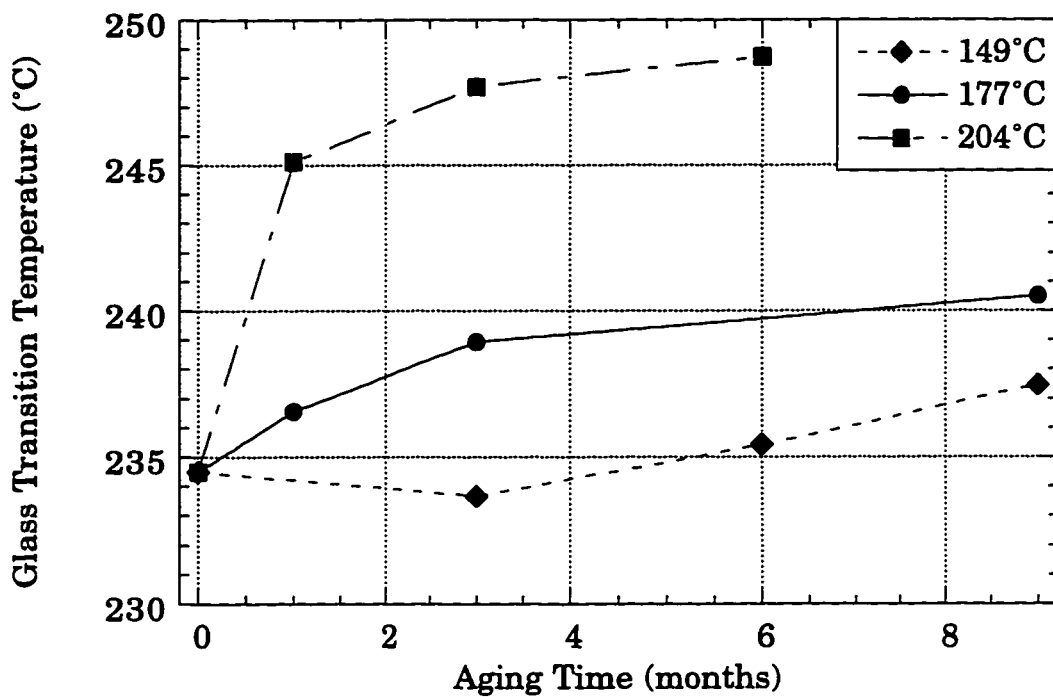


Figure 3.30 Glass transition temperature for IM7/K3B

During DSC testing, a large endotherm was seen as the material reached  $T_g$ . The size of the endotherm at  $T_g$  is a measure of the degree of physical aging which the material has experienced. The endotherm increased in magnitude at each time period in K3B specimens aged at 204°C, showing increased physical aging. The trend in specimens aged at 177°C was also toward larger peaks, although the data was scattered. Since there was no endothermic peak in tests of specimens aged at 149°C, physical aging is negligible at this temperature.

A small number of specimens aged at 204°C were heated above  $T_g$  before testing. Heating above  $T_g$  'rejuvenates' the matrix material, removing the effects of physical aging by returning the matrix to a high temperature equilibrium. The tests of rejuvenated specimens revealed somewhat lower  $T_g$ 's than other tests, indicating that physical aging had reduced the mobility of polymer molecules and increased the  $T_g$ . The  $T_g$ 's measured in tests of rejuvenated specimens were still higher for aged specimens than for unaged specimens. This indicates that the increase in  $T_g$  is due to both chemical and physical aging.

### 3.5 ESCA analysis

Electron Spectroscopy for Chemical Analysis (ESCA) is a highly sensitive method of finding the relative numbers of different types of chemical bonds within 80 Å of a surface. A very basic explanation is given here, but more detailed descriptions are available in the literature [39]. An x-ray source exposes the material to radiation with a specific energy. This radiation penetrates the surface of the material, and stimulates electron emission from the inner shells of the atoms. By measuring the energy of the emerging electrons, the binding energy of the atoms can be found. Each atomic species has a signature energy spectrum that is very easy to read from the data. More significantly, the environment of the atom causes a slight shift in the binding energy. This allows the interatomic bonding to be measured, leading to a determination of the molecular structure.

Results from ESCA testing of IM7/K3B agreed well with the chemical structure. Composition was 81% carbon, 14% oxygen, and 5% nitrogen as predicted. Only one species of nitrogen, or one type of nitrogen bond, was present. Oxygen and carbon species were more difficult to determine, but also agreed with the predicted structure. The chemical structure is similar to Poly(ether imide)(KaptonHN)(KAP) [40], and the spectral data obtained in this study agreed well with the reference spectrum. It is significant that the spectral data from the graphite fiber reinforced composite agreed so precisely with the chemical structure of the neat resin. This indicates that the matrix material remained bonded to the fibers everywhere, leaving no bare fibers.

Extensive testing of K3B mode I and mode II fracture surfaces showed no changes in bond structure with aging time or sampling location. Measurements were taken on surfaces exposed to oxygen during aging, mode I fracture surfaces, discolored mode II surfaces, and interior surfaces. Because of the very rough contours of the fracture surface, the difficulty in charging a non-conductive substance, and the heterogeneity of the material, precise measurements were difficult to obtain. The absolute accuracy of the qualitative measurements obtained for this material were estimated to be no better than 5%. Also, only a few chain scissions per thousand monomers can significantly alter the molecular weight and thus the polymer properties. Therefore, oxidation degradation was not ruled out from the lack of change in ESCA data.

### 3.6 TOF-SIMS tests

Secondary Ion Mass Spectroscopy (SIMS) measures the molecular weight of particles released from the surface of a material by a bombardment of ions. For this study, the positive ion source was Cesium operating at 8 keV. These ions knock out secondary ions from the upper 20 Å of the specimen. Secondary ions are collected by a Time-Of-Flight (TOF) analyzer, which provides a precise measurement of the atomic mass and atomic number of each particle coming from the surface.

Four surfaces were analyzed. A mode I and a mode II surface on unaged material produced nearly identical data. A typical spectrum for this surface is shown in Figure 3.31. The low mass particles below 30 m/z are carbon, oxygen and nitrogen in single or double atom units. Particles between 30 and 100 m/z are combinations of four or five atoms. Again, these ions are composed of carbon, oxygen, nitrogen and hydrogen atoms.

The clusters of data around 150 and 300 m/z are derived from the molecular unit shown in Figure 3.32. This structure is one of the two monomers in avimide K3B. During SIMS testing, the monomer is broken apart. The most common structure in the group just below 150 m/z is depicted in Figure 3.33.

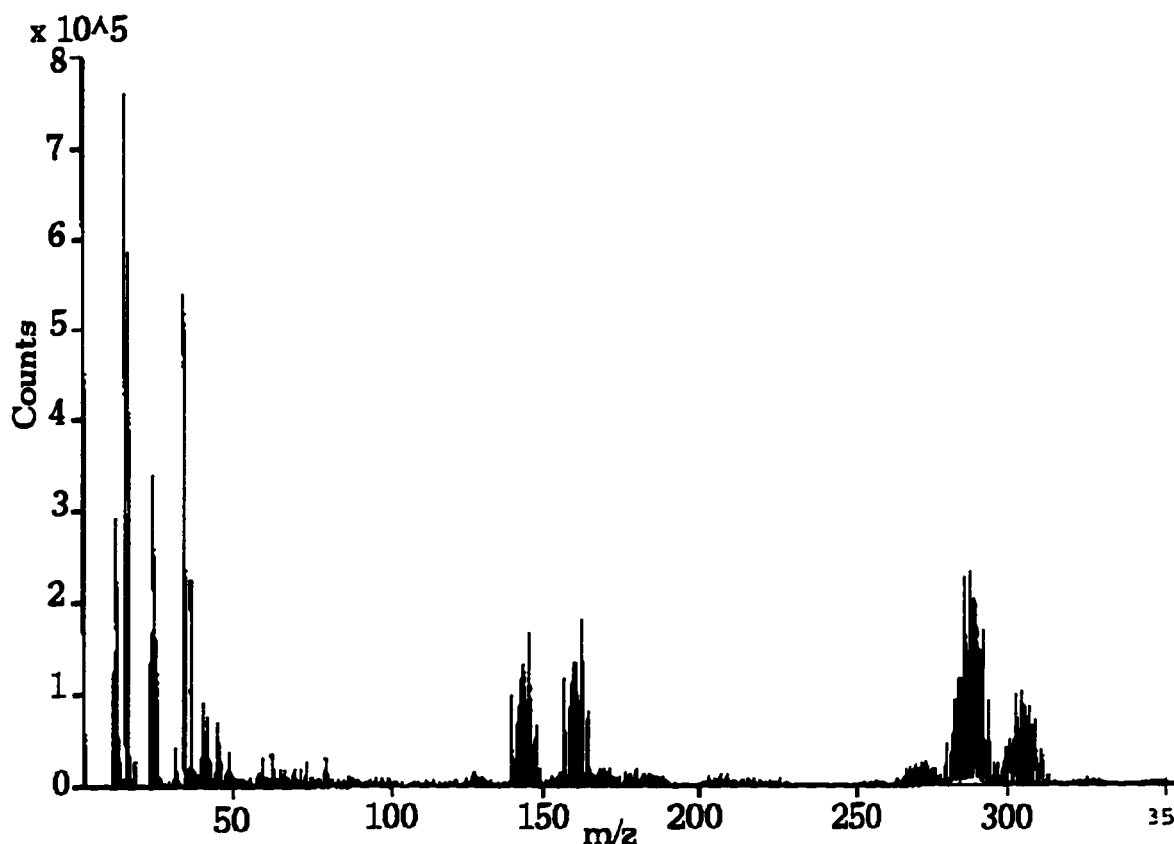


Figure 3.31 Typical SIMS spectrum for unaged K3B

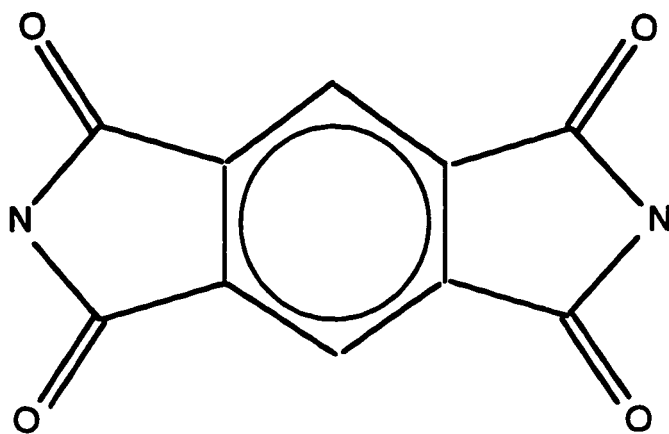


Figure 3.32 Chemical structure of K3B monomer

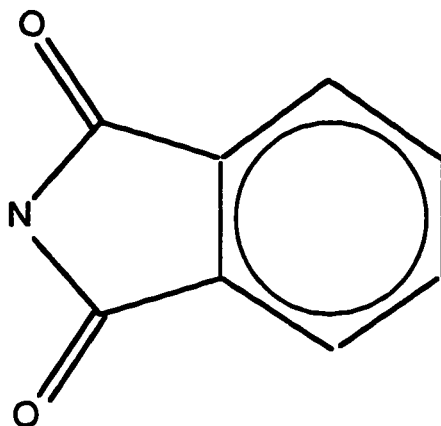


Figure 3.33 Chemical structure of secondary ions in K3B

Other structures in the group are formed by adding or subtracting hydrogen, and by replacing oxygen with nitrogen or carbon. The group of structures just above 150 m/z duplicates the pattern exactly. The difference between the groups is 17 m/z, the equivalent of an OH group. The structures of the lower group near 300 m/z are formed by doubling the unit shown in Figure 3.33, and again the higher group is formed by adding an OH group.

One specimen aged for eighteen months at 204°C was analyzed with SIMS. The surface was from mode I fracture toughness testing, in a region directly exposed to air during elevated temperature aging. No differences were seen in the mass spectrum. K3B was completely resistant to the oxidation degradation on this surface.

Finally, the discolored region on the mode II fracture surfaces of K3B aged two years at 149°C was analyzed. As shown by microscopy, this surface was much closer to the fibers, in or near the region of the interphase between fiber and matrix. The high mass spectrum for this surface was very different from the previous three spectra, as shown in Figures 3.34 and 3.35. Please note the scale in these figures. The groupings surrounding 150 m/z and 300 m/z were close to the level of background noise in the discolored region of the aged material. In comparison to the unaged material, the groups are absent in the aged material. Smaller groups were more abundant in the aged material. This data shows that during aging, the bonds surrounding the nitrogen atom are broken down.

This degradation occurs only in the interphase, and so is only visible on a mode II shear surface. Only the mode II surface is close enough to the fibers to be influenced by the chemistry of the fiber/matrix bond. This chemical degradation in the interphase is the cause of decrease in CAI strength. Shear strength will decrease through the loss of bonding strength between fiber and matrix. The compressive strength of 0° plies is sensitive to changes in the interlaminar shear strength [41].

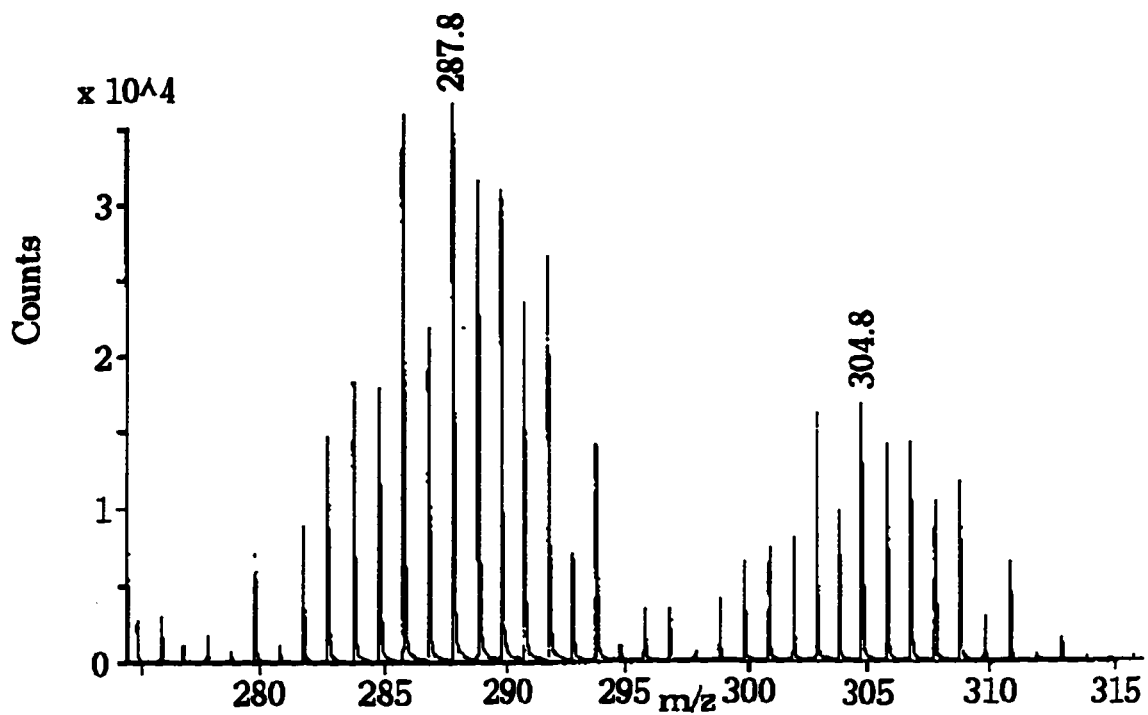
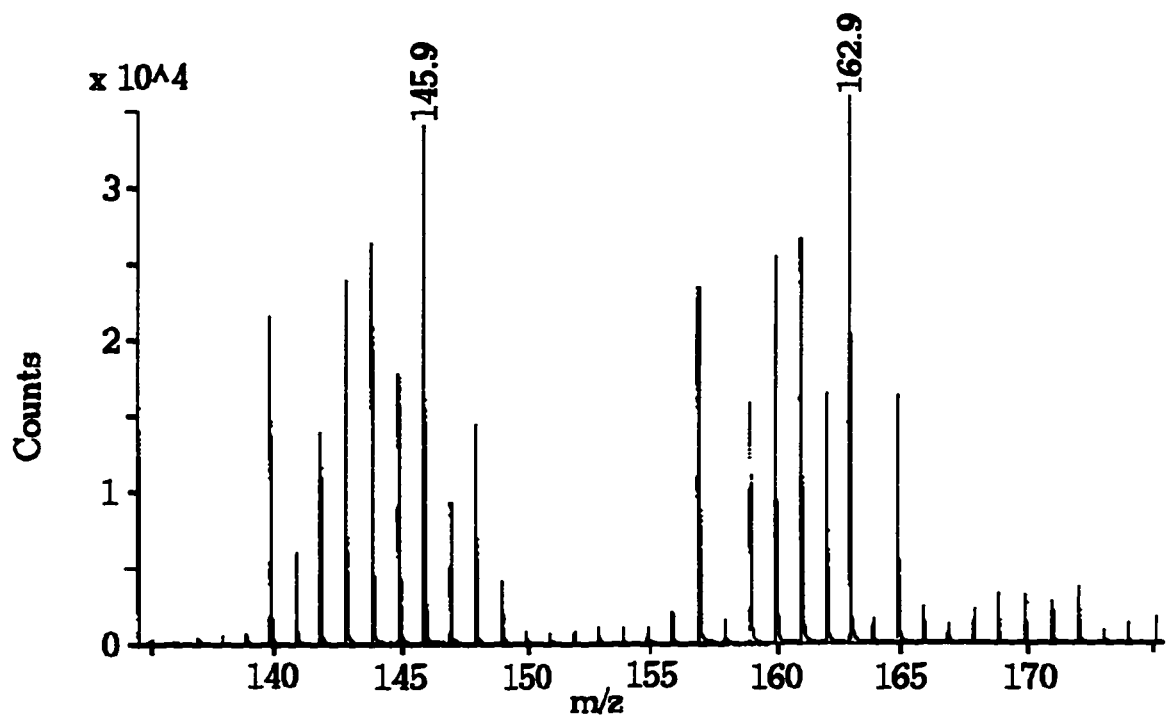


Figure 3.34 Scan of high mass groups on an unaged mode II surface

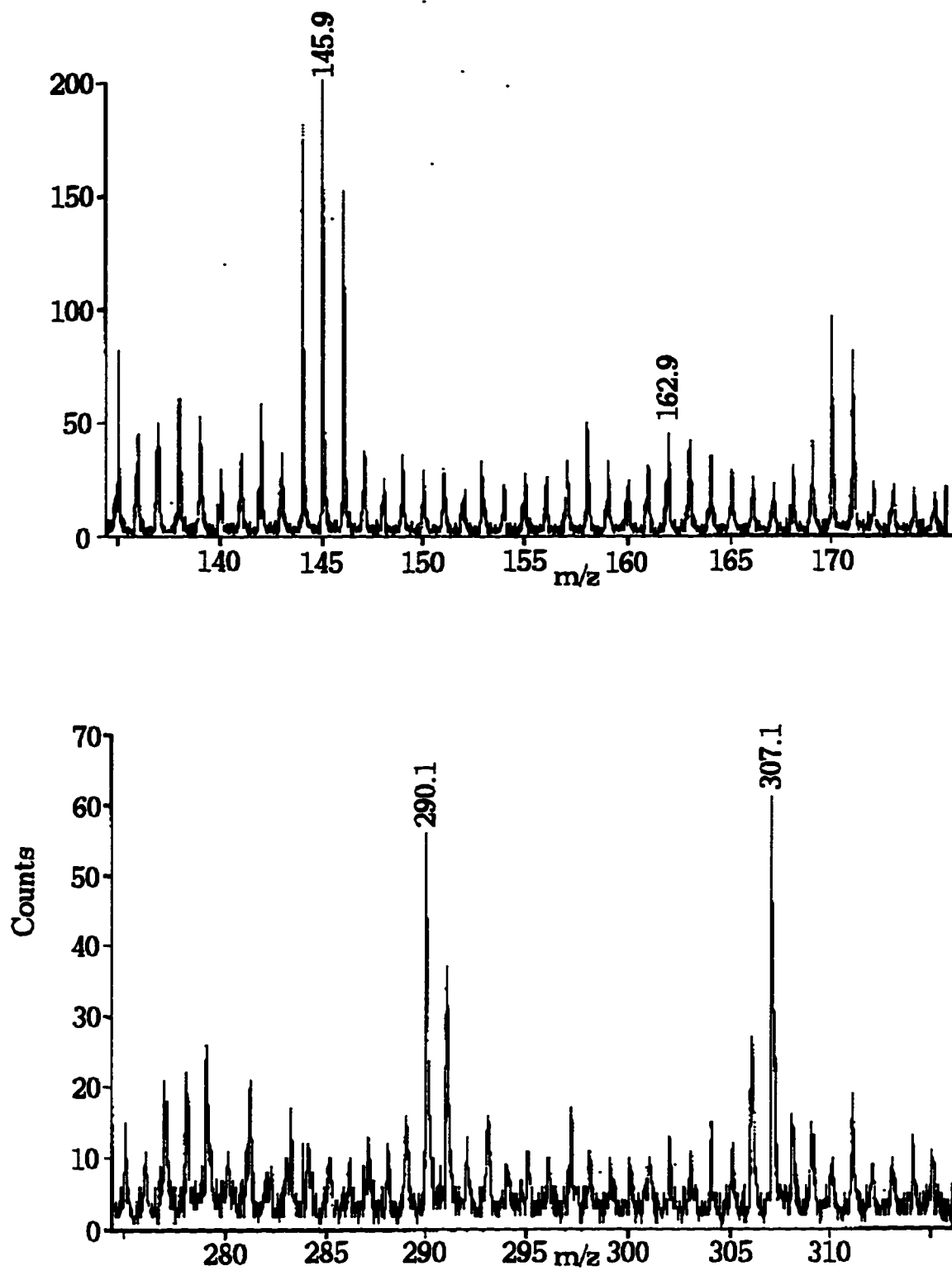


Figure 3.35 Scan of high mass groups on an aged mode II surface

### 3.7 Four point bend strength

Ply compressive strength was investigated utilizing the four point bend test [42]. Specimens were cut from 50 ply unidirectional panels, with the fibers parallel to the length. Specimen dimensions were 14 cm long with a 0.6 cm square cross section. Load was applied as shown in Figure 3.36, putting the center section of the specimen in pure bending. Center displacement was measured during testing using a dial gage indicator. A displacement rate of 0.06 cm/min was applied until failure, defined as the first drop in load and usually accompanied by audible fiber failure. Since failure strength along the fiber direction is greater in tension than compression, specimens always failed on the compressive surface. The ply compression strength was calculated by the equation

$$\sigma_f = \frac{3PL}{4bd^2} \quad (3-3)$$

where P is load at failure, L is the support span, b is the specimen width and d is the specimen thickness.

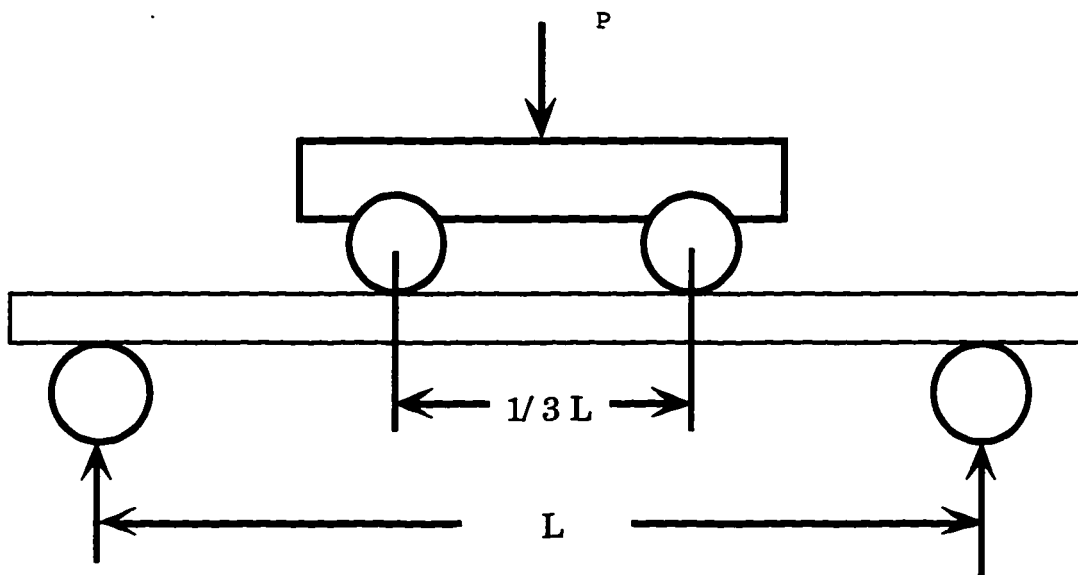


Figure 3.36 Schematic diagram of four point bend testing

Specimens were aged at 149°C for 3 and 6 months and at 204°C for 1 and 3 months. The degradation of the compression strength is shown in Figures 3.37 and 3.38. Aging at 149°C does not affect IM7/5260, while IM7/K3B strength decreases 10% after 6 months of aging. IM7/5260 decreases 25% and IM7/K3B decreases 5% after three months of aging at 204°C. This degradation is very similar to CAI strength degradation, and will be discussed further in Chapter 7.

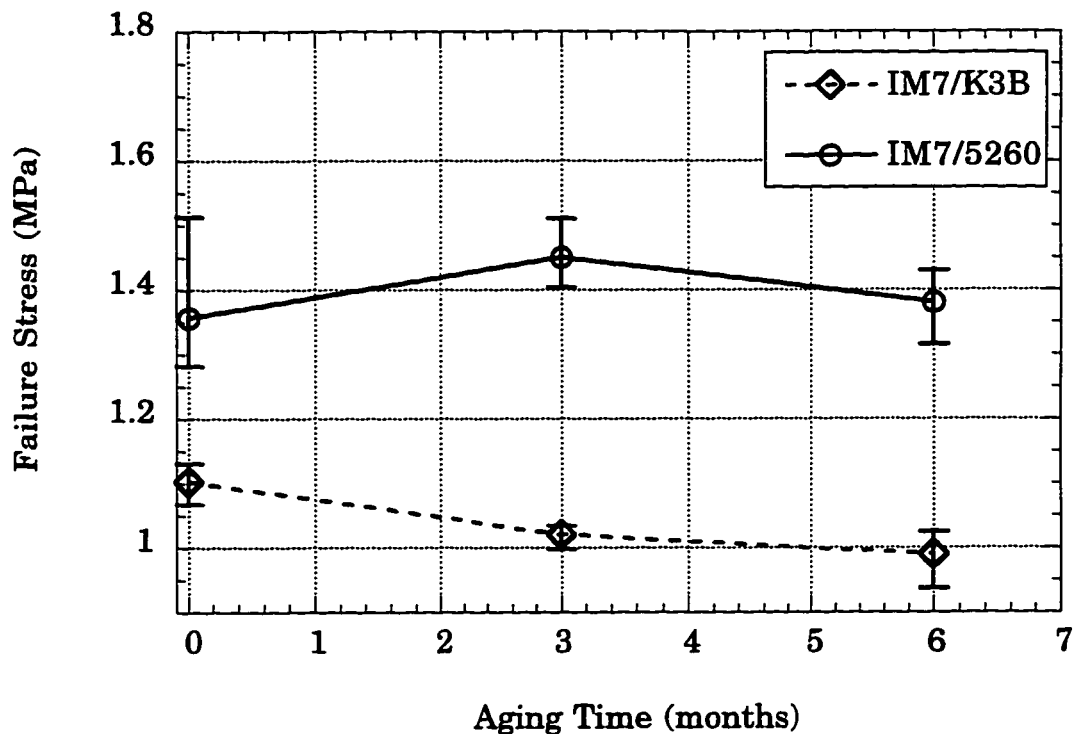


Figure 3.37 Degradation of compressive strength in four point bend specimens aged at 149°C

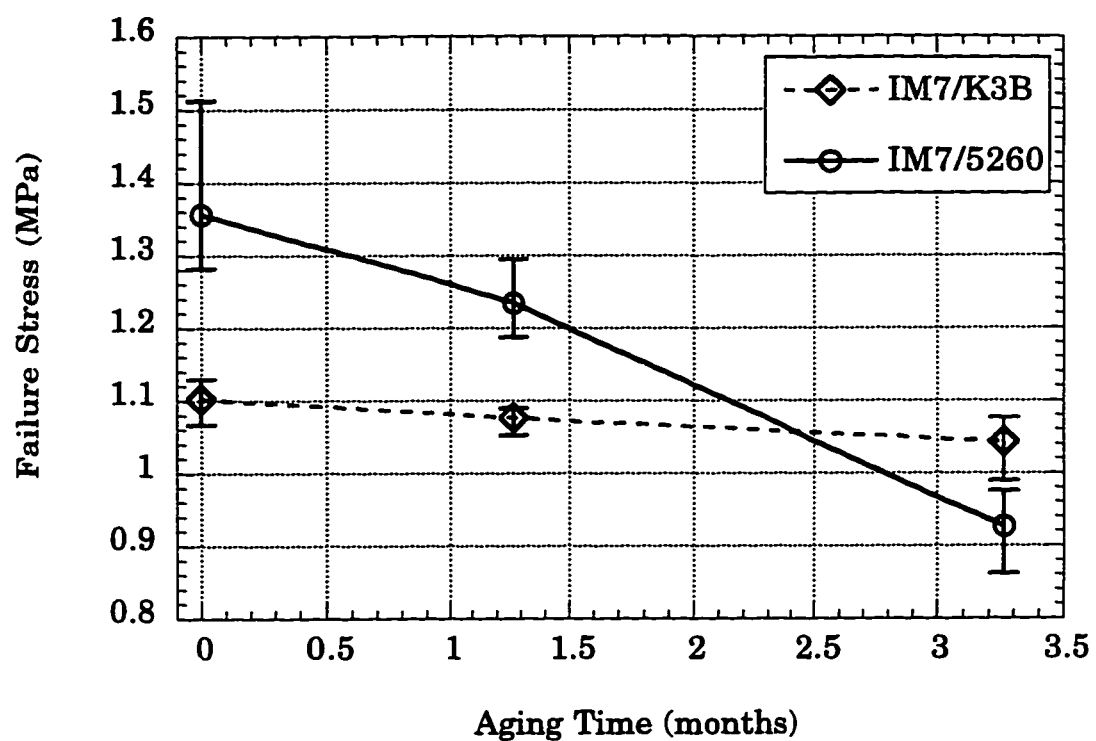


Figure 3.38 Degradation of compressive strength in four point bend specimens aged at 204°C

## Chapter 4

### DIFFUSION/REACTION MODEL

The discoloration zone in the composite material is due to thermo-oxidation. During elevated temperature aging, oxygen in the air diffuses into the specimen from exposed surfaces. The oxygen reacts with the polymeric matrix, forming the discolored material. The diffusion of oxygen into the composite and subsequent degradation reaction are analytically modeled in this chapter.

#### 4.1 Formulation using conservation of mass

The discoloration depth measured on fracture surface specimens in Section 3.3 is one dimensional diffusion and reaction. In one dimension, a closed form solution is possible. The formulation is presented by Ghez in [43], and will be discussed here. The resulting equations will be used to analyze the discoloration depth data from mode II fracture toughness surfaces.

##### 4.1.1 Analytical solution

The equation for the depth of the degraded region is formulated by modeling the process of oxygen diffusion and reaction. In air, the oxygen will have a partial pressure designated by  $p$ . Oxygen dissolves into the polymer surface to give the surface an oxygen concentration of

$$C_o = Kp \quad (4-1)$$

where  $K$  is a solubility constant that depends on temperature. Once on the surface of the specimen, the oxygen diffuses through the degraded region according to Fick's law. It is assumed that the oxidation reaction is complete within the degraded region, and therefore no further reaction between the oxygen and the polymer occurs within this area.

Fickian diffusion is governed by the equation

$$\frac{\partial C}{\partial t} = \frac{\partial}{\partial x} \left( D \frac{\partial C}{\partial x} \right) \quad (4-2)$$

where  $D$  is the diffusivity constant. Within the degraded region, diffusivity is assumed constant so equation (4-2) becomes

$$\frac{\partial C}{\partial t} = D \frac{\partial^2 C}{\partial x^2} \quad (4-3)$$

After diffusing through the degraded region, the oxygen reacts with the polymeric matrix at the boundary. The reaction rate is assumed to be first order, and dependent only upon the temperature.

$$r = kC_L \quad (4-4)$$

The reaction rate has units of flux and represents the flow of oxygen from the diffused state into the reacted material. The level of oxygen in the degraded region is depicted in Figure 4.1.

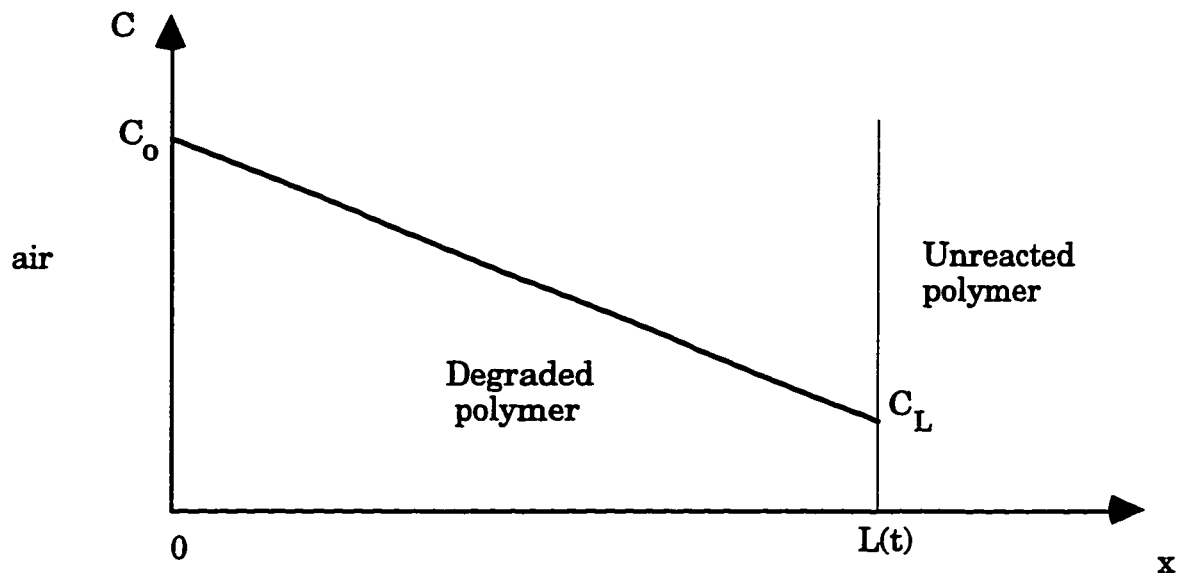


Figure 4.1 Concentration of diffused oxygen at the surface of an aged polymeric composite [43]

Since the diffusion/reaction process is very slow, the diffusion at any point in time is assumed to be steady state. For steady state diffusion, equation (4-3) is set equal to zero and the equation for concentration is

$$C(x,t) = \alpha + \beta x \quad (4-5)$$

were the terms  $\alpha$  and  $\beta$  are constants. Of course, the distance  $L$  is a function of time, so the process cannot be exactly modeled with steady state equations. To account for this time dependence, the assumption of quasi-steady state condition is assumed. That is, equation (4-5) is used, but the terms  $\alpha$  and  $\beta$  are now weakly dependent on time.

The problem of finding the distance  $L$  as a function of time is solved by using mass conservation for the diffused oxygen over the degraded region. Mass conservation is balanced with flow at the boundaries of the degraded region. Oxygen is bound within the polymer molecules, but only diffused free oxygen is considered in the equations.

The mass of molecular oxygen is the integral of the concentration over the width of the degraded region.

$$M_{O_2}(t) = \int_0^{L(t)} C(x,t) dx \quad (4-6)$$

The changes in mass are of primary interest so the time derivative of equation (4-6) is taken. Using the Leibnitz rule, the equation becomes

$$\dot{M}_{O_2}(t) = \int_0^{L(t)} \frac{\partial}{\partial t} C(x,t) dx + \dot{L}C(L,t) \quad (4-7)$$

Equation (4-3) substitutes into equation (4-7) to give

$$\dot{M}_{O_2}(t) = \int_0^{L(t)} D \frac{\partial^2 C}{\partial x^2} dx + \dot{L}C(L,t) \quad (4-8)$$

Evaluating the integral yields

$$\dot{M}_{O_2}(t) = D \frac{\partial C_L}{\partial x} - D \frac{\partial C_0}{\partial x} + \dot{L}C_L \quad (4-9)$$

The change in mass within the area must be equal to the flow through the boundaries. At the boundary between degraded material and the bulk of the composite material, the flow of oxygen out of the degraded region is equal to the reaction rate of the oxygen, given by equation (4-4). By definition of the diffusivity constant, the flux of diffused oxygen at the surface of the composite is

$$J_0 = D \frac{\partial C_0}{\partial x} \quad (4-10)$$

Summing the flow through both boundaries,

$$\dot{M}_{O_2} = kC_L - D \frac{\partial C_0}{\partial x} \quad (4-11)$$

The time derivative of mass is eliminated from equations (4-9) and (4-11) to give the equilibrium equation at the moving boundary.

$$D \frac{\partial C_L}{\partial x} - kC_L + \dot{L}C_L = 0 \quad (4-12)$$

An expression for the time derivative of length in terms of the concentration is found by evaluating the mass of the reacted oxygen. This is the oxygen added to the polymer molecules during thermo-oxidative aging, not including oxygen already present in the unaged polymers. The reaction is assumed to produce a constant concentration of reacted oxygen with the degradation zone. Using the specific volume of the reacted oxygen,  $v$ , the total mass of reacted oxygen is simply

$$M_{O_2}(\text{reacted}) = \frac{L(t)}{v} \quad (4-13)$$

The specific volume is a constant with respect to time, so the rate of change in the mass is equal to

$$\dot{M}_{O_2}(\text{reacted}) = \frac{\dot{L}(t)}{v} \quad (4-14)$$

The only flow of reacted oxygen in or out of the region is at the reaction boundary. The change in the reacted mass is equal to the reaction rate. Setting equation (4-14) equal to equation (4-4)

$$\dot{L}(t) = vkC_L(t) \quad (4-15)$$

Using the assumption of a quasi-steady state diffusion, equation (4-5) gives the concentration as a function of location within the degraded region. Using the concentration profile shown in Figure 4.1, the coefficients for equation (4-5) are

$$\alpha = C_0 \quad \beta = \frac{C_0 - C_L}{L} \quad (4-16)$$

The spatial derivative of concentration is then

$$\frac{\partial C}{\partial x} = \frac{C_L - C_0}{L} \quad (4-17)$$

Substituting equations (4-17) and (4-15) into the equilibrium equation (4-12) gives the equation

$$D \frac{C_0 - C_L}{L} + kC_L + kvC_L^2 = 0 \quad (4-18)$$

For the case of thermo-oxidation in a polymeric composite, the term  $kvC_L$  is much smaller than 1. The squared term can then be neglected to give an expression for the concentration of molecular oxygen at the degradation boundary.

$$C_L = \frac{C_0}{1 + k \frac{L}{D}} \quad (4-19)$$

Equation (4-19) is then substituted into equation (4-17) to give

$$\dot{L} = \frac{vkC_0}{1 + k\frac{L}{D}} \quad (4-20)$$

Using separation of variables with the initial condition that  $L(0) = 0$ , the relation between time and degradation depth becomes

$$t = \frac{L}{vkC_0} + \frac{L^2}{2vDC_0} \quad (4-21)$$

The expression has a linear term and a parabolic term. The linear term is dependent on  $k$ , the reaction rate, indicating degradation dominated by the thermo-oxidative reaction will have linear depth with respect to time. The diffusion term is parabolic with time. When diffusion dominates the degradation process, the degradation depth will proceed as  $t^{1/2}$ .

#### 4.1.2 Experimental parameters

The terms  $v$  and  $C_0$  are material property parameters independent of time and temperature. For the purpose of experimental analysis, these terms will be combined into the reaction rate constant and the diffusivity by the equations

$$\kappa = vkC_0 \quad D' = 2vDC_0$$

The data from Section 3.2 was used to find values of  $\kappa$  and  $D'$ . Table 4.1 lists the values for IM7/5260 and IM7/K3B. For both K3B and 5260, the reaction rate follows the Arrhenius equation

$$\theta = \alpha \exp(-E/RT) \quad (4-22)$$

where  $\alpha$  is a constant,  $E$  is the activation energy of the process,  $R$  is a material dependent constant, and  $T$  is temperature. The variable  $\kappa$  follows this type of temperature dependence for both materials, as shown in Figures 4.2 and 4.3.

Table 4.1 Experimental parameters for degradation growth

Material	Aging Temperature	$\kappa$	D'
IM7/5260	149°C	0.010	14,000
IM7/5260	177°C	0.021	-0.016
IM7/5260	204°C	0.100	0.327
IM7/K3B	149°C	0.126	0.191
IM7/K3B	177°C	0.376	0.091
IM7/K3B	204°C	0.592	0.050

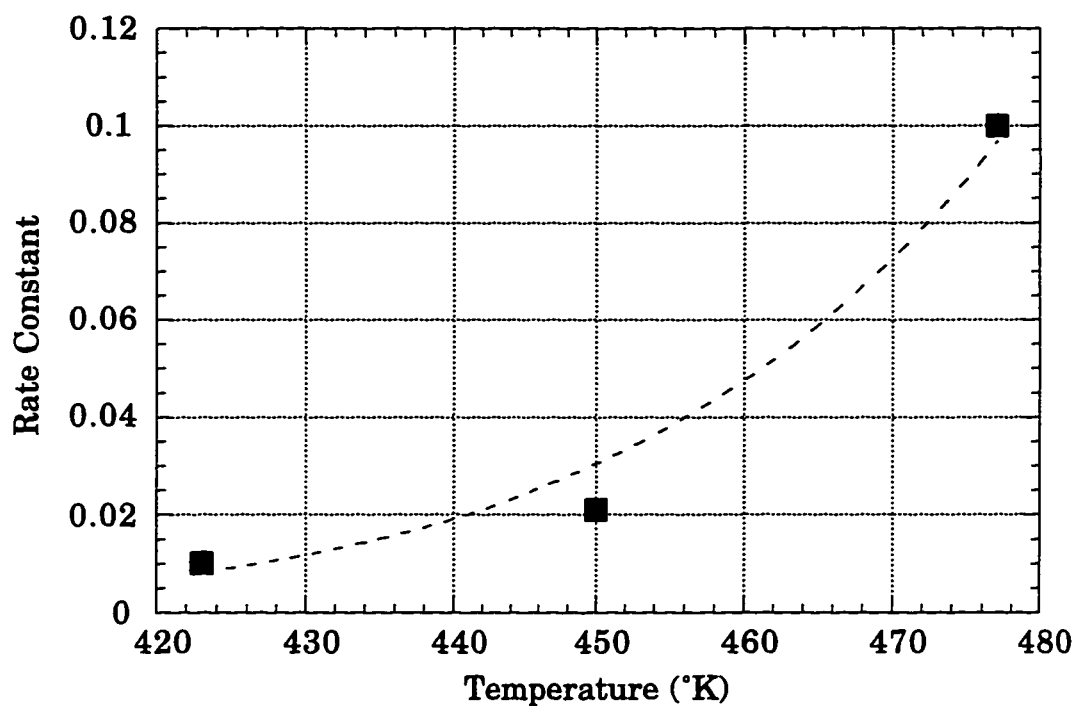


Figure 4.2 Temperature dependence for the reaction rate of thermo-oxidative degradation parallel to the fibers in IM7/5260

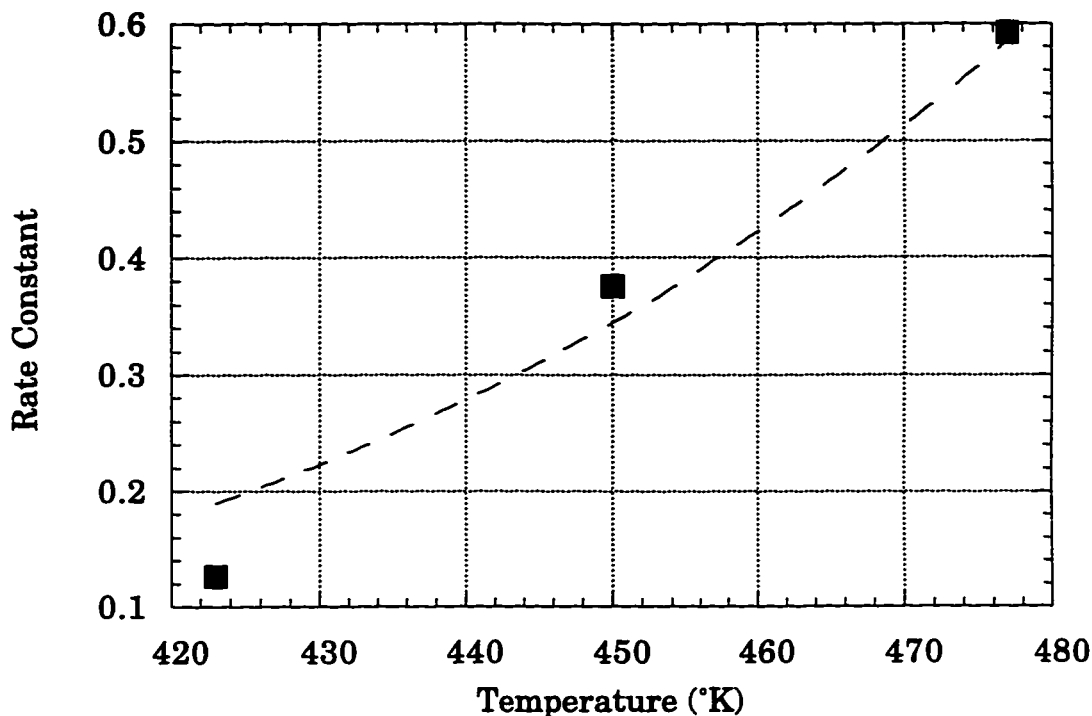


Figure 4.3 Temperature dependence for the reaction rate of thermo-oxidative degradation parallel to the fibers in IM7/K3B

The diffusion coefficients for IM7/5260 show no trends. Because diffusivity in the degraded region is very high relative to the reaction rate, the parabolic term in equation (4-21) is almost zero. The slight fluctuations in data are responsible for the wide variation in  $D'$ . Degradation growth for this material is more appropriately modeled with a simple linear regression.

The diffusion through K3B is slower than the reaction rate, and dominates the degradation growth at longer aging times. The K3B material does not break apart in the manner of the thermoset 5260, and oxygen passes through the matrix at a much slower rate. The diffusion coefficients do not follow Arrhenius behavior. Diffusion is slowest at 204°C.

## 4.2 Finite element model

The equations developed in the previous section are sufficient for analysis of the one-dimensional degradation in the mode II fracture toughness specimens. For the analysis of degradation growth in CAI specimens and other complex geometries, a more general tool is required. Finite element modeling provides a versatile method of analyzing complex geometries, and so a finite element formulation of the diffusion/reaction process is presented here.

### 4.2.1 Governing equations

The diffusion of a gas through a solid with reaction is a well known problem. Recently, the oxygen diffusion in a polymeric material has been modeled in one-dimension [44, 45]. However, the models do not include any distinction between the degraded region and the unreacted material. Oxygen is allowed to diffuse homogeneously through the material. Clearly, the properties of the degraded and unreacted regions are not the same for the materials in this study. Therefore, a numerical model incorporating reaction kinetics and heterogeneous diffusivity was needed. Also, the anisotropic behavior of composite materials must be included in the equations. The following pages show the formulation for a heterogeneous model with anisotropic diffusion/reaction.

The diffusion of oxygen into a composite and the reaction with the polymer matrix proceeds as follows. The oxygen in the air dissolves onto the surface, giving the surface a concentration of  $C_0$ . This oxygen then diffuses through the degraded region. Within the degraded region, a small amount of reaction between the oxygen and polymer will continue until the reaction is complete. At the edge of the degraded region, most of the diffused oxygen will be absorbed by the unreacted polymer material. Diffusion past this point will not occur until the reaction has proceeded sufficiently to change the chemical composition of the polymer.

An analogous problem has been studied for decades in the geological sciences. This problem is the flow of water through unsaturated soil [46-48]. A reservoir of water exists at the edge of the region of interest, just as a reservoir of oxygen exists at the edge of the composite material. As water seeps into the soil, a saturated region develops behind a moving boundary. Water flows through the saturated soil relatively easily. This region is equivalent to the degraded region in the polymeric composite. At the boundary, unsaturated soil absorbs the water, which effectively stops the flow of water past this boundary. In the composite, unreacted polymer absorbs oxygen, which effectively stops diffusion past the boundary.

The flow at the boundary is governed by the capillary pressure. Capillary pressure is a measure of the attraction between the soil and water. It is defined as the pressure change due to the water being absorbed by the soil, and is always negative. An analogous term in the oxidation process would measure the attraction, or reactivity, between oxygen and polymer. This term will be designated the reaction pressure.

The reaction pressure,  $p_r$ , governs the flow of oxygen at the boundary of the degraded region. This term is governed by the reaction between oxygen and polymer. The flux,  $q$ , of the oxygen concentration is related to the reaction pressure by the diffusivity,  $D$ .

$$q = -D \nabla p_r \quad (4-23)$$

The equilibrium equation is found by evaluating the differential element shown in Figure 4.4. The change in concentration,  $C$ , within the element is equal to the flow through the boundaries.

$$dC \, dx \, dy = \left( -\frac{\partial q_x}{\partial x} \, dx \, dy - \frac{\partial q_y}{\partial y} \, dx \, dy \right) dt \quad (4-24)$$

which is equivalent to

$$\frac{\partial C}{\partial t} = -\frac{\partial q_x}{\partial x} - \frac{\partial q_y}{\partial y} \quad (4-25)$$

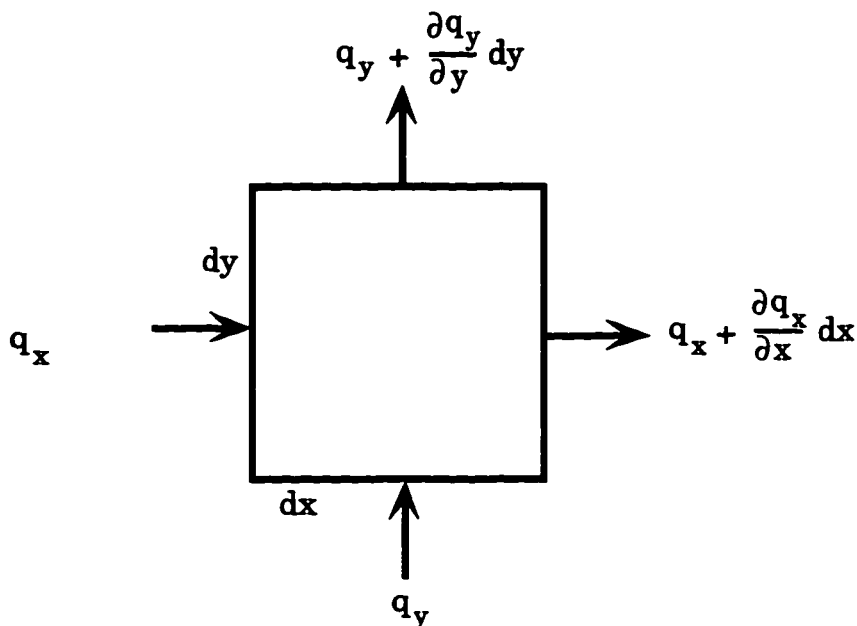


Figure 4.4 Differential element within the material

Substituting (4-23) into (4-25) yields

$$\frac{\partial C}{\partial t} = \frac{\partial}{\partial x} \left( D_x \frac{\partial p_r}{\partial x} \right) + \frac{\partial}{\partial y} \left( D_y \frac{\partial p_r}{\partial y} \right) \quad (4-26)$$

The concentration is normalized to saturation,  $S$ , by dividing through equation (4-26) with the maximum concentration of oxygen within the reacted polymer. The diffusivity constants absorb this term. In this formulation, the diffusivity terms are constant and can be pulled out of the derivative.

$$\frac{\partial S}{\partial t} = D'_x \frac{\partial^2 p_r}{\partial x^2} + D'_y \frac{\partial^2 p_r}{\partial y^2} \quad (4-27)$$

The reaction pressure is a function of the saturation. Parameters  $\alpha$  and  $n$  are found experimentally such that saturation follows the equation

$$S = \frac{1}{1 + \alpha(-p_r)^n} \quad (4-28)$$

With equation (4-28), equation (4-27) can be transformed into

$$\frac{dS}{dp_r} \frac{\partial p_r}{\partial t} = D'_x \frac{\partial^2 p_r}{\partial x^2} + D'_y \frac{\partial^2 p_r}{\partial y^2} \quad (4-29)$$

The diffusivity of the material is a function of the saturation. The degraded layer is much more diffuse than the unaged material. As saturation increases during the aging process, diffusivity increases. The relation between diffusion and saturation is chosen simply as

$$D = D_0 S^\lambda \quad (4-30)$$

When reaction pressure is near zero, the left hand side of equation (4-29) drops to zero and the equation is in a steady state. This is the case in the degraded region where oxygen flows freely due to the high diffusivity. In the undegraded region, the right hand side of equation (4-29) is near zero. The time rate of change is therefore near zero, indicating little change for even long aging times. The shape of the moving front at the boundary is determined by the parameters in equations (4-28) and (4-30).

Since  $S$  is defined explicitly as a function of  $p_r$  at each point in the material, equation (4-29) takes the form of a nonlinear diffusion equation. This equation was solved using finite element methods.

#### 4.2.2 Finite element formulation

The finite element problem was solved using MacFred [49], a program written by Professor K. A. Holsapple at the University of Washington. This program provided the user's interface and solution routines necessary

to solve the problem. A subroutine was added to this program to perform the element matrix calculations particular to this problem.

The Galerkin method was used to formulate the element matrices. An explanation of the general Galerkin method for linear problems is given in several textbooks [50-51]. Only the formulation of the element matrices for the nonlinear equation (4-29) is given here.

The weak formulation of (4-29) is

$$\int_{\Omega} v \left[ \frac{\partial}{\partial x} \left( D \frac{\partial p_r}{\partial x} \right) + \frac{\partial}{\partial y} \left( D \frac{\partial p_r}{\partial y} \right) - \frac{\partial S}{\partial p_r} v \frac{\partial p_r}{\partial t} \right] dA = 0 \quad (4-31)$$

with  $v$  as the set of trial functions and  $\Omega$  the domain. Equation (4-31) is integrated by parts to remove the second derivative, giving

$$\int_{\Omega} \left[ \frac{\partial v}{\partial x} D \frac{\partial p_r}{\partial x} + \frac{\partial v}{\partial y} D \frac{\partial p_r}{\partial y} + \frac{\partial S}{\partial p_r} v \frac{\partial p_r}{\partial t} \right] dA - v D \bar{n} \cdot \nabla p_r \Big|_{\Gamma} = 0 \quad (4-32)$$

Since the trial functions are defined as zero on the boundary  $\Gamma_1$  and the slope of the reaction pressure is zero on the remaining boundary, the boundary term drops out.

The basis functions define the reaction pressure by

$$p_r = \sum_{i=1}^N N_i p_i \quad (4-33)$$

Substituting (4-33) into (4-32), the equation becomes

$$\int_{\Omega} \left[ \frac{\partial N_k}{\partial x} D \frac{\partial N_i}{\partial x} p_i + \frac{\partial N_k}{\partial y} D \frac{\partial N_i}{\partial y} p_i + \frac{\partial S}{\partial p_r} N_k N_i \dot{p}_i \right] dA = 0 \quad (4-34)$$

This can be rewritten in the form

$$C_{ki}\dot{p}_i + K_{ki}p_i = 0 \quad (4-35)$$

$$K_{ki} = \int_{\Omega} \left[ \frac{\partial N_k}{\partial x} D_x(p_i) \frac{\partial N_i}{\partial x} + \frac{\partial N_k}{\partial y} D_y(p_i) \frac{\partial N_i}{\partial y} \right] dA \quad (4-36)$$

$$C_{ki} = \int_{\Omega} \left[ \frac{\partial S}{\partial p_r}(p_i) N_k N_i \right] dA \quad (4-37)$$

The integrals are evaluated using Gaussian integration. For each element, the integral is equal to the evaluation of the function at specific points within the integral, multiplied by a weighting function. For simple linear terms, the integrals can be found by

$$K_{ki}p_i = \sum_m w_m \left( D_x \frac{\partial N_k}{\partial x} \frac{\partial N_i}{\partial x} p_i \Big|_{X_m} + D_y \frac{\partial N_k}{\partial y} \frac{\partial N_i}{\partial y} p_i \Big|_{X_m} \right) \quad (4-38)$$

$$C_{ki}\dot{p}_i = \sum_m w_m \frac{\partial S}{\partial p_r} N_k N_i \Big|_{X_m} \quad (4-39)$$

where the  $m$  Gaussian points are evaluated using the coordinates  $X_m(x_m, y_m)$ , and the  $w$  terms are the weights for each Gaussian point. Adding in the nonlinear terms, the equations become

$$K_{ki}p_i = \sum_m w_m \sum_j \left( N_j D_x(p_i) \frac{\partial N_k}{\partial x} \frac{\partial N_i}{\partial x} p_i \Big|_{X_m} + N_j D_y(p_i) \frac{\partial N_k}{\partial y} \frac{\partial N_i}{\partial y} p_i \Big|_{X_m} \right) \quad (4-40)$$

$$C_{ki}\dot{p}_i = \sum_m w_m \sum_j N_j \frac{\partial S}{\partial p_r}(p_i) N_k N_i \Big|_{X_m} \quad (4-41)$$

With equations (4-40) and (4-41), the time derivative in equation (4-35) can be solved using the theta method. This method treats the time dependency as a separate function, enabling the problem to be solved using Gaussian integration. The equation for reaction pressure is written as

$$\mathbf{p}_r(\mathbf{x}, y, t) = \mathbf{p}(\mathbf{x}, y) \mathbf{T}(t) \quad (4-42)$$

Basis functions are defined for the time function, just as for the spatial basis functions used in the Galerkin method. For a single time element,

$$T_n = 1 - \frac{t}{\Delta t}; \quad T_{n+1} = \frac{t}{\Delta t} \quad (4-43)$$

The weak formulation of (4.35) over a single time element becomes

$$\int_{t_n}^{t_{n+1}} w_j [C \dot{\mathbf{p}}_r + \mathbf{K} \mathbf{p}_r] dt = 0 \quad (4-44)$$

Using equation (4-42), the formulation is

$$\int_{t_n}^{t_{n+1}} w_j [C(\mathbf{p}_n \dot{T}_n + \mathbf{p}_{n+1} \dot{T}_{n+1}) + \mathbf{K}(\mathbf{p}_n T_n + \mathbf{p}_{n+1} T_{n+1})] dt = 0 \quad (4-45)$$

The theta term is defined by

$$\theta = \frac{\int w_j t dt}{\int w_j dt} \quad (4-46)$$

Using the definition of theta, (4-46), and the definition of the time basis functions, (4-43), equation (4-45) can be rewritten as

$$\left[ \frac{1}{\Delta t} C + \theta \mathbf{K} \right] \mathbf{p}_{n+1} + \left[ -\frac{1}{\Delta t} C + (1 - \theta) \mathbf{K} \right] \mathbf{p}_n = 0 \quad (4-47)$$

Equation (4-47) is the general equation for the theta method.

The nonlinear element matrices in (4-40) and (4-41) were used with the theta method given in (4-47) to solve the diffusion/reaction problem. FORTRAN subroutines were written to solve the finite element equations in conjunction with the FRED program. The listings for these subroutines are given in Appendix C.

### 4.2.3 Modeling results

The two composite materials studied had differing diffusion/reaction characteristics. Diffusion through the degraded 5260 was fast relative to the reaction process. Oxygen diffuses quickly through the material until reaching the moving boundary between degraded and undegraded polymer. Therefore, oxygen levels are near saturation throughout the degraded region and a steep gradient of oxygen concentration develops at the boundary. In contrast, oxygen diffuses slowly through K3B compared to the reaction process. Oxygen concentration decreases with increasing distance from the surface. The profiles of the oxygen concentration versus distance from the surface for these two materials, as calculated by the finite element routine, are shown in Figure 4.5.

Figures 4.6 and 4.7 show the results for degradation growth parallel and transverse to the fibers in unidirectional IM7/5260 aged at 204°C. The numerical model captures the linear behavior well. The parabolic behavior of degradation growth in K3B is also captured by the model, as shown in Figures 4.8 and 4.9. The difference between the two materials is seen in the input parameters shown in Table 4.2. 5260 has faster diffusion and the K3B has a higher reaction rate. The difference in growth between the two directions is governed by the diffusion rate. Since other parameters are determined by the chemical reaction between the polymer matrix and oxygen, only the diffusion was allowed to change for each material.

Table 4.2 FEM parameters for 1-D degradation growth

	5260 Parallel	5260 Transverse	K3B Parallel	K3B Transverse
Diffusivity	7.1	2.2	1.9	0.9
lamda	2.4	2.4	2.5	2.5
alpha	0.01	0.01	0.05	0.05
n	4.8	4.8	1.5	1.5

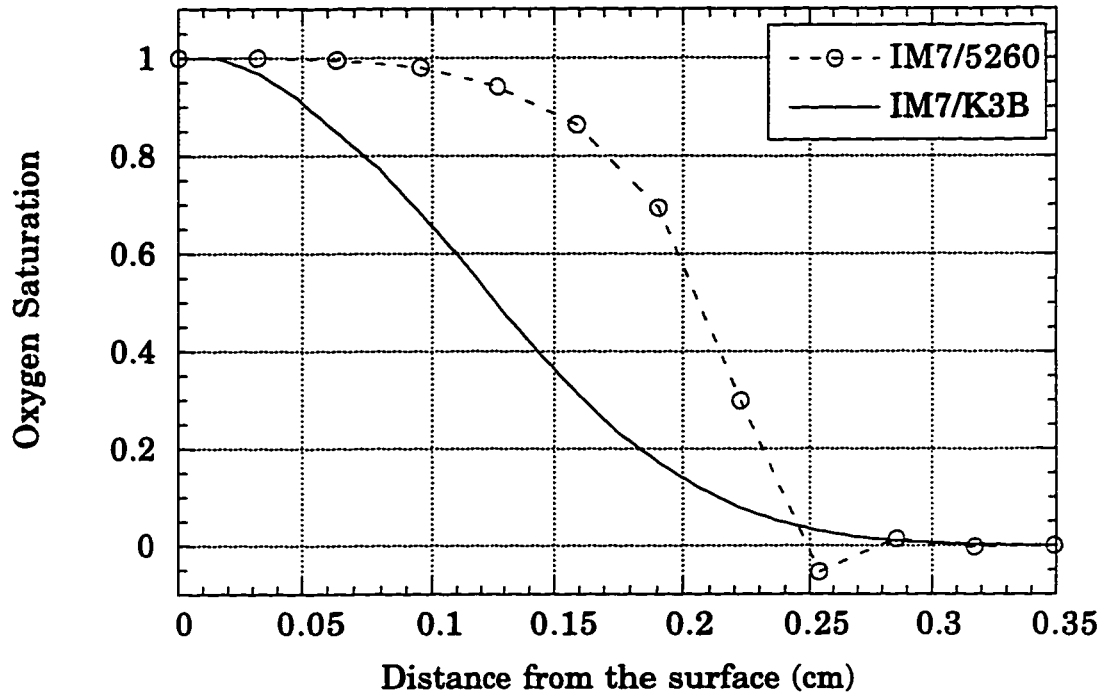


Figure 4.5 Profile of diffused oxygen saturation near the surface

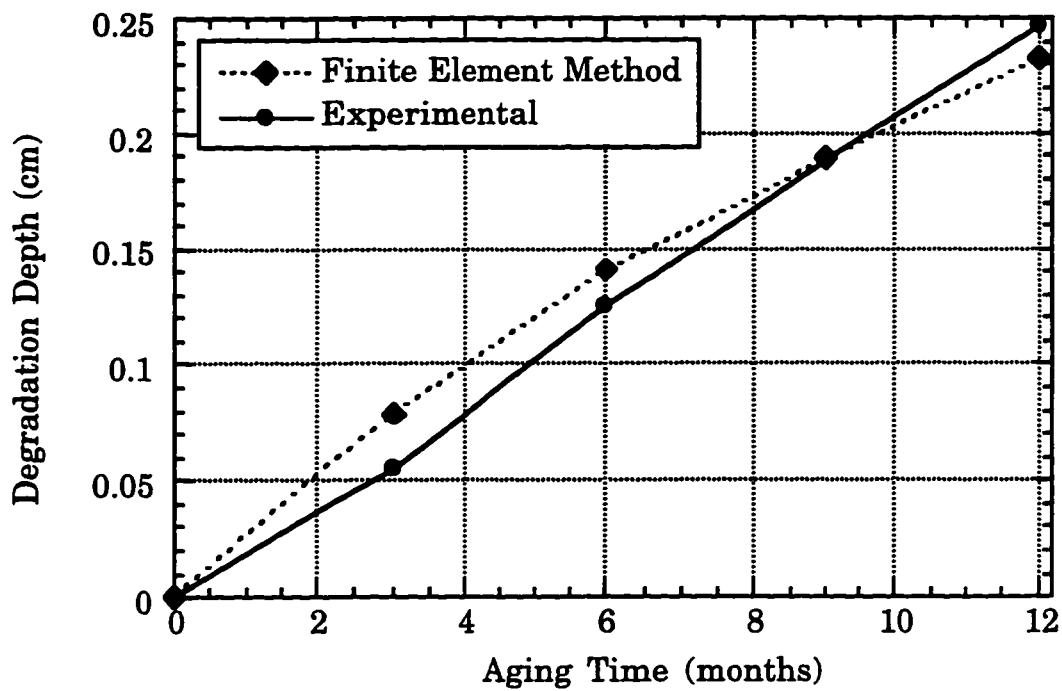


Figure 4.6 Degradation along the fibers in IM7/5260 aged at 204°C

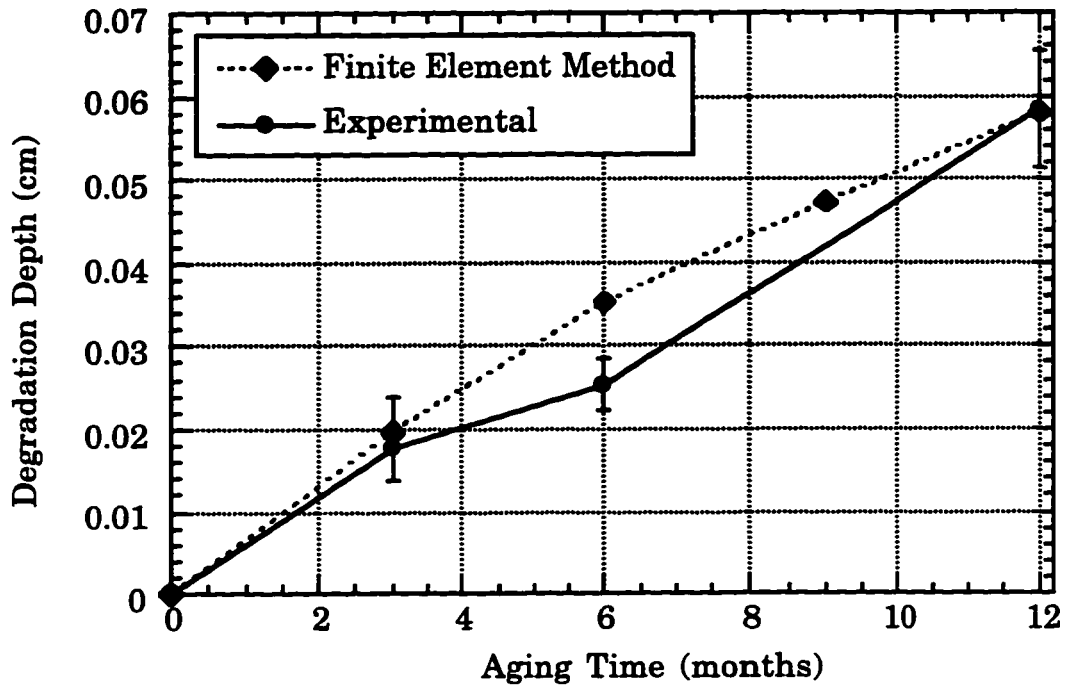


Figure 4.7 Degradation transverse to fibers in IM7/5260 aged at 204°C

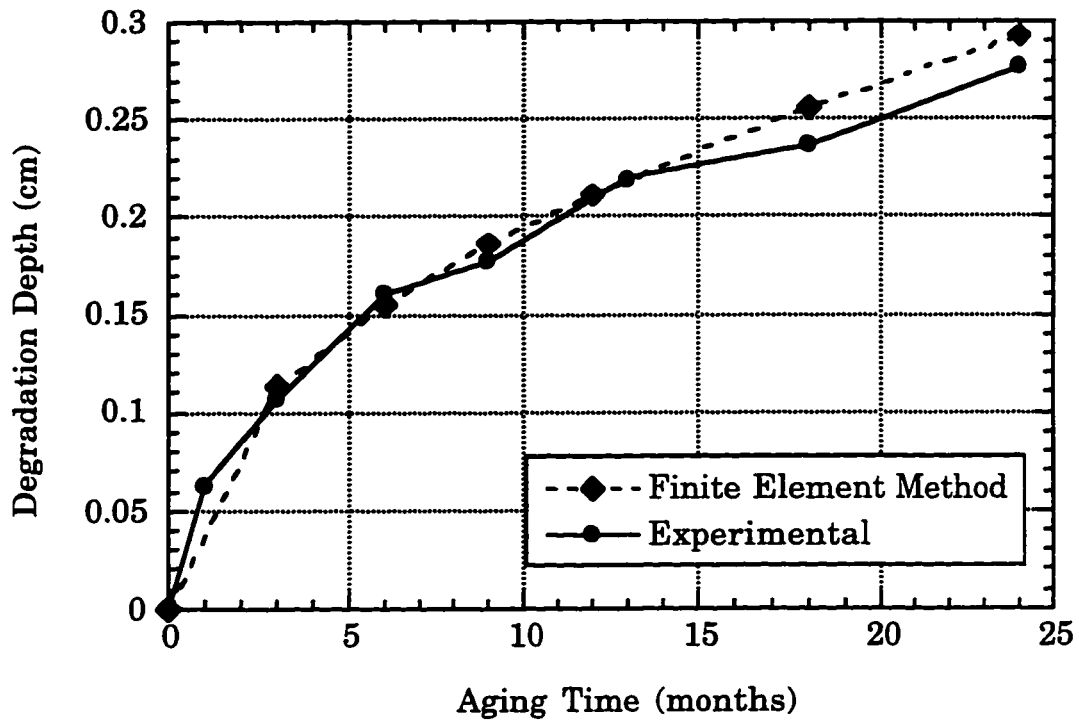


Figure 4.8 Degradation along the fibers in IM7/K3B aged at 204°C

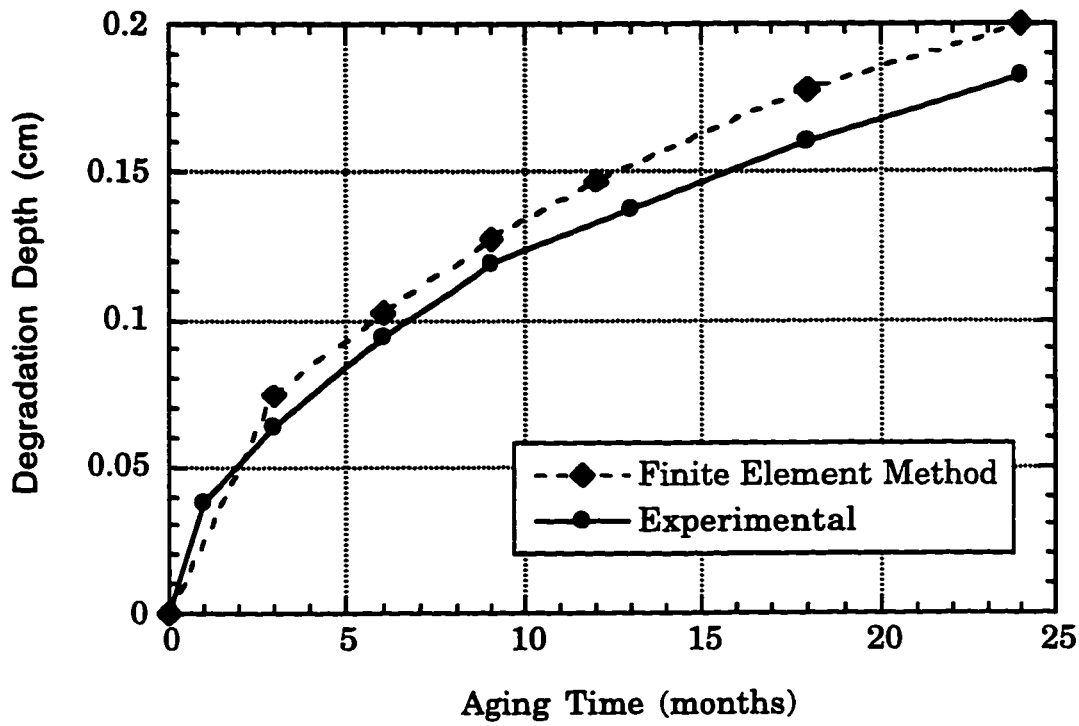


Figure 4.9 Degradation transverse to fibers in IM7/K3B aged at 204°C

As discussed in Section 3.3, open hole specimens were aged to provide experimental data for two dimensional degradation growth. A specimen was aged for 6 months at 204°C. A wedge was forced between plies and then surface layers were peeled away to reveal the surface shown in Figure 4.10. The dark discoloration around the open hole is caused by thermo-oxidative degradation.

The finite element program was used to model the open hole case for unidirectional IM7/5260 using the parameters determined from the one dimensional analysis. The boundary for degradation after 6 months of aging at 204°C is depicted by the dashed line in Figure 4.11. The edge of the open hole is shown by the solid line. The degraded region is thickest in the direction parallel to the fibers, which lie across the page as indicated in the figure. The actual degradation of the open hole specimen verifies the ability of the finite element model to predict two dimensional degradation.

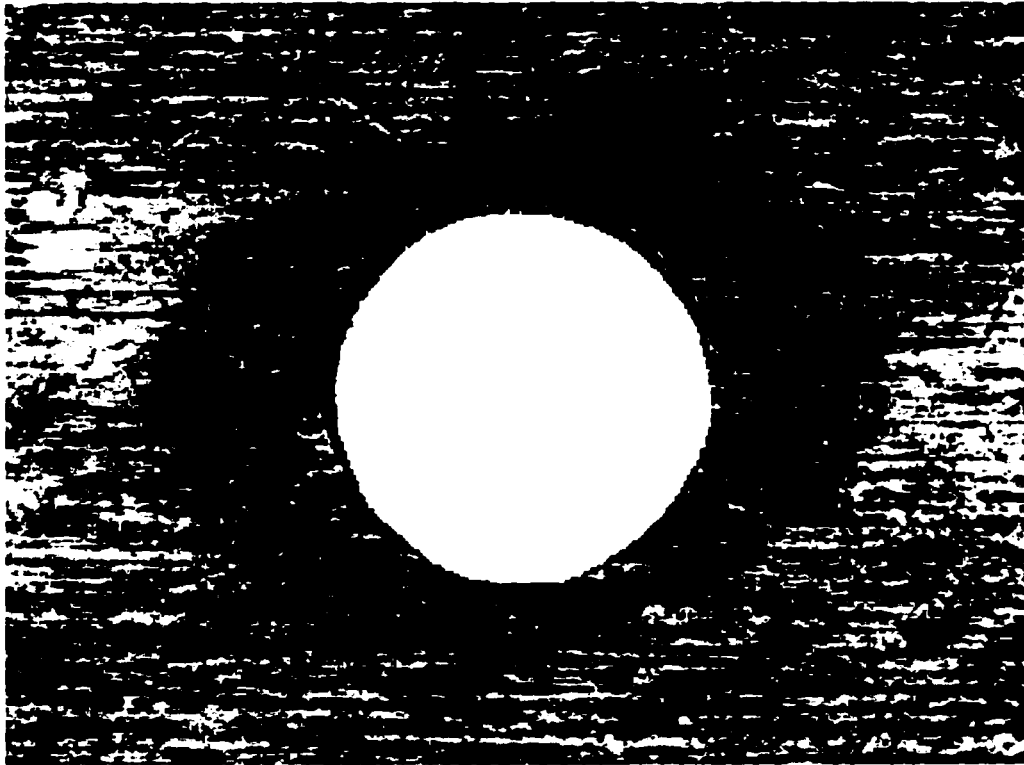


Figure 4.10 Interior ply of an aged open hole specimen

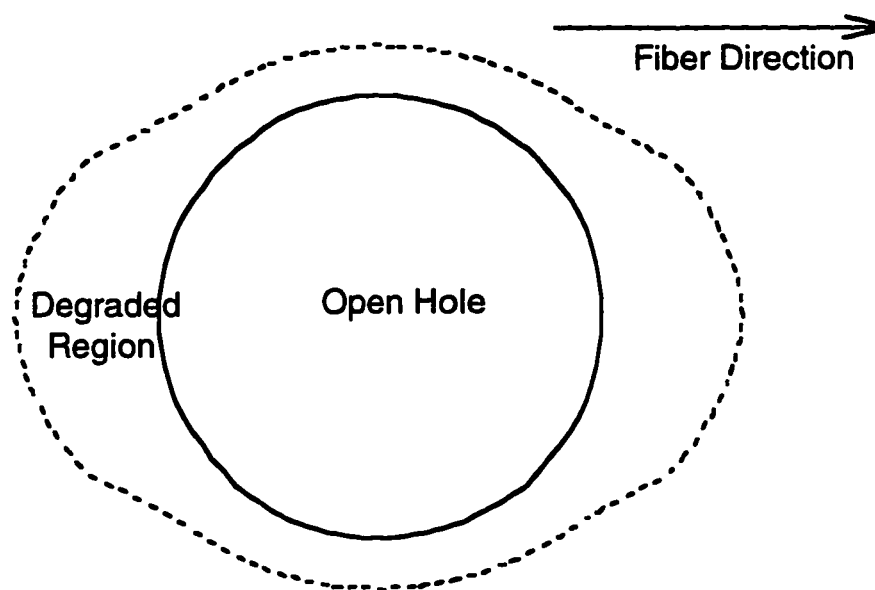


Figure 4.11 Degradation boundary around an open hole from FEM

## Chapter 5

### **COMPRESSION AFTER IMPACT STRENGTH THEORIES**

The delamination damage incurred by an object striking an aircraft structure at low velocity is a significant problem with using composite materials which does not occur when using conventional metal materials. In metals, the kinetic energy transferred to the structure by an impacting object is absorbed primarily through plastic deformation. If the energy absorbed is small, the deformation will be small and have little effect on the strength of the structure. If the energy is large, the deformation is large and can easily be found by a visual inspection. The structure can then be repaired, restoring its original strength.

In composite materials, the energy absorption mechanisms are more complex. The dominant mechanisms for absorbing impact energy include fiber failure, the fracturing of fibers, delamination, which is debonding between individual plies, and matrix cracking. The extent of fiber failure is generally restricted to an area equal in size to the area of visible surface damage and is similar to the plastic deformation of metals. Small fiber failures can usually be tolerated and severe fiber failures can easily be found and repaired.

The delamination between plies is of greater concern to the designers using composite materials. Surface damage that appears quite small can correspond to a large delamination area. Under compressive loading, these large delamination areas cause failure of the composite panel because the delamination zone undergoes a local buckling that significantly reduces local laminate stiffness. Strain concentrations develop around the buckled sublaminates and failure strength of the laminate decreases. Therefore, it is of great importance to characterize and model the extent of damage within the specimen when studying Compression After Impact (CAI) strength.

The response of composite structures to impact has been a subject of interest for over 20 years in the aerospace industry. In service, an aircraft structure is subjected to events which greatly reduce the compressive strength and durability of the damaged component. A standardized test for measuring this strength was released by NASA in 1983 [52]. The Boeing Company and ASTM followed with their own standards [53, 54] soon after. The release of these documents was surrounded by many studies addressing the issues involved in CAI strength.

## 5.1 Impact Damage

### 5.1.1 *Impact Modeling*

The force applied by a low velocity object striking a laminate and the response of the laminate to this impact can be calculated in a direct manner for composites [55-57] until the first failure. For the prediction of failure, the analysis of the stress field can be simplified by assuming quasi-static conditions [58-59]. This is because the inertial forces are small compared to the force of the impactor and can be neglected. Put another way, the velocity of the impactor is very small compared to the velocity of the shock waves and so spalling will not occur. The first failure of the composite is predicted by analyzing the strain field around the impact zone and using simple failure criteria [60].

Successive failure is much more difficult to predict. The stress field is altered by the growing damage, and each successive failure is affected by the preceding failures. A slight error in calculating the first failure leads to more errors during the damage process, resulting in a substantial error in the final damage area. The analytical predictions are useful for analysis of composite durability. However, the accuracy of experimental measurements is far better than any analytical prediction based on impact energy, specimen properties, or impact geometry. Only experimental data was used for evaluating the extent of damage within composite laminates in this study.

### *5.1.2 Damage Characterization*

The actual damage in an impacted composite is a complex combination of delaminations, matrix cracks, and broken fibers. Most studies performed on the damage state determine a relationship between the extent of damage and some parameter of the impact or specimen [61-68]. These studies lend insight into the impact process, qualitatively relating damage characteristics to impact or material variables. These studies do not lend themselves to residual strength modeling, since they cannot make quantitative predictions without experimental data.

The K-rule presented by Gosse and Mori is a good method for predicting the matrix delamination characteristics due to impact [62]. While it does not predict the quantitative damage area caused by an impact event, the K-rule provides a means of predicting the shape and form of delamination between plies of the laminate. A brief explanation of the methodology of the K-rule as applied to a quasi-isotropic layup follows.

Principal strains for an element of the laminate are determined from an analysis of the strain field caused by a surface impact. The element considered has a square cross section, with a height of one ply thickness, and runs radially out from the impact point parallel to the ply fiber direction. The strain field for the cross section of this element and the resulting principal strains are shown in Figure 5.1. Also shown in this figure is the crack which forms if the magnitude of the principal strains exceeds the material limit of the matrix. When cracks form in consecutive plies of the laminate, delamination propagates between these cracks. A delamination between elements in consecutive plies is shown in Figure 5.2. In this figure, the two elements shown run parallel to the fibers in their respective plies, and the impact point is at the intersection of the two elements. Many plies with such delaminations and cracks will link into a series of delaminations, forming a spiral staircase progression through the laminate. For a  $(45/0/-45/90)_{3s}$  laminate, the ply by ply delaminations and cracks are as shown in Figure 5.3. This type of damage was characteristic for all specimens impacted in this research work.

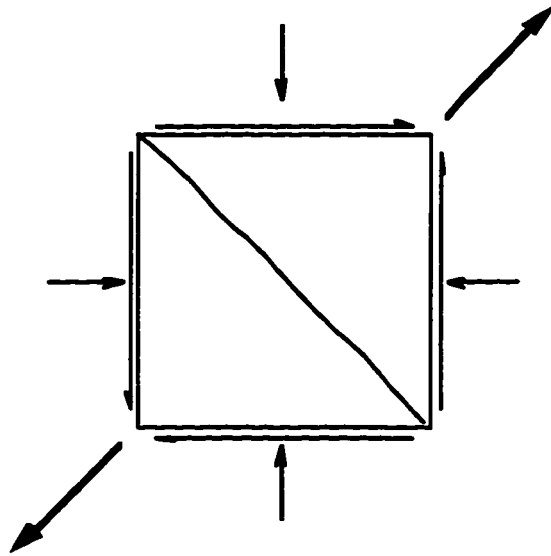


Figure 5.1 Strain fields, principal strains, and crack propagation for an element in the K-rule damage analysis [62]

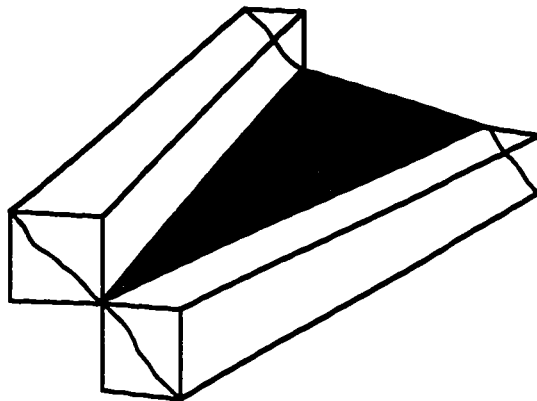
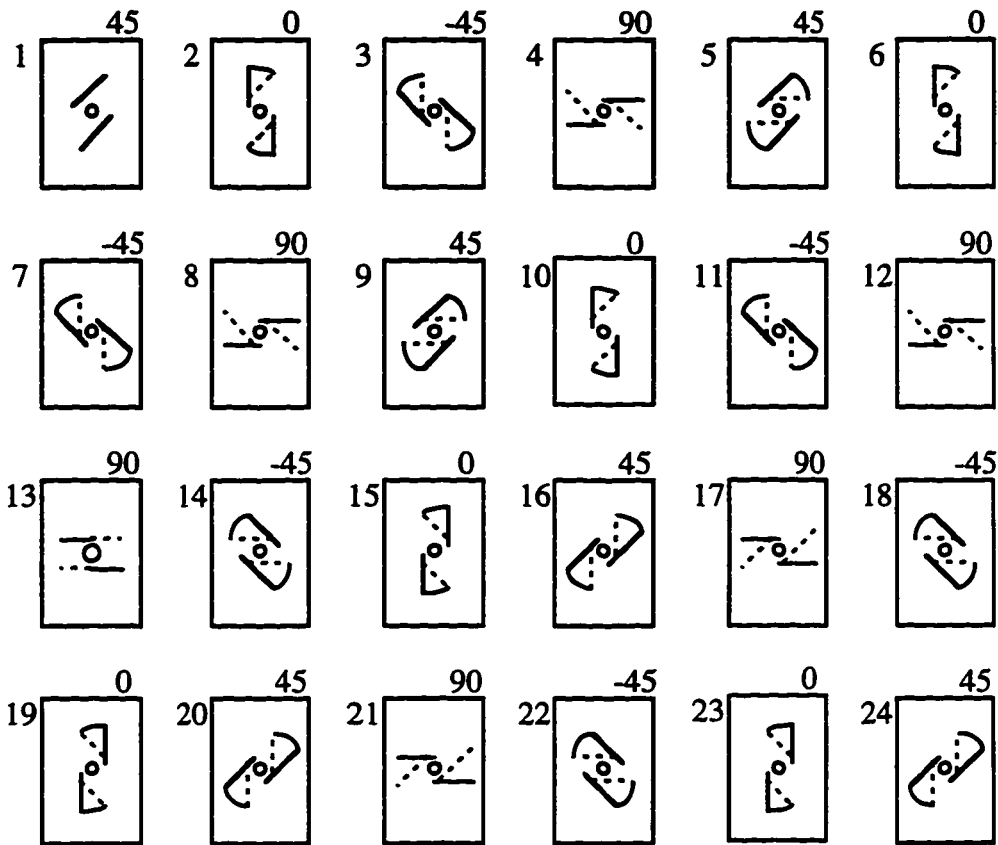


Figure 5.2 K-rule prediction of delamination region connecting two different ply elements with transverse cracks [62]



Delaminations shown exist between the present ply and the previous ply. Dashed lines represent cracks in the previous ply.

Figure 5.3 Delaminations between plies of a  $(45/0/-45/90)_{3s}$  laminate

Unfortunately, the complicated damage modeled by these studies does not lend itself well to analysis of the stress states during axial compression. In order to perform such an analysis, the damage in the laminate must be idealized. The most common method of idealizing the damage is to assume that impact causes a delamination to occur near the back surface of the specimen. Although the actual damage includes matrix cracking and fiber failure, in many cases the delaminated area dominates the failure of the specimen. This simplification greatly reduces the complexity of the problem, and therefore many researchers have looked at plates with elliptical delamination near the surface.

## 5.2 Sublaminare Stability

Early work was performed by Chai and Babcock [69] on the modeling of an elliptical delamination near the surface of a flat plate. The model assumes a thin, orthotropic sublaminare on a thick isotropic base, and uses an elastic stability Rayleigh-Ritz method to determine sublaminare buckling load and the subsequent stress field. Whitcomb and Shivakumar [70-72] performed a similar analysis, comparing the Rayleigh-Ritz solution with a finite element solution. Other work has followed, building on this early work and developing more refined methods of determining the strain field in this simple model [73-79]. There have also been many studies that further limited the model to the one dimensional case [80-83]. While no longer applicable to the CAI specimen, these reports are interesting because of the cases they were able to study. Multiple delaminations and buckling of the base laminate were investigated for through the width delaminations in these studies.

An alternate approach is to idealize the damage region as a soft inclusion. Guild, Hogg and Prichard conducted this type of study using finite element models to predict the residual strength of a panel [84]. The difficulty lies in determining the stiffness of the soft inclusion. For the referenced study, reduced stiffness values were backed out of the finite element program by using experimental data of the ultimate strength. Ilcewicz, Dost, and Coggeshall combined both methods, using sublaminare stability to predict the reduced stiffness, and then using finite elements to determine final strength [85].

Dost, Ilcewicz, and Gosse have used the damage state determined by the K-rule to predict CAI failure using a sublaminare stability approach [86]. Lin and Li further modified this model by accounting for the post buckling response of the sublaminare [87]. In the model, the spiral array of delaminations is idealized by a stack of circular sublaminates with a thickness of four plies. The idealized dimension of the delamination is determined from a circle with an area equivalent to the area of the actual damage.

The stiffness properties of the sublaminates are calculated as the average stiffness for all possible stacking sequences. This greatly reduces calculations without significantly effecting the accuracy of the solution. The stability of the sublaminates is predicted using a series solution, assuming a thin sublaminate on a thick base laminate. Since the sublaminates are unsymmetric, reduced bending stiffnesses were used.

At stress levels above the critical buckling load, the sublaminates are assumed to carry a constant load. As load increases, the sublaminates carry a progressively lower percentage of the total load. Therefore, the damaged region is modeled as a soft inclusion, whose modulus is a function of load. An illustration of the reduced modulus and the simulated damage zone are shown in Figure 5.4. The modulus is calculated as the buckling stress, divided by current strain. Strain of the sublaminate is determined by imposing strain compatibility at the boundary.

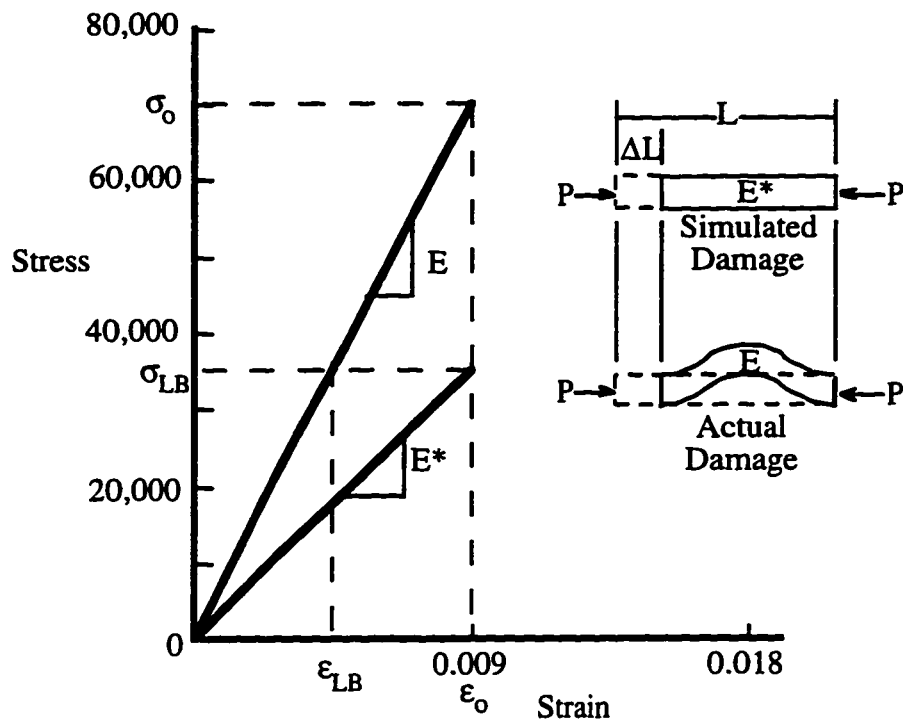


Figure 5.4 Reduced modulus calculation and simulated damage zone used in the sublaminate stability model [86]

The reduced modulus at failure is calculated as the buckling stress divided by the undamaged laminate failure strain. The reduced modulus is then used to calculate a modulus retention ratio,  $MRR = E^*/E$ . This is used to calculate the transverse and shear moduli of the sublaminates. Poisson ratio is assumed to remain the same. Using the calculated reduced moduli for the soft inclusion, a finite element model is used to calculate strain concentration near the damage state. With the stress redistribution calculated, a failure criterion is applied to predict failure strength of the damaged composite panel.

### 5.3 Failure Criteria

#### 5.3.1 *Delamination Growth*

Once the stresses and strains around the damage have been determined, a failure criterion must be chosen. For the sublaminates model, the most common failure criterion is delamination growth. Many of the studies mentioned previously use delamination growth as a fracture criterion and there are quite a few additional studies devoted to improving techniques for determining delamination growth [88-90]. When critical fracture energy is reached, the direction of delamination growth must be determined. The specimen fails when delamination growth becomes unstable.

#### 5.3.2 *Localized Strength Failure*

Mechanics of materials failure criteria have also been used to predict CAI strength, including maximum stress, maximum strain, von Mises, Tsai-Hill, and Tsai-Wu. Tan provides a good review of these failure criteria [91]. The stress fields are analyzed for the specimen, and then the appropriate criterion is used to pick first ply failure.

Failure can be further analyzed to predict the strength of undamaged composite laminates [92]. These models use constituent properties to predict failure in different fiber directions. In compression of quasi-

isotropic laminates, failure is determined by the  $0^\circ$  plies. During failure, the load bearing plies separate from surrounding plies and fail in shear. Known as kinking or brooming, this type of failure occurs when the top and bottom halves of the ply undergo opposite, out-of-plane displacement. Figure 5.5 shows the four surface plies of a quasi-isotropic specimen. The interior plies remain straight after failure, while the outer ply buckles. The load bearing  $0^\circ$  ply had failed in the center of the picture. Failure in these plies is determined by interlaminar shear strength of the matrix material since the ply does not fail until separation occurs between plies.

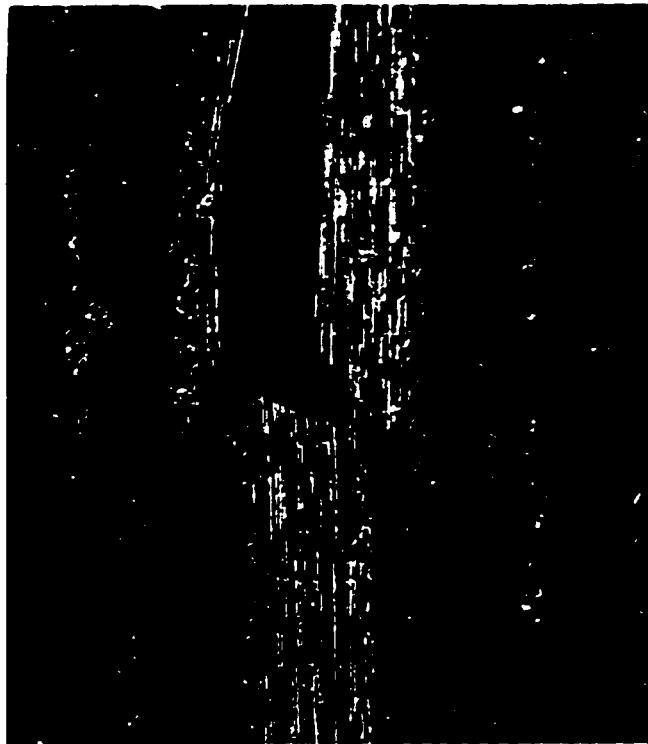


Figure 5.5 Edgewise view of compression failure in the  $0^\circ$  ply

## Chapter 6

### COMPRESSION AFTER IMPACT STRENGTH TESTING

#### 6.1 Failure strength

##### 6.1.1 *Experimental Procedure*

Test matrices were designed to produce data corresponding to the expected thermal environment of the HSCT fuselage. Aging temperatures of 1490°C and 177°C were chosen because these are the temperatures predicted in the composite structure at Mach 2.4. A 204°C aging temperature was studied to evaluate accelerated aging. Aging took place at sea level pressure, a more aggressive aging environment than the expected service environment of 20 km. The greater pressure accelerated the oxidation degradation.

Aging times for IM7/5260 were chosen using a graph of the change in glass transition temperature as a function of time and temperature for the composite material studied. A plot of  $T_g$  data and the resulting curve fits are shown in Figure 6.1. The times were selected so that the change in  $T_g$  would be the same between each data point, in the hopes that this would create an equivalent change in CAI strength properties.

Five aging times up to the maximum aging time were chosen for IM7/5260 to fully characterize the changes due to aging over time. Smaller intervals in aging time were used initially, in order to study the short term behavior more carefully. Longer time intervals were used for the last groups of specimens, since the aging process was expected to approach a steady state condition. Final aging times at each temperature were chosen according to the expected amount of degradation. That is, shorter aging times were used with higher aging temperatures. Longer aging times would not have provided useful data, because CAI strength of the specimen dropped below acceptable levels for engineering applications.

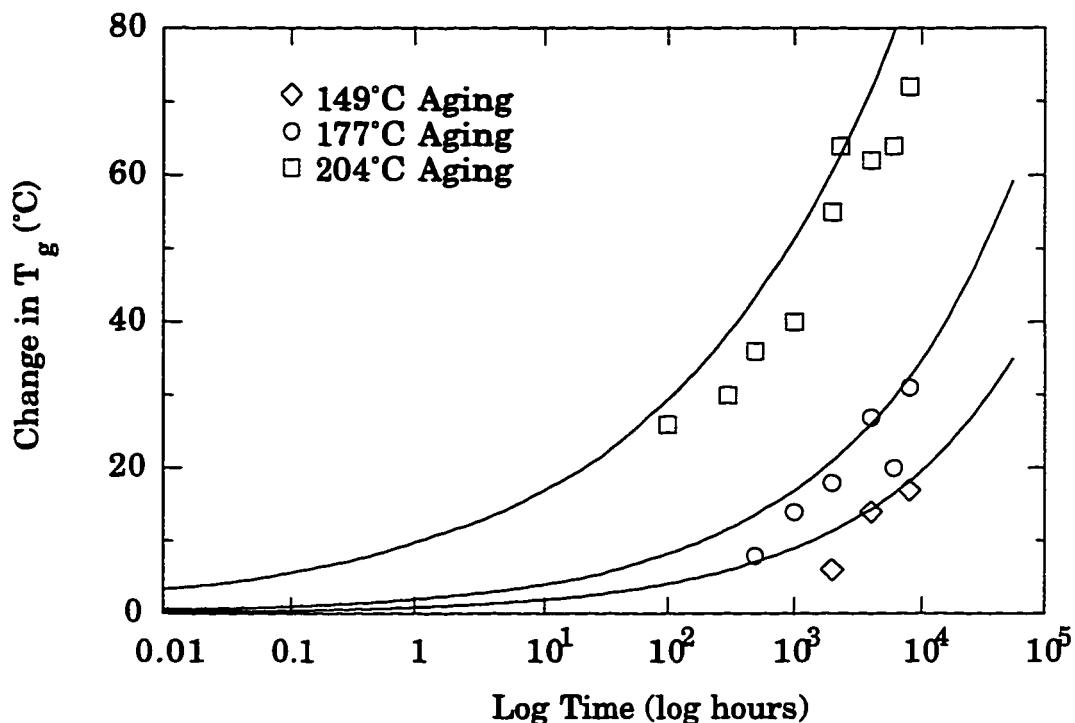


Figure 6.1  $\Delta T_g$  used to select aging times for IM7/5260

The maximum aging time for IM7/K3B was two years, approximately 17,500 hours. While less than one third of the lifetime of the HSCT, two years of aging was considered sufficient to draw meaningful conclusions about the long term aging characteristics of the polymeric material. Since the correspondence between  $\Delta T_g$  and CAI strength degradation proved poor in IM7/5260, a more uniform test matrix was selected for IM7/K3B. Each aging temperature had the same aging times. Eight aging times were chosen, with a several month interval between successive aging times. Smaller intervals were used initially to capture short term behavior. Longer time intervals were used at the end of the study since aging behavior became constant.

Three different impact energy levels were chosen so that the variation in aging effects due to damage size could be characterized. Impact energies of 11.3 J (33.1 J/cm), 22.6 J (66.2 J/cm), and 33.9 J (99.3 J/cm) were chosen, which correspond to damage states described as barely visible, visible, and severe, respectively. An impact energy level of 50.8 J (149 J/cm) was considered for IM7/K3B because of its higher impact resistance. However, this high energy impact resulted in near penetration of the laminate, and therefore was determined to be too large for this study. Barely visible damage states were characterized by an indentation depth of approximately 0.013 cm, no fiber breakout on the back surface, and internal damage consisting mostly of fiber breakage. Visible damage had a 0.046 cm indentation depth, fiber breakout, and some internal delaminations. Severe damage described a specimen with a 0.102 cm or deeper indentation, fiber breakout but no through penetration, and a substantial amount of delamination. A minimum of four replicates for each aging condition was used.

Two types of impact events were necessary for this study. CAI strength of a material depends on both the ability to tolerate existing damage and the ability to resist damage during an impact event. Test type a, impacting before aging, gives similar damage to all specimens at a given impact energy level, and so characterizes the effect of material property changes on damage tolerance. Test type b, aging before impact, characterizes the change in damage resistance for the specimen due to aging.

Once the parameters were set, specific testing points were selected to allow determination of the separate effects of time, temperature, and impact type. The test matrix for aged IM7/5260 CAI tests is shown in Table 6.1. Also, four unaged IM7/5260 specimens were tested for each impact energy level. The complete test matrix for IM7/K3B specimens is shown in Table 6.2.

Table 6.1 Test matrix for CAI testing of IM7/5260

Aging Temperature	Impact Energy	Aging Time (mon)							
		0.1	0.5	1.4	1.9	3.4	6.9	13.7	27.4
149°C	22.6 J	-	a, b	-	-	a, b	a, b	a	a
149°C	33.9 J	-	-	-	-	a, b	a, b	a	-
177°C	11.3 J	a	-	a	-	-	a	a	-
177°C	22.6 J	a, b	-	a, b	-	a	a, b	a	-
177°C	33.9 J	a	-	a, b	-	-	a	-	-
204°C	11.3 J	a	a	-	a	-	-	-	-
204°C	22.6 J	a, b	a, b	a	a	-	-	-	-

Note: a denotes 3 replicates impacted before aging  
b denotes 3 replicates aged before impact

Table 6.2 Test matrix for CAI testing of IM7/K3B

Aging Temperature	Impact Energy	Aging Time (months)							
		0	1	3	6	9	13	18	24
149°C	22.6 J	-	-	b	a	b	a	b	a
149°C	33.9 J	-	-	b	a	b	a	b	a
177°C	11.3 J	5	a	b	a	b	a	a, b	a
177°C	22.6 J	5	a	b	a	b	a	a, b	a
177°C	33.9 J	5	a	b	a	b	a	a, b	a
204°C	22.6 J	-	a	b	a	a, b	a	b	a
204°C	33.9 J	-	a	b	a	a, b	a	b	a

Note: a denotes 4 replicates impacted before aging  
b denotes 4 replicates aged before impact

The composite materials studied in this research had a quasi-isotropic (45/0/-45/90)<sub>3S</sub> layup. The laminate curing was performed by Boeing, and the material was shipped to the University of Washington in 60 cm by 56 cm panels. The panels had an average thickness of 0.35 cm. After visual inspection of the first batch, it was determined that some of the panels would be unsuitable for testing, as there were defects in the material from heavy scratches and impacts. All defective material was replaced. Later C-scans of the specimens confirmed that the composite material was initially free of defects.

The large panels were cut into twenty 10 cm by 15 cm samples with the 15 cm length parallel to the zero degree fiber direction. The material was cut using a rotary saw with a fluid cooled diamond cutting wheel rotating at 600 rpm. Each specimen dimension was checked to be within a tolerance of  $\pm 0.02$  cm.

Isothermal aging of all specimens was performed in three air-circulating ovens. Once the specimens were sealed inside, the ovens were programmed to reach aging temperature at a controlled rate of 2°C/min. The ovens were then set to continuously maintain the desired aging temperature. Temperature was maintained to within  $\pm 1^\circ$  of the set temperature at all points inside the oven. After aging for a set of specimens was completed, the ovens were allowed to cool and the specimens were removed. Cooling rates could not be set electronically, but were maintained at less than 2°C/min by controlling the amount of room temperature air flowing into the ovens. Time spent during the removal process was not counted toward the total aging time of the specimens.

Precision impacting of the CAI specimens was performed with a drop weight impactor. The procedure followed Boeing Specification 7260, using a 1.6 cm tup for the impactor. The specimens were held in an impact jig with a 7.6 cm by 12.7 cm rectangular opening. For each impact, graphs of load and impactor velocity as a function of time were recorded in order to fully characterize the impact event.

Ultrasonic pulse-echo C-scans were also performed on selected specimens to characterize the damage dimensions for each type of impact. The procedure consists of submerging the specimen in water, sending a sound wave into the specimen, and recording the returning sound waves. For undamaged specimens, two strong signals are received for the front and back of the specimen. Any discontinuity within the material, such as a crack or delamination, will also cause the signal to bounce back to the receiver. Scanning over the entire surface of the specimen produces images of the interior damage, from which damage dimensions are determined.

A loss of back signal C-scan was used to generate the digitized image of delaminations through the thickness of the composite specimen. The digitized image was then used to calculate the dimensions of the damaged region in the following manner. First, the border of the damage zone was defined, by manually drawing a black line around the edge of the damage region. The interior of this prescribed region was then erased, and the exterior of this region was painted solid black. A simple histogram of the image then gave the damage area. Width and height of the damage area were also calculated from this black and white image. The diameter of a perfect circle with the same area was used to idealize the delamination damage. An example of the C-scan image and delamination area for a single specimen are shown in Figures 6.2 and 6.3.

Time-of-flight of the ultrasound signal was also recorded for IM7/K3B specimens, which determined the depth location of delaminations. Figure 6.4 shows a typical C-scan image of a specimen with impact damage. The left portion of the figure shows an overhead view of the specimen, while the right portion shows the expanded cross section provided by the time-of-flight measurements. The impact side is on the left of the cross section. Delaminations occur on the back side of the specimen away from impact. Fiber damage occurs through the entire thickness of the laminate, with a diameter roughly equivalent to the diameter of the surface indentation.

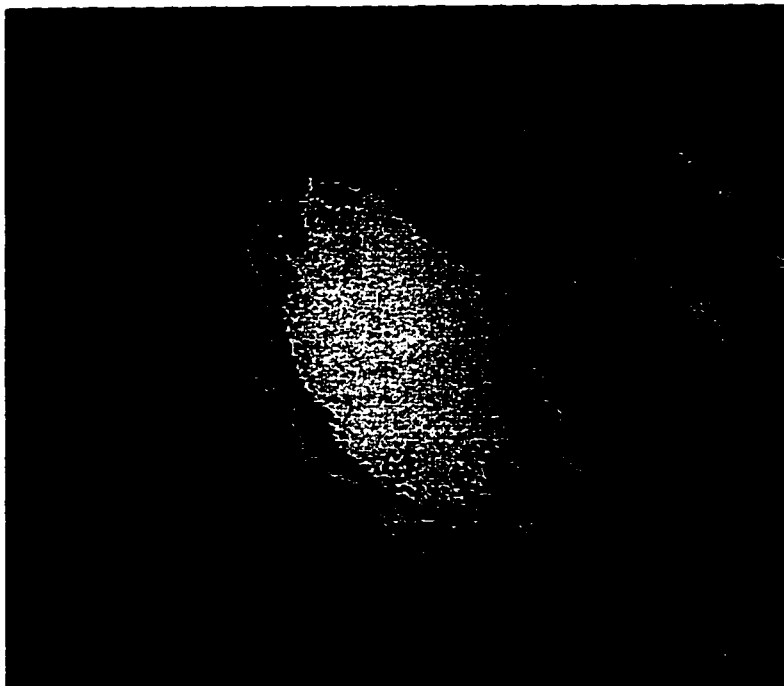


Figure 6.2 Image of loss of back signal for an impacted laminate



Figure 6.3 Damage area idealization from loss of back signal

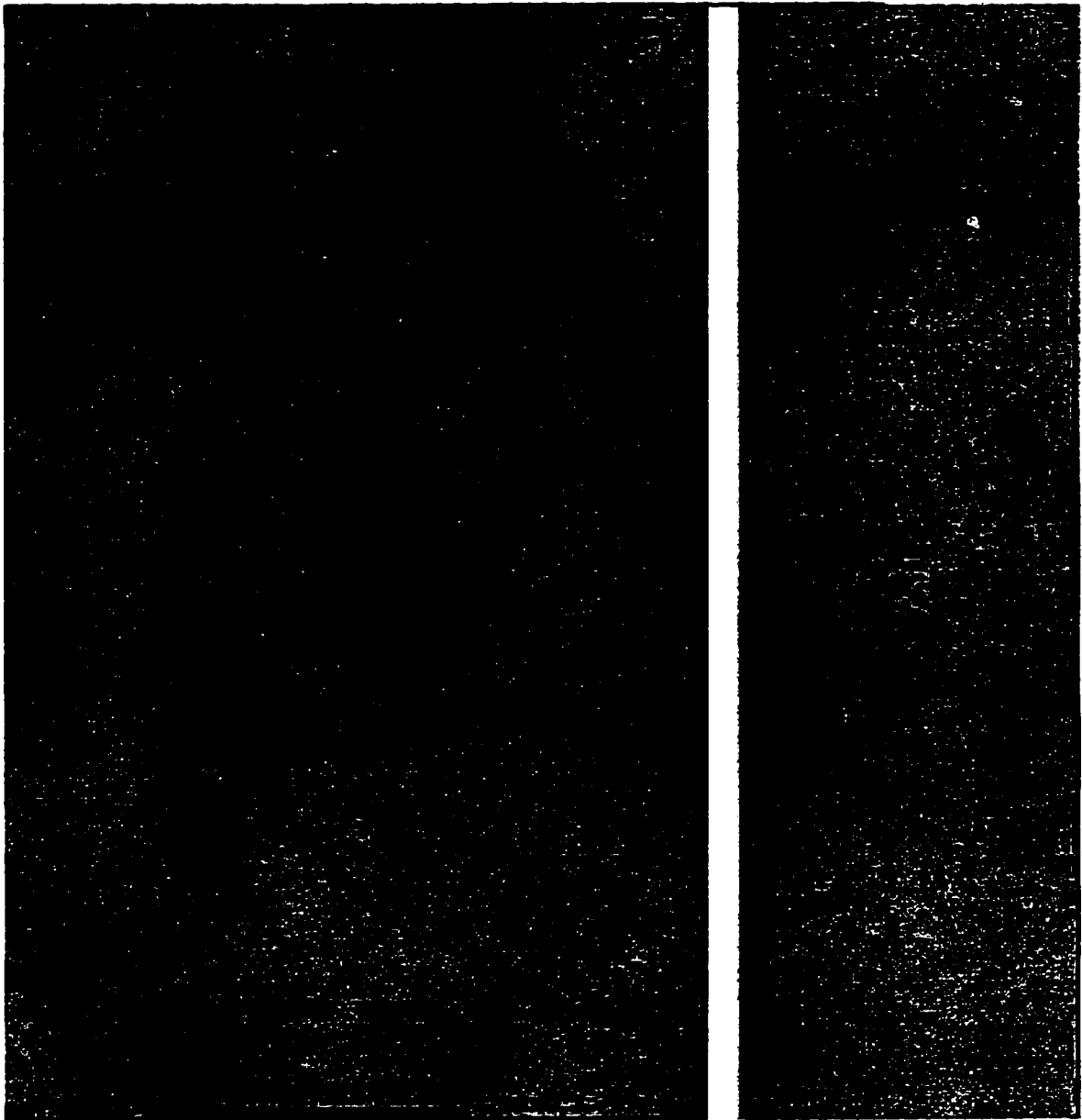


Figure 6.4 Internal signal from C-scan with time-of-flight

Because ultrasonic C-scans of specimens are costly and the total number of CAI tests conducted was quite large, not all specimens were scanned to determine the extent of internal damage. Only a representative number of specimens were scanned for each type of impact event. At least four specimens that were impacted before aging were C-scanned for each impact energy level and each material type. For specimens that were aged before impacting, at least two specimens were ultrasonically scanned for each aging time, aging temperature, and impact energy level.

After aging and impacting, strain gages were placed on each CAI specimen for measurement of 'far-field' strain. Back-to-back strain gages were located 3.75 cm down from the top of the specimen and 2.5 cm from the edge on each side. The specimen was then placed in a steel fixture, shown in Figure 6.5, to hold the specimen in simply supported boundary conditions on the edges and clamped boundary conditions on the ends. Bolts were tightened on the sides of the specimen until out-of-plane displacement was no longer possible at the edges, but in-plane slippage still occurred. The fixture was placed on the table of a 270 kN capacity testing machine. Each strain gage was connected to a quarter resistance bridge. Voltages from each resistance bridge were measured by a data acquisition board connected to a personal computer. A load voltage output from the testing machine was also read by the data acquisition board.

The top fixture and a half dome, which mated with a cusp on the loading arm, were placed on the top of the specimen. The loading arm was lowered slowly, and measurements of strain were taken. The application of the load was adjusted until the back to back strain gages indicated a uniform load application. The arm was then raised again to exactly zero. A data acquisition routine was started on the personal computer which calculated measurements of strain and stress twice per second. The loading arm was lowered at a rate of 0.06 cm/min. The test was run until the specimen failed, defined as a severe (greater than 50% of instantaneous value) drop in load. Failure was also accompanied by a loud noise and visible damage across the width of the specimen.

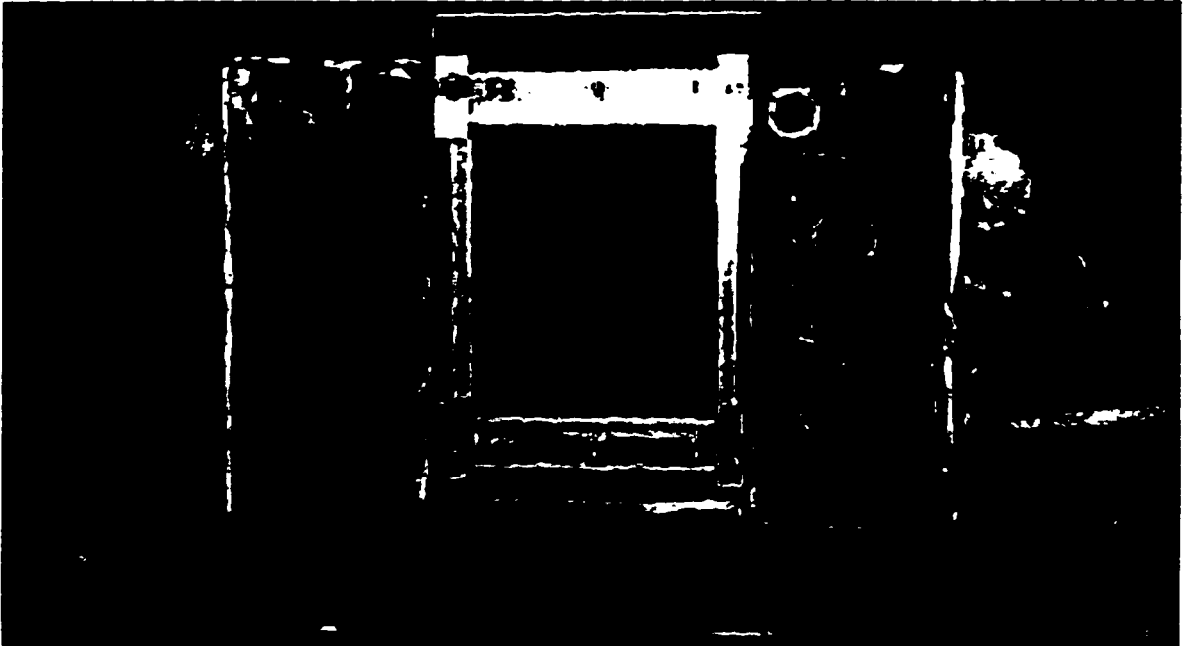


Figure 6.5 Test fixture for CAI specimens

The edges of the specimen were held straight throughout the test by the steel test fixture. Ideally, the specimen would have remained a flat plate during testing. However, the stiffness of the material was insufficient to resist bending at the high stress levels near failure. Therefore, out-of-plane displacements were measured for many specimens in order to determine bending strains due to curvature of the specimens. Shadow moiré was used to provide out-of-plane data for the entire surface of the specimen. A displacement dial gage was also used to verify the displacement calculations of the shadow moiré technique. This procedure is detailed further in Appendix A.

After testing, the maximum load reading from the dial gage of the testing machine was recorded. This maximum load was divided by the measured area of the specimen at the mid-plane to determine maximum stress. Digital values for stress and strain data were automatically stored by the computer. Data points recorded after specimen failure were deleted, and the maximum stress values were found. A typical plot is depicted in Figure 6.6. Modulus values for each specimen were calculated from the average of the stress-strain data from each strain gage. The nonlinear strain point, where buckling of the specimen causes noticeable differences between front and back strain, was determined for each specimen.

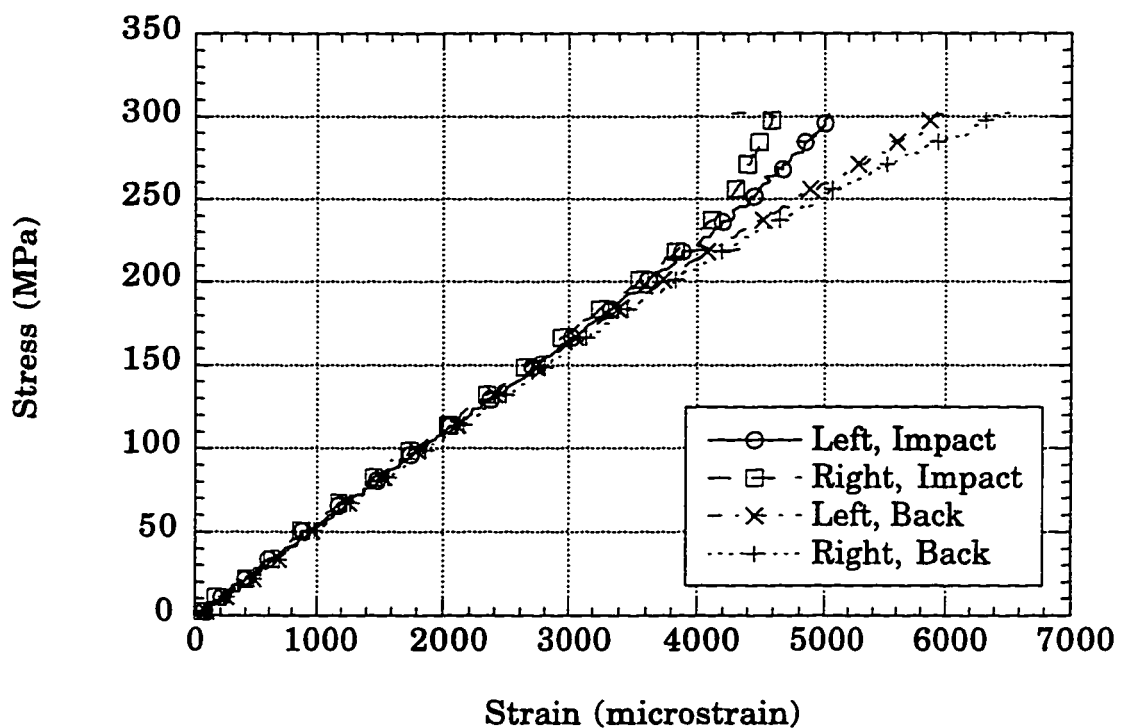


Figure 6.6 Typical CAI stress-strain data

### 6.1.2 Results from unaged specimens

The first task in the CAI program was to determine baseline compressive strength after impact for laminate specimens with zero aging. At least four specimens were tested for each of the three impact energy levels shown in the test matrix. The data are plotted in Figure 6.7. Also shown are results for compression tests of laminates with no impact damage. These tests were conducted to determine an upper limit on the strength of the laminate as well as testing the bending of the undamaged specimen. The one IM7/K3B specimen impacted at 50.8 J is also included.

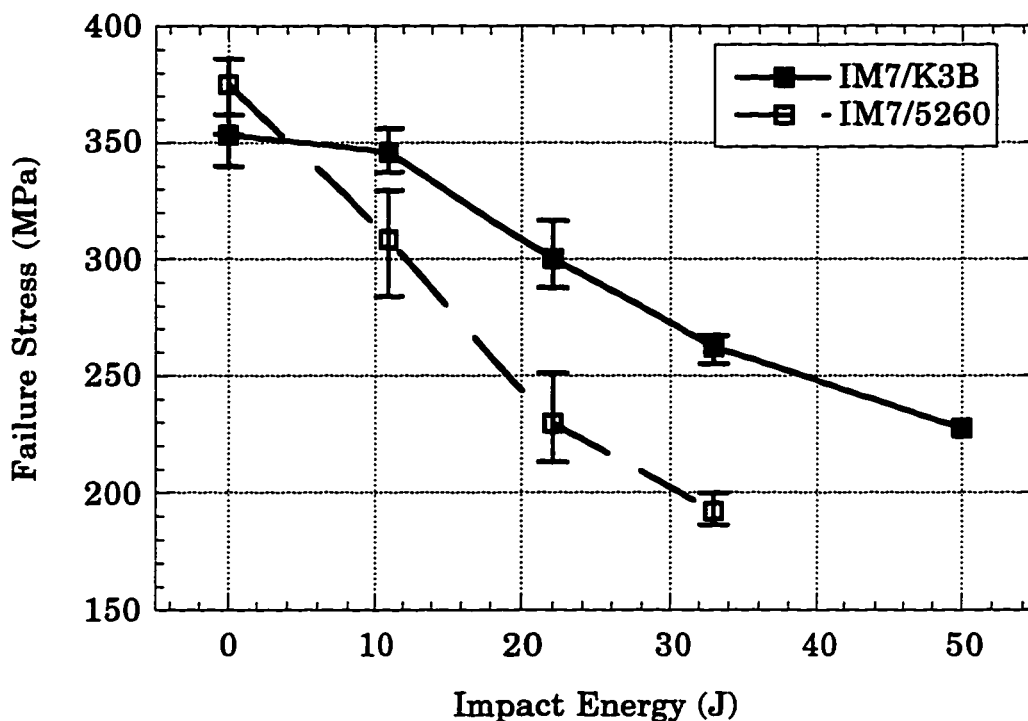


Figure 6.7 Failure stress for CAI specimens with zero aging

K3B has a substantially improved CAI strength over 5260 for equivalent impact energies. CAI strength of IM7/K3B is 12% higher than IM7/5260 for 11.3 J impacted specimens, and 36% greater in average strength at the 33.9 J impact energy level. 5260 does show a greater compression strength than K3B for undamaged laminate, which is most likely due to slightly higher compressive stiffness and strength. Note that the CAI strength for K3B specimens impacted at 11.3 J is virtually the same as the undamaged laminate compressive strength. The damage resulting from this type of impact is limited to fiber breakage with very little delamination, which has almost no influence on the compressive strength of the laminate. This point is important in the evaluation of CAI strength data for aged specimens.

The higher CAI strength of K3B material at equivalent impact energies is due to smaller damage areas. The average effective damage diameters, as determined by C-scan, of specimens impacted before aging are shown in Figure 6.8. The damage diameters determined by C-scan are significantly lower for K3B at all energy levels. This improved damage resistance is the reason for the greatly improved CAI strength of the K3B material. When CAI strength is plotted as a function of damage diameter, the two materials are roughly equivalent. This fact is shown in Figure 6.9

C-scans were also utilized to analyze the failure mechanism of CAI specimens. Specimens were loaded to near failure, but unloaded before failure occurred. During compression to 90% of predicted ultimate load, damage growth was audible in these specimens. The additional damage was quite noticeable in the C-scan images. The time-of-flight recordings showed that the additional damage occurred on the impacted surface of the specimen, as shown in Figure 6.10. Due to bending of the specimens, the back of the specimen had low strain and delaminations near the back surface did not grow during compression testing. Because of an initial curvature created by the impact event, the impact point was always on the inside curve of the specimen. This placed the impact side in a higher strain, and thus failure initiated on this side.

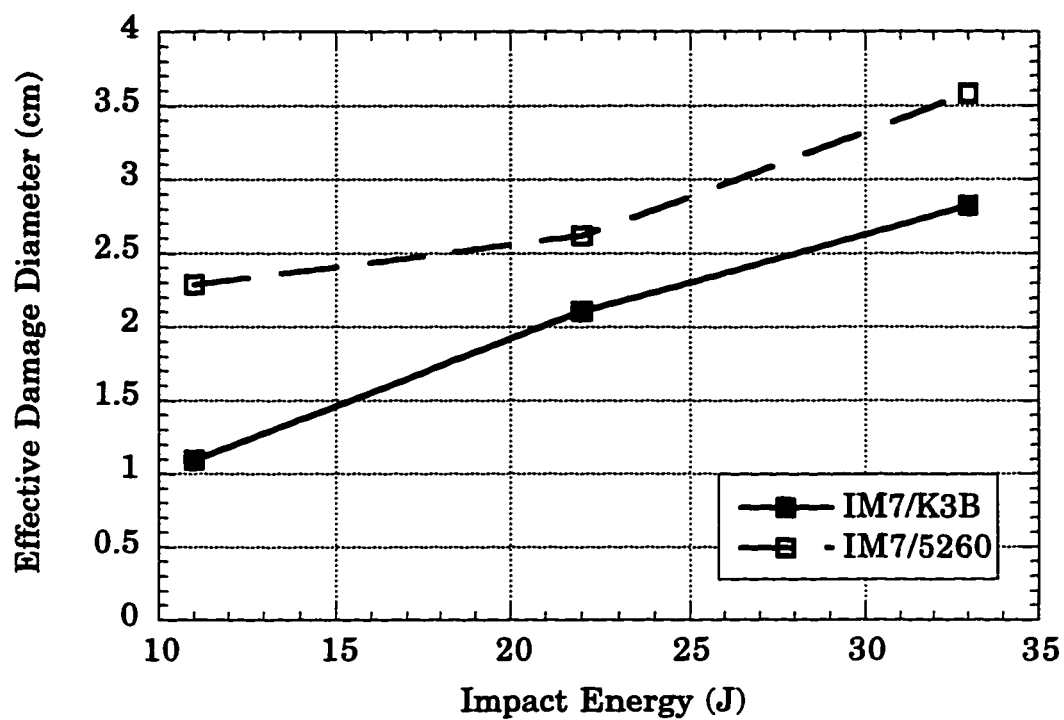


Figure 6.8 Damage diameter for CAI specimens with zero aging

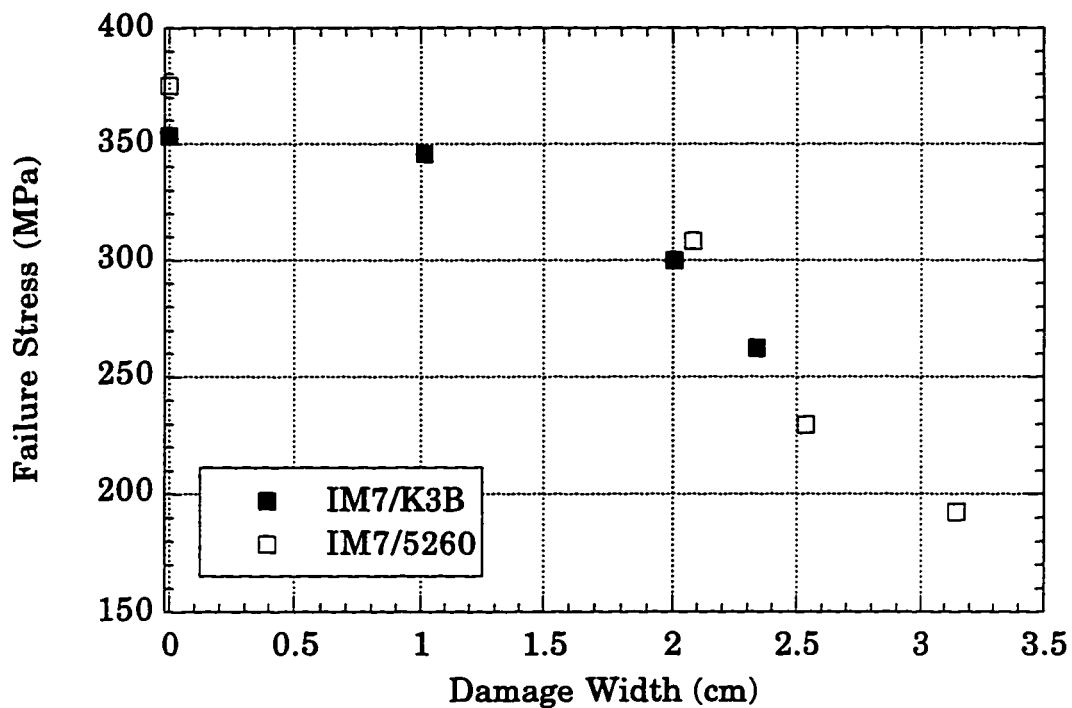


Figure 6.9 CAI failure stress vs. damage width

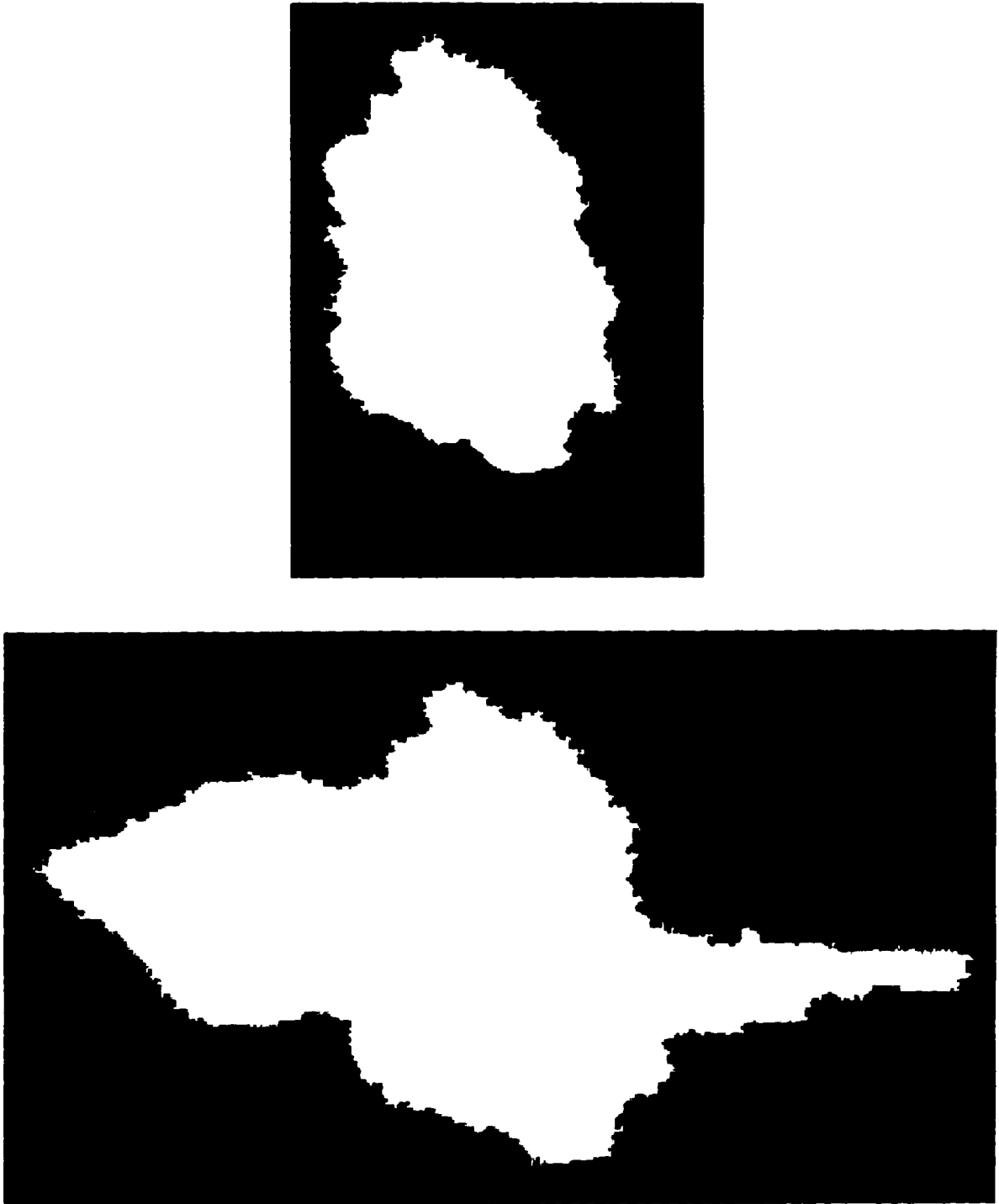


Figure 6.10 Damage before and after loading to 90% of failure

### *6.1.3 CAI strength of aged specimens*

The response of the two materials to elevated temperature aging is different. IM7/5260 degrades primarily due to oxidation, with degradation growing in from surfaces exposed to air. The degradation rates are driven by temperature and the availability of oxygen. IM7/K3B degradation is largely independent of temperature or the presence of oxygen. The results of CAI testing will be discussed separately for the two materials.

Aging of IM7/5260 at 149°C seems to have only a small effect on the CAI specimens (see Figure 6.11). Specimens impacted at 33.9 J show no variation with aging time for up to fourteen months of aging. These results agree with the degradation growth discussed in Section 3.1.3.

Specimens impacted at 22.6 J were aged up to 28 months and show some effects due to aging. Statistical variance of the data was calculated using the F statistic. The statement that aging time had a significant effect on the CAI strength was satisfied to the 95% level. The statement was not satisfied at the 99% level. Therefore, it is likely that the changes in average strength at longer aging times are indeed due to aging and not merely an artifact of data scatter, but it is not a certainty.

A line was fitted to the data for CAI strength of specimens aged at 149°C. Judging from degradation at higher temperatures, it is likely that the degradation rate will remain constant. The correlation between the curve fit and the data was 0.362, indicating the curve fit was only a small improvement over a flat line. Because of the low correlation of the curve fit, projections based on this numbers are questionable. Therefore predictions of the CAI strength of IM7/5260 aged at 149°C will not be made here.

Specimens impacted at 22.6 J after aging (type b tests) have a higher CAI strength than those impacted before aging. The rise is due to a post cure of the polymer material, shown by the rise in  $T_g$  (see Section 3.3). The increase is not seen in specimens impacted before aging because the slight oxidation degradation will negate increase due to post curing.

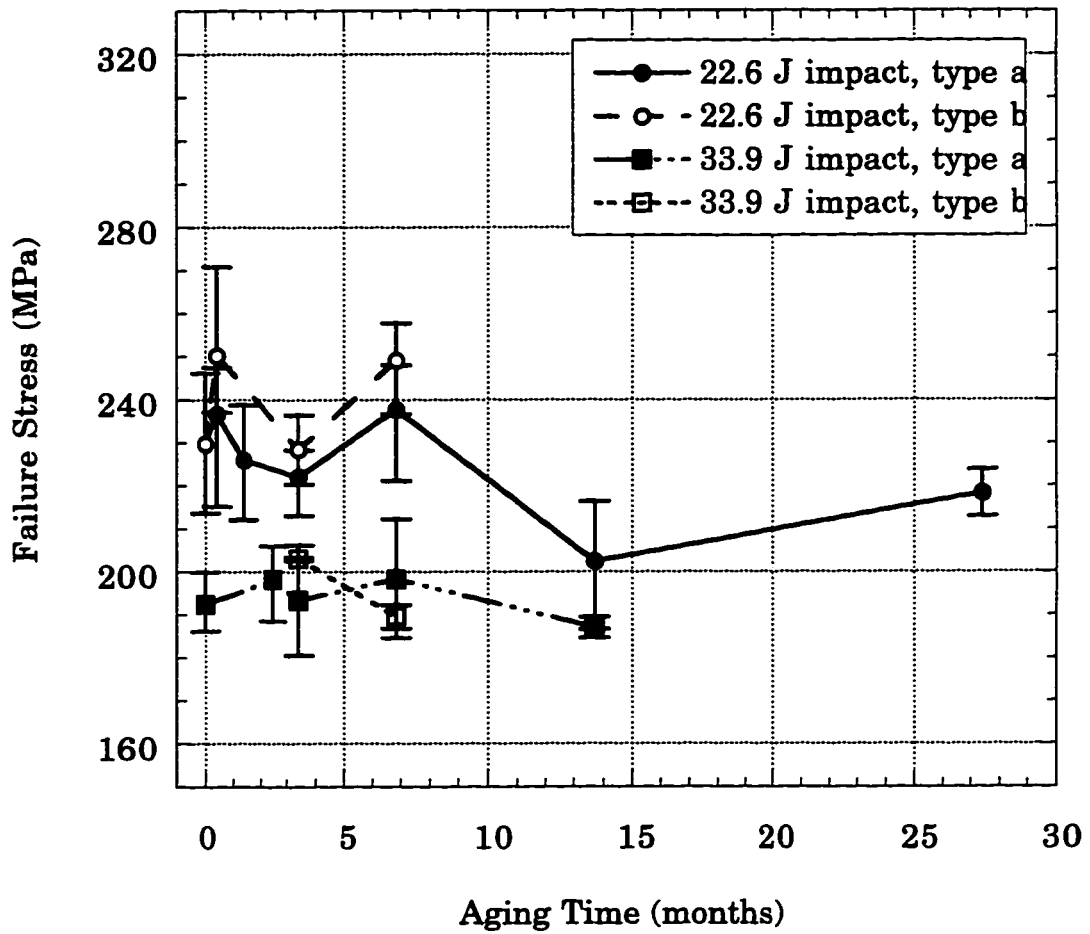


Figure 6.11 CAI failure stress for IM7/5260 specimens aged at 149°C

The higher temperature aging shows clearly the degradation of CAI strength in IM7/5260 (see Figures 6.12 and 6.13). The confidence interval for aging time being statistically significant is well over 99% for both aging temperatures. Linear curve fits of the data have correlation values of roughly 0.7. The data has a great deal of noise, but the trends are unmistakable.

At 177°C, the CAI strength has decreased by 25% after fourteen months of aging. This strength reduction is roughly equivalent for all impact energies. Projections based on the data for specimens aged at 204°C show that a 25% reduction is reached after only three months of aging. These degradation rates follow typical reaction laws with respect to temperature. This will be discussed further in Section 7.2.

Specimens aged at 177°C before impact again show slightly higher CAI strength than specimens impacted before aging. The data shows more clearly the trends discussed for the 149°C data. Initially, the matrix material experiences post curing. The polymer chains of the matrix material continue to link together, forming a stronger network which drives failure strength higher. This initial increase is not seen in specimens impacted before aging because the interior is exposed to oxygen and therefore the oxidation degradation is more severe in these specimens. After the initial increase, degradation begins to penetrate the outermost layers of the specimen and decreases in CAI strength follow the trends for specimens impacted before aging.

The CAI strength of type b specimens aged at 204°C does not show the initial increase from the post cure effect. This is explained by the much higher damage areas measured for these specimens. The post cure caused the material to become brittle and the impacts after aging caused very large damage areas. It is likely that the increase in strength properties due to post cure exists, but this increase is overshadowed by the decrease in strength due to a much greater damage area.

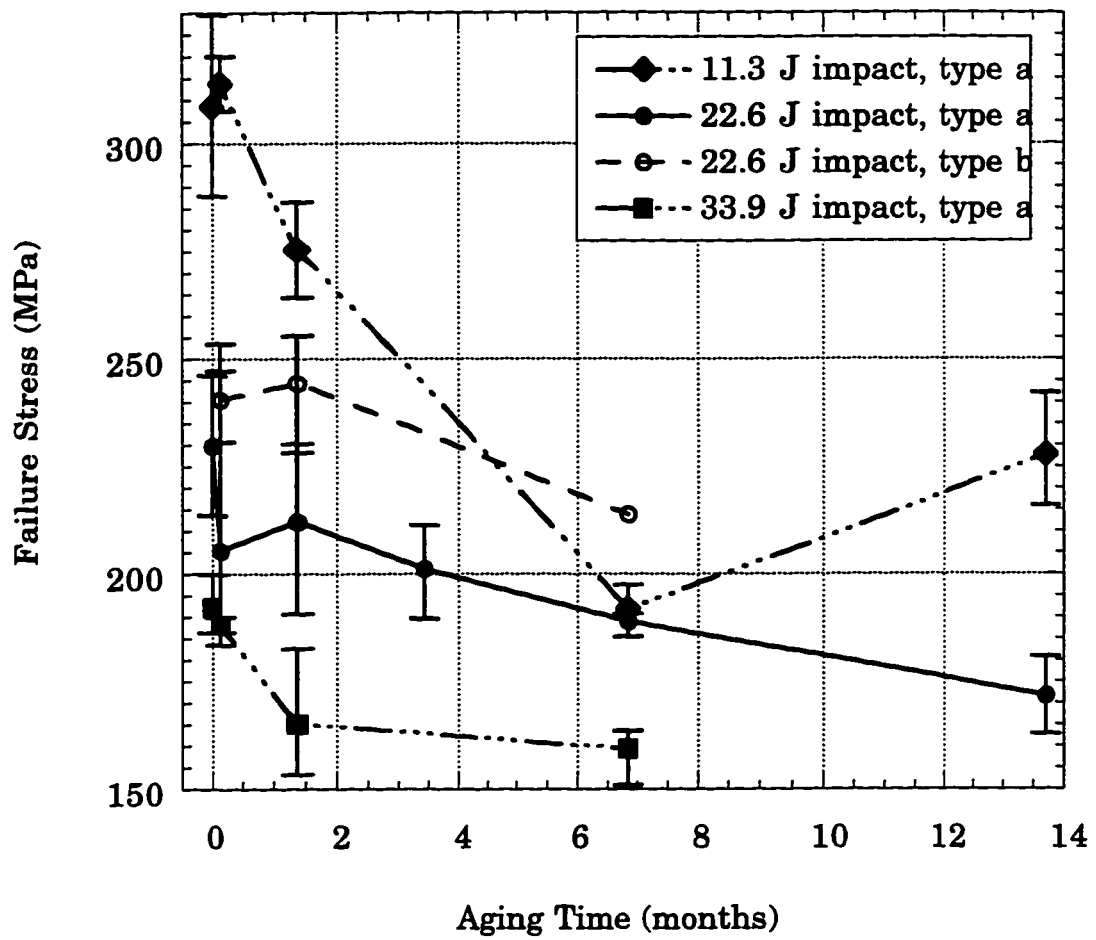


Figure 6.12 CAI failure stress for IM7/5260 specimens aged at 177°C

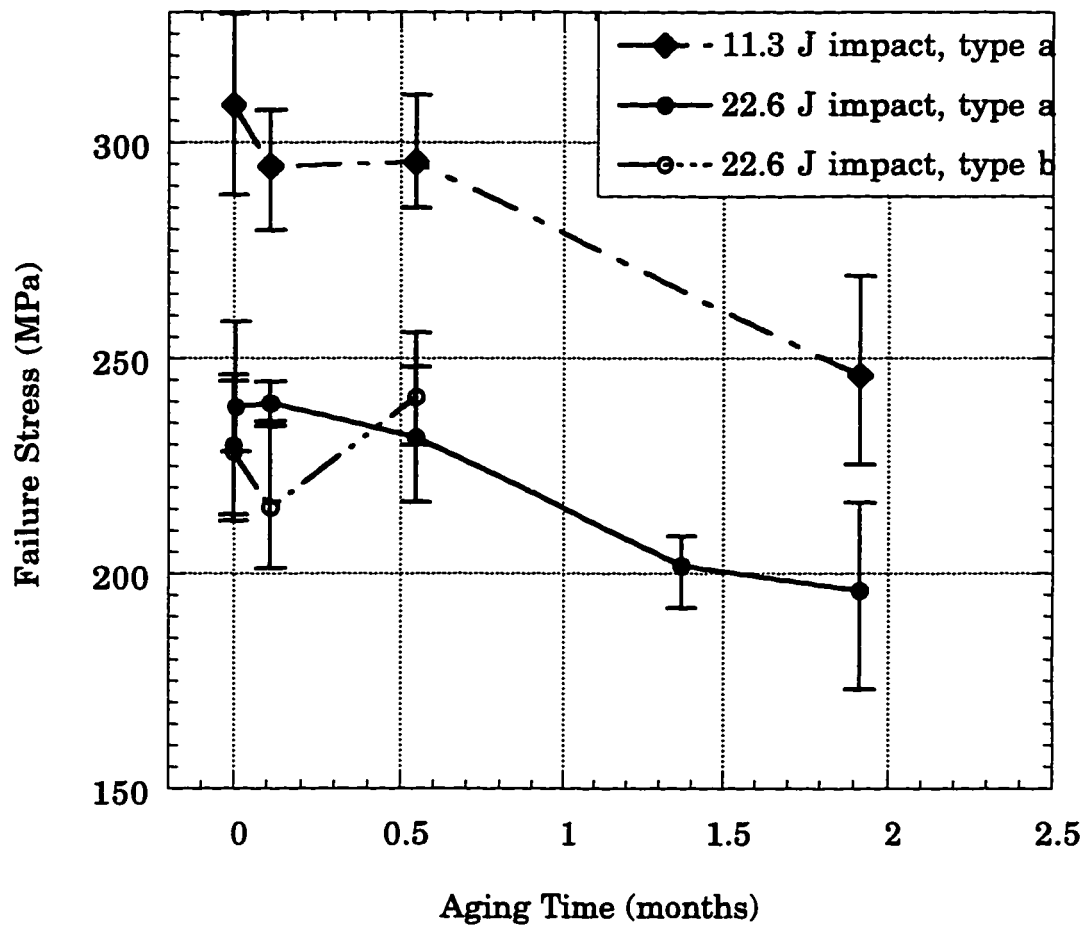


Figure 6.13 CAI failure stress for IM7/5260 specimens aged at 204°C

For all IM7/K3B specimens, there is a general trend for CAI strength to decrease for aging times up to six months (see Figures 6.14 through 6.16). Decreases are on the order of 10% with standard deviation of data points on the order of 5%. While these changes are small, a statistical analysis verifies their significance. Data was combined for all temperatures, and evaluated for variation with respect to aging time.

Each of the three impact energies were evaluated separately. As can be seen in Figure 6.15, specimens impacted at 11.3 J were generally unaffected by aging time. The confidence interval for the hypothesis that CAI strength decreased for aging times less than six months was below 95%. These specimens had failure strength very near to that of undamaged panels. Some of these panels failed due to stress concentrations near the damage, but others failed at the point of load application. Such failure modes were more influenced by the alignment of the loading block than the aging of the specimen. Thus the data revealed no significant information about aging effects.

Aging up to six months was significant for the remaining data. Specimens impacted at 22.6 J had a 99% confidence interval, and specimens impacted at 33.9 J had a 95% confidence interval. Since both sets of data showed the same trends, the statistical data was combined to calculate the confidence interval for all specimens impacted at either 22.6 or 33.9 J. This calculation yielded a confidence interval well over 99% for the hypothesis that aging time causes significant decrease in CAI strength.

A very significant observation is that aging degradation is independent of temperature. This behavior is contradictory to reaction kinetics. The exact causes of this anomaly are as yet unknown, but the effects on CAI strength are easily determined. This will be discussed in greater detail in the following chapter.

After six months of aging, the decrease in CAI strength proceeds at a slower rate. The degradation reaction approaches saturation, and further aging is expected to cause smaller and smaller changes in strength.

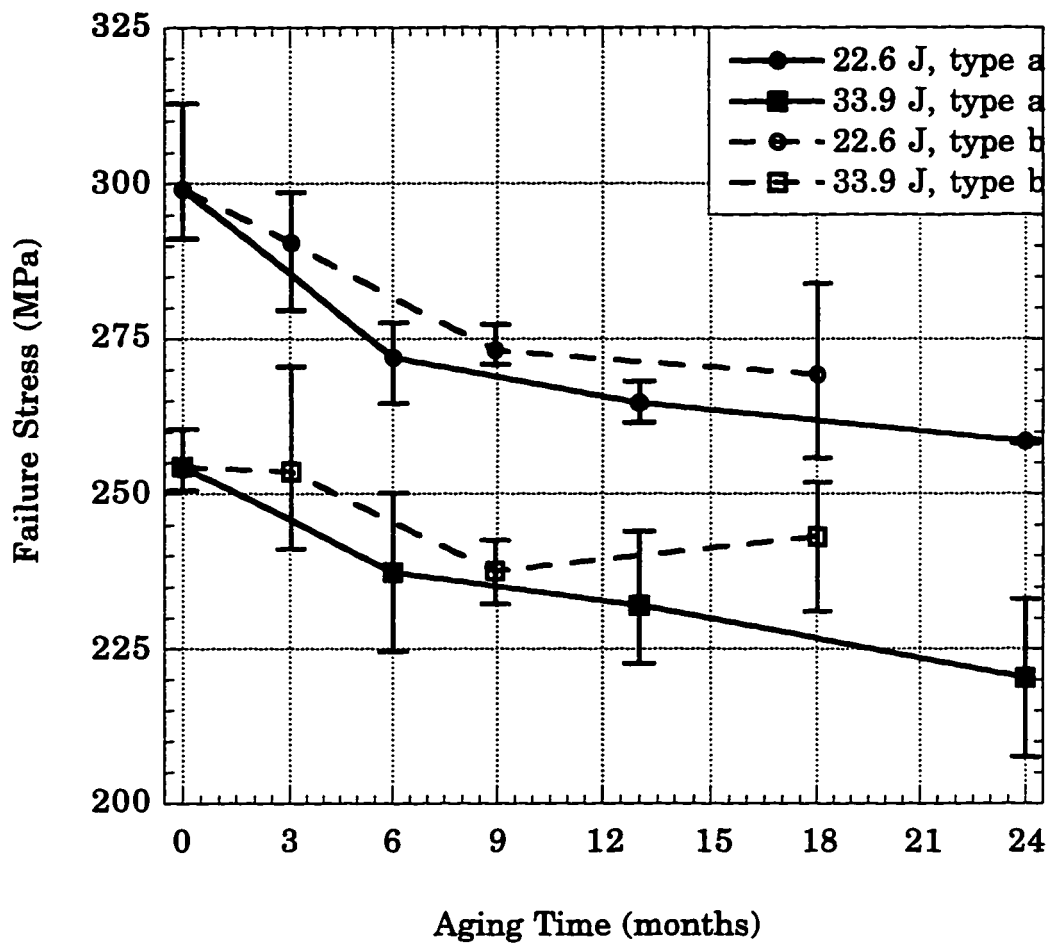


Figure 6.14 CAI failure stress for IM7/K3B specimens aged at 149°C

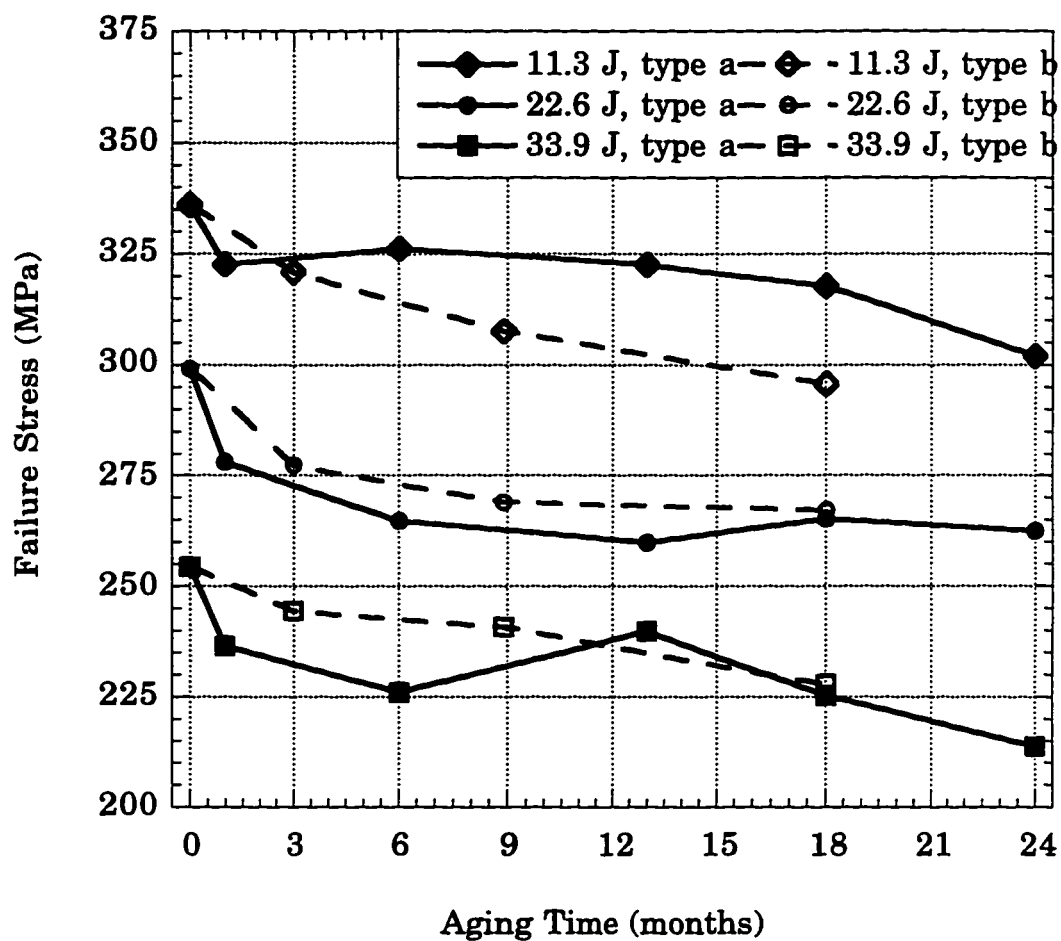


Figure 6.15 CAI failure stress for IM7/K3B specimens aged at 177°C

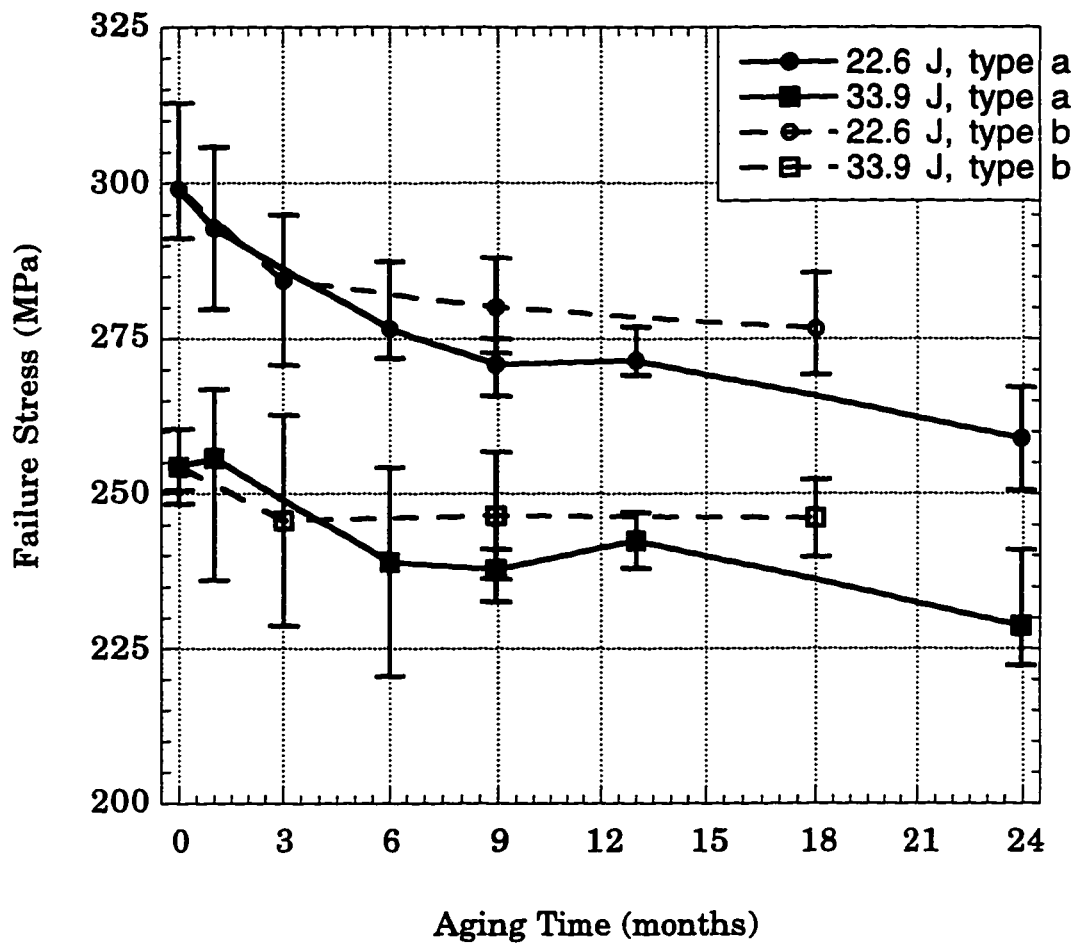


Figure 6.16 CAI failure stress for IM7/K3B specimens aged at 204°C

The trends for CAI strength of specimens aged before impact follows the trends of specimens impacted before aging. That is, the CAI strength decreases initially but then reaches a steady state value and remains constant. The data for this type of impact event is dependent on temperature however. At 149°C and 177°C, the strength of specimens with type b impacts is significantly higher than specimens with type a impacts. Data for both aging temperatures show a 99% confidence interval for the difference between the two type of impacts to be statistically significant. However, there is no difference between data for the two types of impact for specimens aged at 204°C.

#### *6.1.4 Impact damage in aged specimens*

Due to the post curing effect, the polymeric matrix of a composite becomes stronger, with increasing molecular weight and bond density. However, the post cure can also decrease toughness by making the material more brittle. Lower compliance of the specimen leads to less energy stored by elastic deformation, and therefore more energy absorbed by the creation of damage. This increased damage has been measured directly for IM7/5260 with C-scans.

The damage areas of IM7/5260 specimens which were impacted with 22.6 J of energy after aging are shown in Figure 6.17. These data follow trends similar to the data for  $T_g$  changes due to aging discussed in Section 3.3. Both the  $T_g$  change and the impact damage area are related to the amount of post cure. Aging at 204°C causes immediate increases in damage area due to impact, with changes occurring more slowly at the lower temperatures. After the initial increase, the damage area approaches a steady state value.

The data scatter for damage area is quite high. The reason for this high data scatter is revealed by examination of the internal signal C-scan. Most specimens had radially symmetric damage which followed the K-rule described in Chapter 5. In all cases of uncharacteristically high damage area, large delaminations were found in the C-scan. Figure 6.18

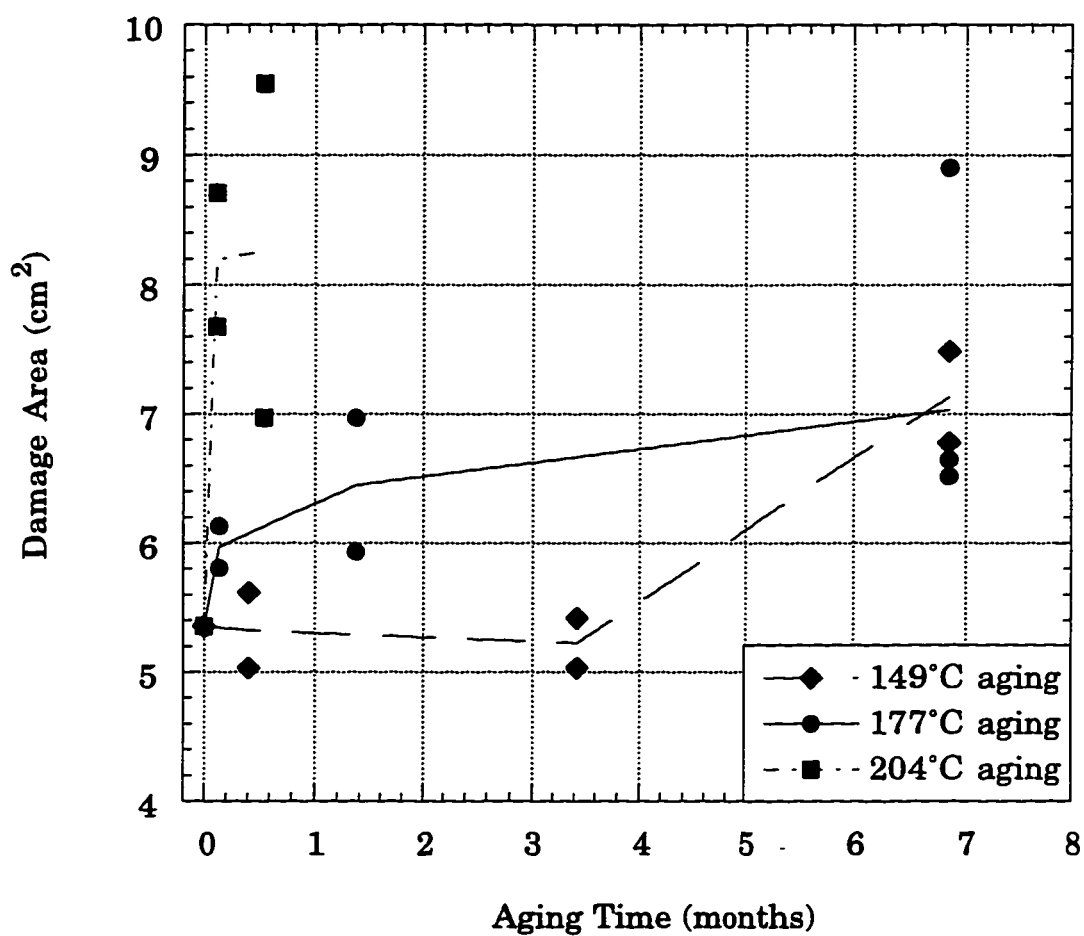


Figure 6.17 Damage area for IM7/5260 specimens impacted with 22.6 J of energy after aging



Figure 6.18 Example of symmetric (top) and asymmetric (bottom) damage

provides an example of this type of delamination. The first image shows the internal signal of a specimen without large delaminations. The second image shows a specimen with the same impact energy level and aging. The second image contains exceedingly large delaminations above and to the lower right of the impact. These delaminations are believed to form in areas where the toughening agent in IM7/5260 is below design level.

Elevated temperature aging has little affect on the impact damage area of IM7/K3B. Only data for specimens aged at 177°C before impact are shown in Figure 6.19, but the values are typical for all data. There is some variation with respect to aging time, and interpretations can be made about the aging of the material. But the statistical significance of the variations is low and so the changes are due to data scatter.

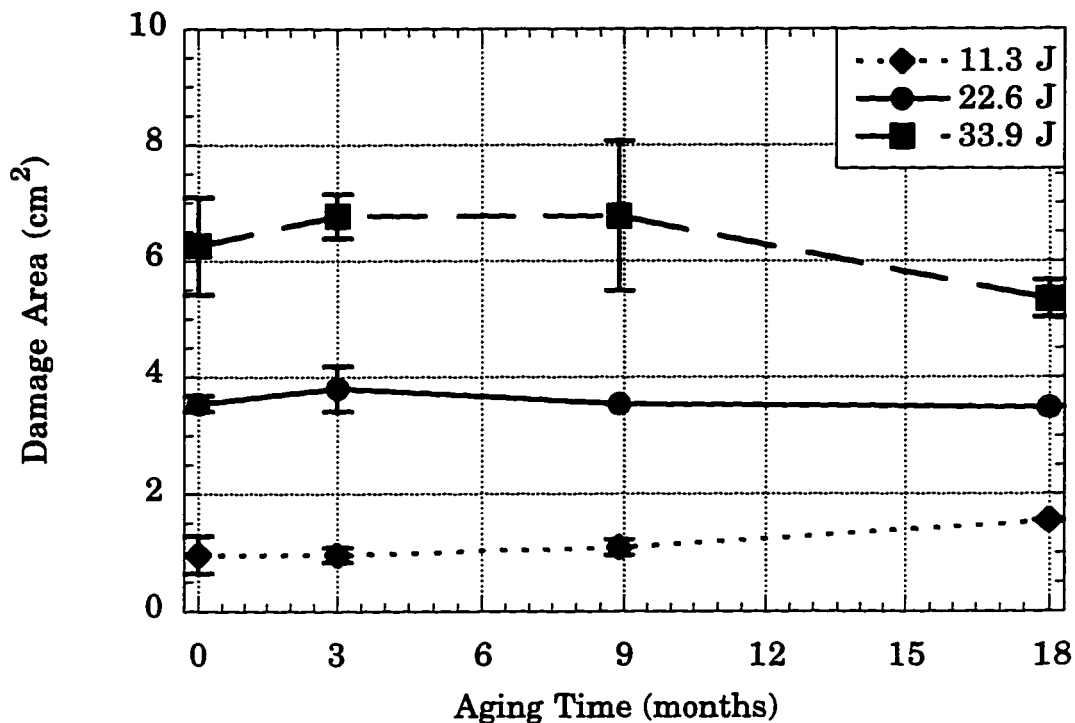


Figure 6.19 Damage area for IM7/K3B specimens impacted after aging at 177°C

## 6.2 Out-of-plane displacement

Although the CAI test fixture supported the specimens at the edges, bending occurred near the failure load. The impact event imparts a slight curvature to the specimen, with a radius on the order of hundreds of inches. The asymmetric impact damage also contributes to specimen bending at high load levels [84]. To account for the effect of bending on the stress near the damage, curvatures were measured using shadow moiré. The theory and experimental procedure for conducting the shadow moiré testing is explained in Appendix A. The calculated bending strains were verified by using back to back strain gages near the center of the specimen.

### 6.2.1 Results of shadow moiré testing

All specimens curved in half wave mode shapes. The impact surface was always on the interior of the curve, because of pre-existing curvature from impact. IM7/K3B specimens showed no change in local buckling around the impact damage during testing. A typical shadow moiré pattern photographed during CAI testing is shown in Figure 6.20. Impact damage appears in the center of the image. The reference cone is seen in the lower left corner. Strain gages appear at the top of the image, and the metal frame surrounding the moiré image holds the reference grating in place.

Sublaminar delaminations often grew during loading of IM7/5260 specimens. This sublaminar buckling has been investigated in other work [93]. The area of the buckled sublaminar does not normally grow larger than the original delamination area. Failure predictions are made assuming the buckled area is equal to the delamination area. Therefore, growth up to this maximum area is unimportant.

Two of the IM7/5260 specimens had slow sublaminar buckling growth which exceeded the measured delamination area. Delaminations grow between the outermost 45° ply and the next 0° ply near failure, as determined by the C-scans shown in Section 6.1.2. Judging from the

frequency of audible damage growth, these type of delaminations are common in CAI specimens near failure. Buckling in only the outer 45° degree ply, while the 0° degree ply remained stable, is the most likely explanation for the observed buckling growth in the two IM7/5260 specimens. Thus the observed sublaminated buckling did not represent a significant change in the failure mode. Shadow moiré images of the damage growth sequence are shown in Figure 6.21.

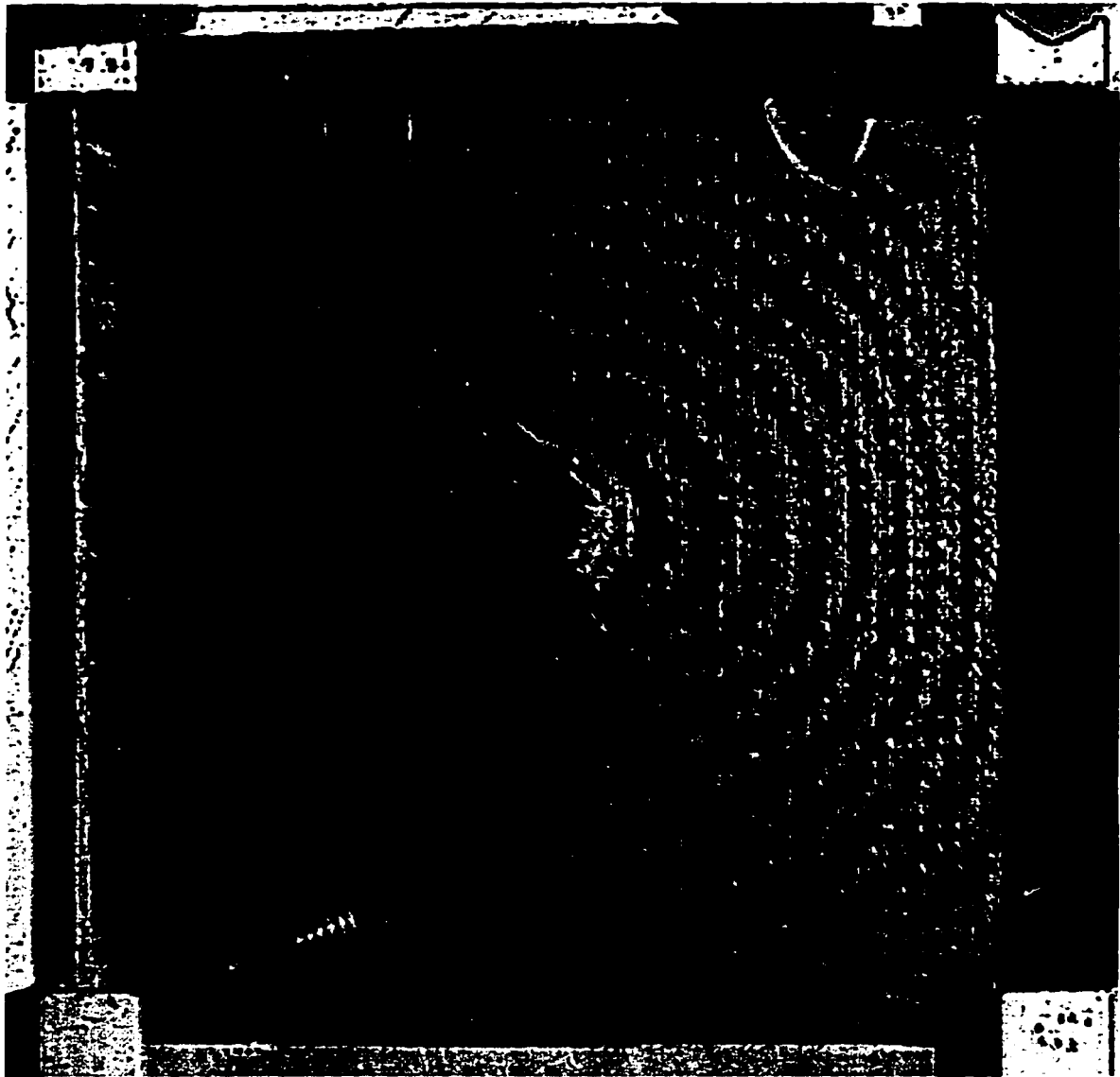
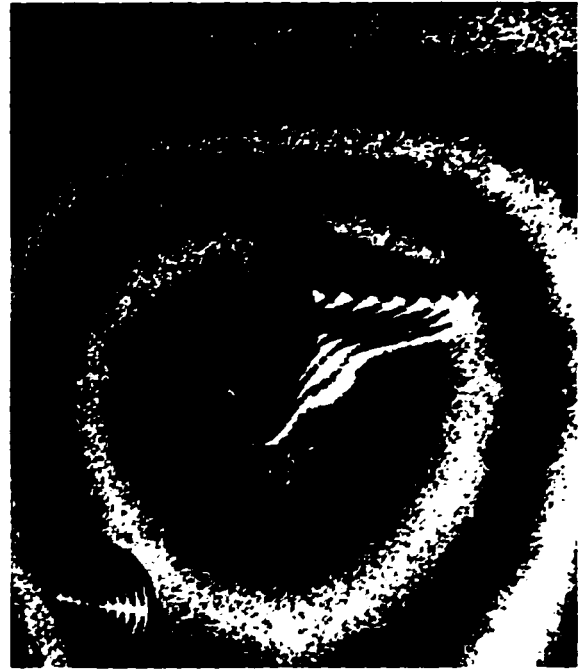


Figure 6.20 Shadow moiré fringes of a CAI specimen near failure



183 MPa



196 MPa



208 MPa



failure

Figure 6.21 Loading sequence showing outer ply buckling in IM7/5260

### 6.2.2 Specimen bending

The curvature of the surface was determined by the shadow moiré displacement field. The displacement of the midpoint of the specimen was measured directly with a dial gage during testing. Using these data, the displacement along the centerline of an axially loaded CAI specimen was calculated and is plotted in Figure 6.22. The inflection near the top of the specimen is due to the load application. The boundary condition is not truly clamped, nor purely simply supported. This is because there is local deformations at the loading ends which allow rotations, but there are also moments which resist rotation. Also, the impact damage reduces stiffness, causing curvature to be greatest in the impact region.

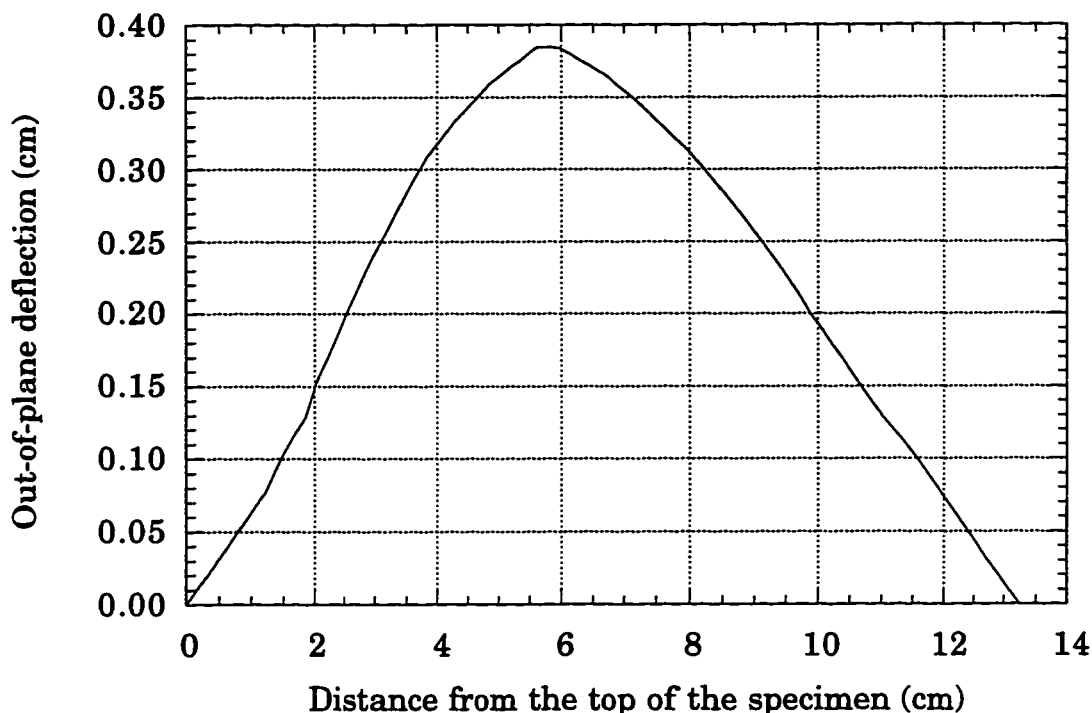


Figure 6.22 Out-of-plane deflection along the centerline of a CAI specimen near failure

Bending strains were calculated directly from the measured curvature of the specimen. The bending strain is simply  $\epsilon_b = \kappa z$ , where  $z$  is the distance from the midplane. Curvature was calculated from a curve fit of the out-of-plane displacement data in the region of interest. The curve fit was of the form

$$w = A_1 \sin\left(\frac{px}{6}\right) + \left[1 - B_1 \cos\left(\frac{px}{3}\right)\right] \quad (6-1)$$

where  $w$  is the out-of-plane displacement,  $x$  is the distance from the top of the specimen, and  $A_1$  and  $B_1$  are parameters. The curvature is then calculated as

$$\kappa = \frac{\partial^2 w}{\partial x^2} = -A_1 \left(\frac{p}{6}\right)^2 \sin\left(\frac{px}{6}\right) + B_1 \left(\frac{p}{3}\right)^2 \cos\left(\frac{px}{3}\right) \quad (6-2)$$

As stated previously, dial gages were used to measure the  $w$  deflection at the center of the specimen during CAI testing. Typical deflection vs. load curves are shown for each impact energy level in Figure 6.23. Since the shape of the curve for a given specimen remained constant during loading, curvature was a linear function of the maximum out-of-plane deflection. Therefore, bending strain could be calculated using the curve fit of Figure 6.22 and the displacement data of Figure 6.23. The surface strains were also measured experimentally using strain gages located near the impact damage for a limited number of specimens. Bending strains calculated using the two methods were in close agreement, verifying the shadow moiré method of calculating bending strain (see Figure 6.24). This was the method used for most bending analysis.

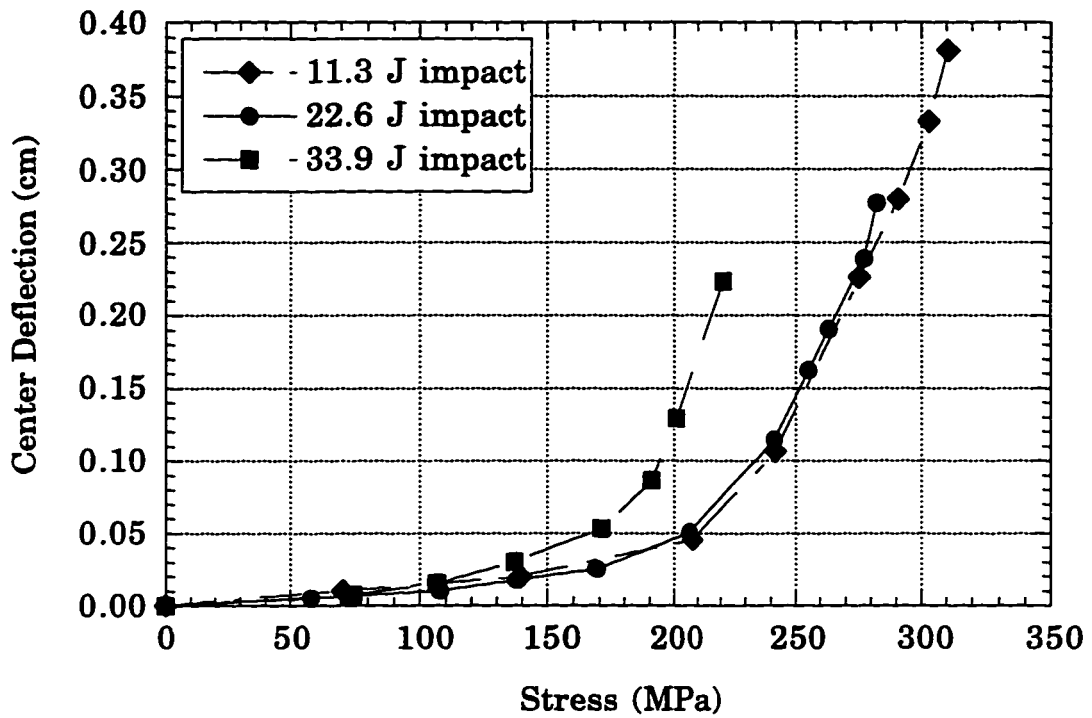


Figure 6.23 Center deflection during loading of CAI specimens

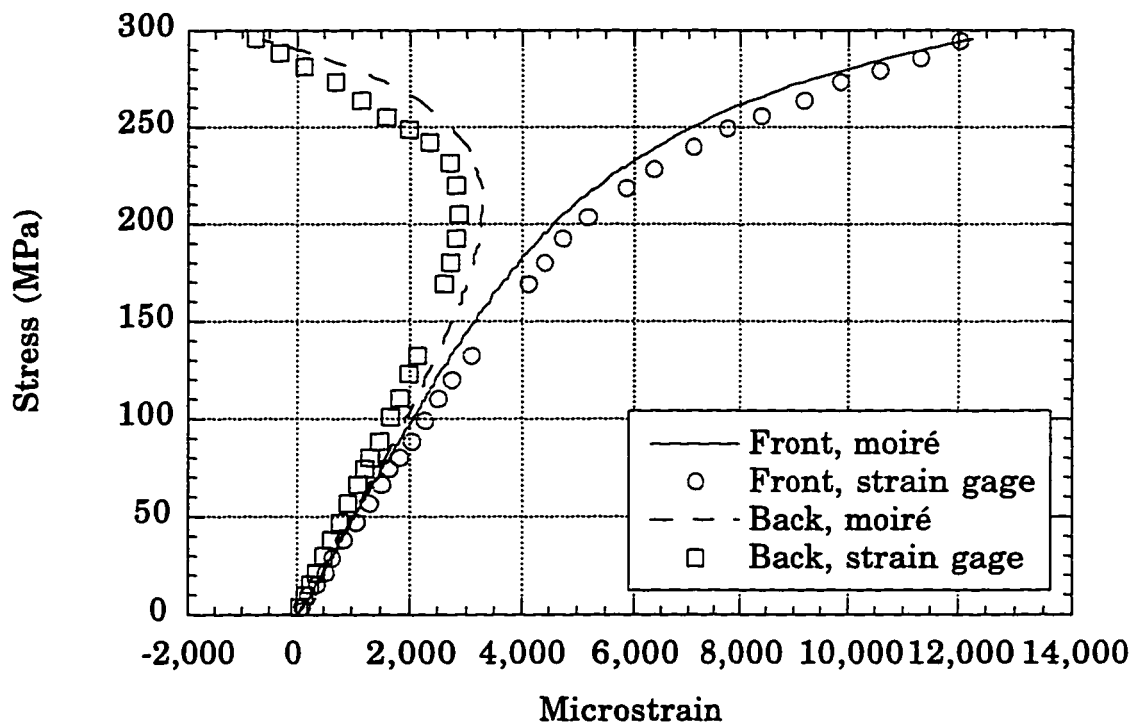


Figure 6.24 Strains near the impact damage during loading

### 6.3 Near damage strain fields

For a few selected specimens, moiré interferometry was used to measure the in-plane displacement field around the impact point. Moiré interferometry is an established technique [93-98] that uses a diffraction grating on the specimen and an interference pattern of laser light to create lines of constant in-plane displacement. A thorough explanation of the fundamental theory and use is given by Daniel Post [94]. A summary of this work, as pertains to this research, is included in Appendix B.

Figure 6.25 shows the strain field for an IM7/K3B specimen aged nine months at 204°C before impact at 22.6 J. The applied load for this image is at a stress level of 222 MPa, 80% of the failure load. Also shown in the figure are the delamination area and the fiber damage radius. Delamination area was measured by C-scan, and is represented in the figure as the white outline surrounding the impact point. Fiber damage radius was calculated from the depth of the impact indentation. Precise measurements were not possible from the C-scan image or surface of the CAI specimen. Therefore, impact dent depth and impactor tup geometry were used to calculate impact dent width. This was taken to be the fiber damage radius, and is represented by a dark circle.

As seen in Figure 6.25, strain is very high across the impact center within the fiber damage radius. Splits between fibers on the surface of the specimen appear as lines of low strain extending along the 45° angle from the impact center. These cracks develop strain concentrations at their tips, and often grow longer during testing. However, the outer 45° ply does not carry the majority of the load, and such crack growth does not precipitate failure of the specimen. Only crack growth in the 0° ply, indicated by cracking transverse to the loading direction, precipitated specimen failure. Another prominent feature of the strain field are the ripple patterns, which are caused by fiber waviness on the surface.

A finite element model was formulated to represent the CAI specimen. The damage was modeled as a soft inclusion with a radius equal to the fiber damage radius. The modulus properties of the inclusion were taken from the experimental moiré image. The calculated strain field is shown in Figure 6.26. This simplified strain field does not capture the many details of the experimental strain field. However, the strain fields are similar along the centerline, transverse to the loading axis. Since failure is known to occur at the edges of the damaged region along this line, failure can be predicted from the concentrations in the calculated strain field.

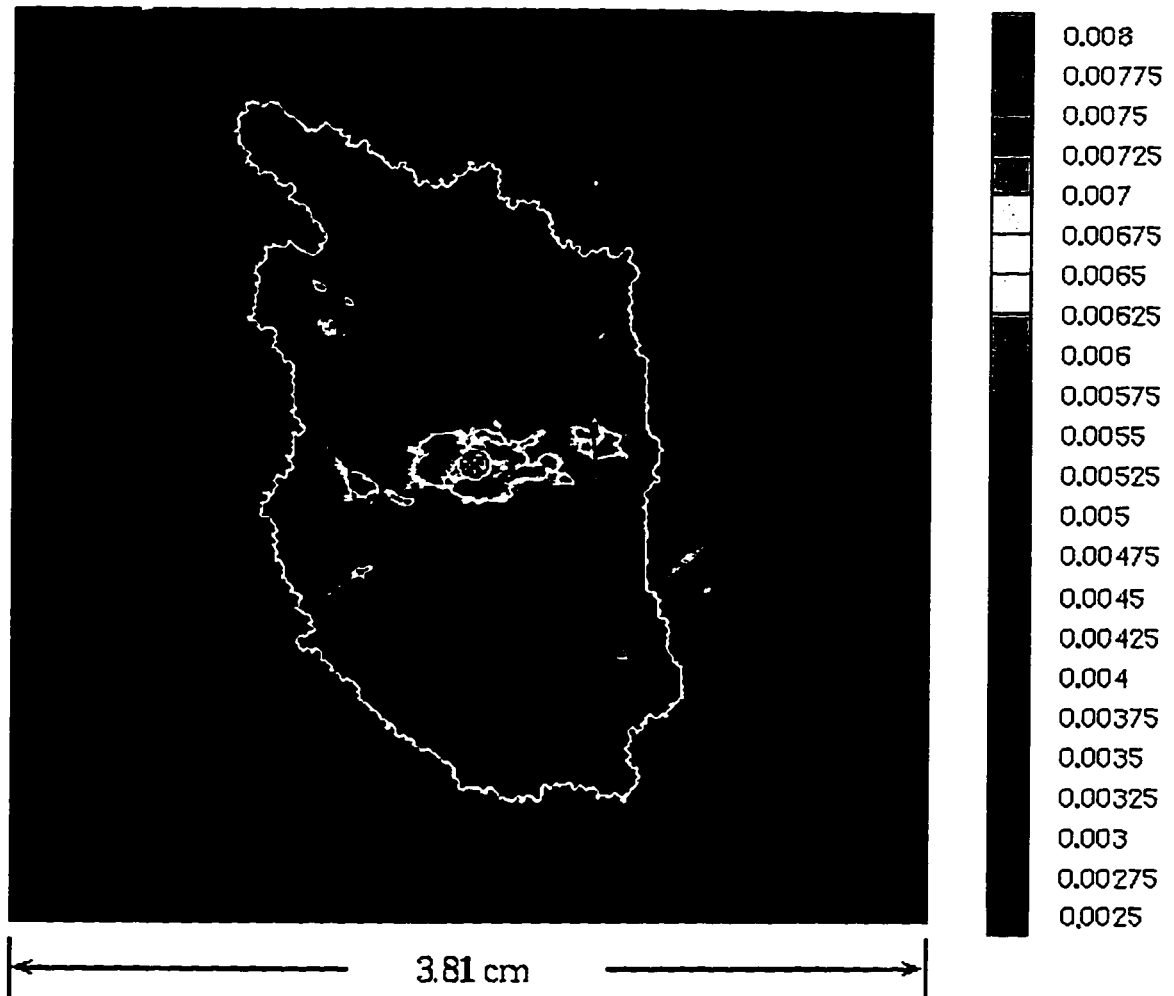


Figure 6.25 Axial strains for an IM7/K3B CAI specimen at 80% of failure stress, measured by moiré interferometry

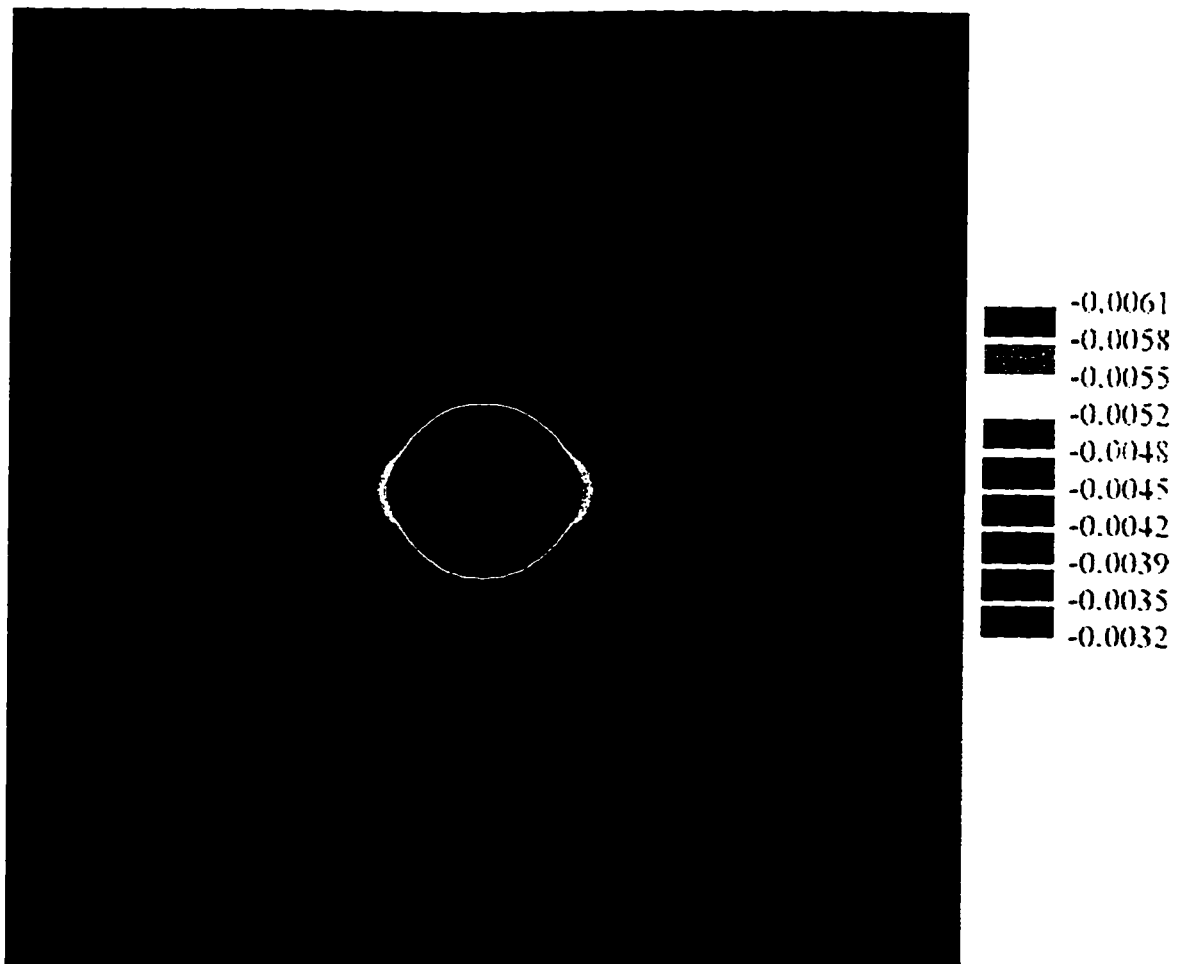


Figure 6.26 Axial strains for an IM7/K3B CAI specimen at 80% of failure stress, calculated by finite element methods

## Chapter 7

# AGING EFFECTS ON COMPRESSION AFTER IMPACT STRENGTH

As explained in Chapter 2, elevated temperatures can cause chemical and physical changes in the matrix material of a composite structure. This change in properties alters the CAI strength of the composite panel. This chapter evaluates each aspect of thermal aging and the effects on CAI strength.

### 7.1 Post-cure of the Matrix Material

Changes in glass transition temperature showed that the polymeric composite continues to cure during aging. Aging at 204°C completes the curing process within a few months, after which time no more post-curing occurs. Specimens aged at lower temperatures do not achieve complete curing within the aging time studied, nine months. Continuation of the curing process results in an increase in the bond density of the polymer. Thermoset materials have more cross-linking, while thermoplastic materials have a higher molecular weight. These chemical changes will increase the stiffness of the polymer. However, transverse stiffness measurements showed little evidence of increased stiffness during the post-cure.

Post curing did alter the damage resistance of IM7/5260. Increased cross-linking resulted in a more brittle matrix, thereby reducing the interlaminar toughness. Specimens aged before impact had larger damage areas than specimens impacted before aging. The rise in damage area was proportional to the change in  $T_g$ , as seen by comparing Figures 3.30 and 6.17. Over the lifetime of the aircraft, it is projected that the damage size of specimens impacted after aging would be equivalent to the large damage size of specimens aged for one month at 204°C. Damage area of specimens aged at 177°C would reach this size after a few years of aging.

## 7.2 Matrix stiffness changes

Physical aging can also increase the stiffness of the matrix material. The void content decreases during aging, making the material more dense and therefore less compliant. Laminate theory was used to calculate the changes in specimen stiffness due to changes in transverse stiffness,  $E_2$ , and shear stiffness,  $G_{12}$ . The effect of ply stiffness changes on buckling stress of the sublaminates and bending strains in the panel were also calculated.

A stiffness change of no less than 7% is required to produce a 1% change in the stiffness, bending strains, or sublaminates buckling load of a quasi-isotropic laminate.  $E_2$  was measured from 90° unidirectional specimens, aged up to three months. Only IM7/K3B specimens aged at 204°C showed changes in  $E_2$ , and the increase was a mere 2%. Therefore, stiffness changes due to aging can be ignored for the quasi-static loading case of CAI strength.

## 7.3 Changes in impact resistance

Elevated temperature aging has no effect on the impact damage area of IM7/K3B. The thermoplastic matrix is undergoing a post-cure process, as shown by the  $T_g$  data in Section 3.3. The characteristic damage state is different for this material. IM7/5260 has large delaminations, absorbing impact energy through the formation of fracture surfaces between plies. The tougher thermoplastic K3B has only a small amount of delamination. While the energy absorbed by delamination damage depends on the matrix material, energy absorbed by fiber breakage is dependent on the fibers. Since the fibers are unaffected by aging, the energy absorbed by fibers during impact is constant. In IM7/5260, much of the energy was absorbed by delamination, and so the damage area was sensitive to aging. However, the damage incurred by impact for IM7/K3B specimens has a large proportion of fiber damage. Thus, the ability of the material to resist impact damage remains constant during aging.

As stated in Section 7.1, the damage area increases substantially for IM7/5260 specimens aged before impact. Post-curing causes the matrix to become more brittle, and larger delaminations form during impact. The larger damage areas do not directly lead to lower CAI strength, however. Because of the bending curvature of the specimen at high loads, the failure occurred around the fiber damage on the impact side of the specimen. The sublaminar buckling was not the dominant factor in specimen failure, and so the larger damage areas were not important in this case.

This does not mean that the extent of damage is not important in the CAI strength of specimens tested in this study. The extent of fiber damage and the associated matrix and interlaminar cracking are the determining factors for the CAI strength. However, for a given impact energy and laminate properties, changes in delamination area have only a small effect on the CAI strength. An illustration of this fact is given by the IM7/5260 specimens with known delamination areas, used as data in Figure 6.17. For each pair of specimens with equal aging, the specimen with the larger damage area had greater CAI strength. The large damage areas absorbed a great deal of the impact energy, leaving less energy to be absorbed by broken fibers and matrix cracking. Although the larger delamination area reduced compressive strength of the laminate, the lesser fiber damage around the impact point increased the strength. Since the strength is dominated by fiber damage, the net result was greater CAI strength.

#### 7.4 Changes in fracture toughness

Delamination growth is governed by the interlaminar fracture toughness of the matrix material. For many graphite/epoxy composite materials, fracture toughness determines the sublaminar growth and thus the failure of CAI specimens. However, the toughened bismaleimide and thermoplastic materials used in this study have high interlaminar fracture toughness. The quasi-isotropic laminate fails due to kinking in the 0° plies before the critical fracture toughness is reached. Therefore, the degradation of  $G_{Ic}$  discussed in Section 3.1 has no effect on CAI strength.

## 7.5 Oxidation zone growth

The dominant effect of elevated temperature aging on composite materials is the oxidation of exposed matrix surfaces. Oxidation degradation reduces the strength of the material, and leads to lower failure stresses in structural components. For IM7/5260, the degradation is obvious. The interatomic bonding in the polymer chain is broken and the residue leached away, leaving bare fibers with little matrix support. Degradation of IM7/K3B is very subtle. Only by use of the most advanced analysis procedures can any chemical change be detected. K3B resin is virtually impervious to oxidation at the temperatures studied. However, polymers in the interphase region are degraded. The degradation reduces the shear strength near the fibers, resulting in the decreased strength values of the laminate specimens.

For panels impacted before aging, the CAI strength will be affected by oxidation immediately. The damaged region has a large degree of matrix cracking and ply delamination, which provides access for the oxygen. Because the failure occurs near the damage region, the degradation of the material in this area is critical.

Degradation growth past the stress concentration point near the damage is less important for the CAI strength of the materials in this study. Once transverse cracking failure begins in the load bearing 0° plies, the specimen becomes unstable and global failure occurs. Although the ply compressive strength increases as the crack grows into the laminate, the greater strength is insufficient to arrest the crack growth.

Specimens with a (45/0/-45/90)<sub>3s</sub> layup are more resistant to oxidation degradation when aged before impact. Since the load bearing 0° plies are protected from oxygen by the outer 45° ply, a delay in compressive strength degradation is observed. After degradation has proceeded through the thickness of one ply, the CAI strength degrades at a rate similar to the degradation of specimens impacted before aging.

## 7.6 Ply failure strength degradation

Oxidation degradation governed the reduction in CAI compressive strength. The undamaged failure stress of aged material was measured using the four point bend test, as described in Section 3.7. Specimens were cut before aging, so that the surface was directly exposed to air during the aging process. This provided a direct measure of the effect of oxidation degradation on the compressive strength of the 0° plies.

The failure stress data from four point bend testing was compared to the failure stress of CAI specimens. Data was normalized by the strength of the unaged material. As seen in Figures 7.1 and 7.2, there is an almost perfect correlation between the two measures of compressive strength. The simplified geometry of the undamaged four point bend specimen captures the aging degradation of the CAI specimen. The complicated stress state in the CAI specimen remains largely unaffected by the aging. The changes in material properties, specifically failure strength of the 0° ply, dominate the degradation effects. All other changes are secondary.

The number of data points for four point bend strength is small, and the maximum aging time is six months. The importance of the test was not anticipated, and only an exploratory test matrix was planned for the four point bend testing. Because of the inherent nature of research involving long term aging, more data cannot be gathered to immediately verify these findings with longer aging times. However, the data gathered is sufficiently conclusive to determine that reductions in CAI strength due to aging of polymeric composites are dominated by this reduction in ply compressive strength.

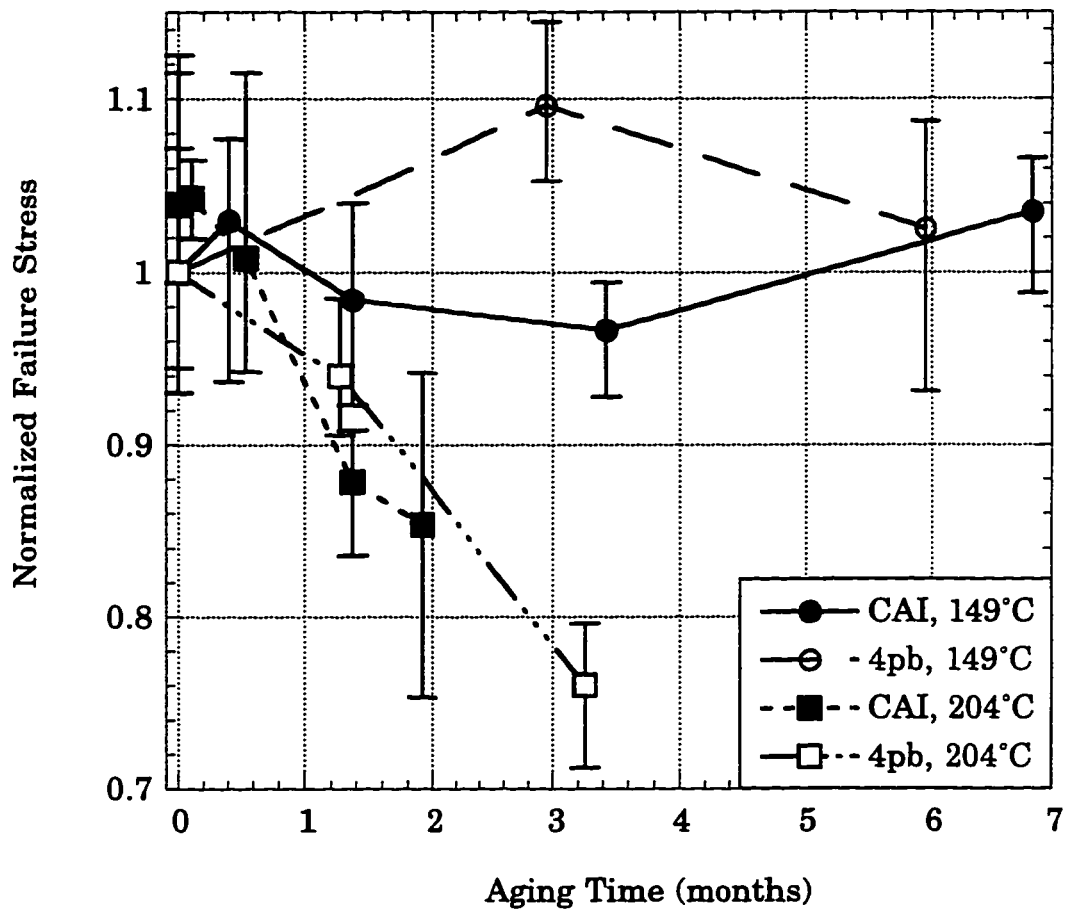


Figure 7.1 Normalized failure strength for IM7/5260 CAI and four point bend specimens

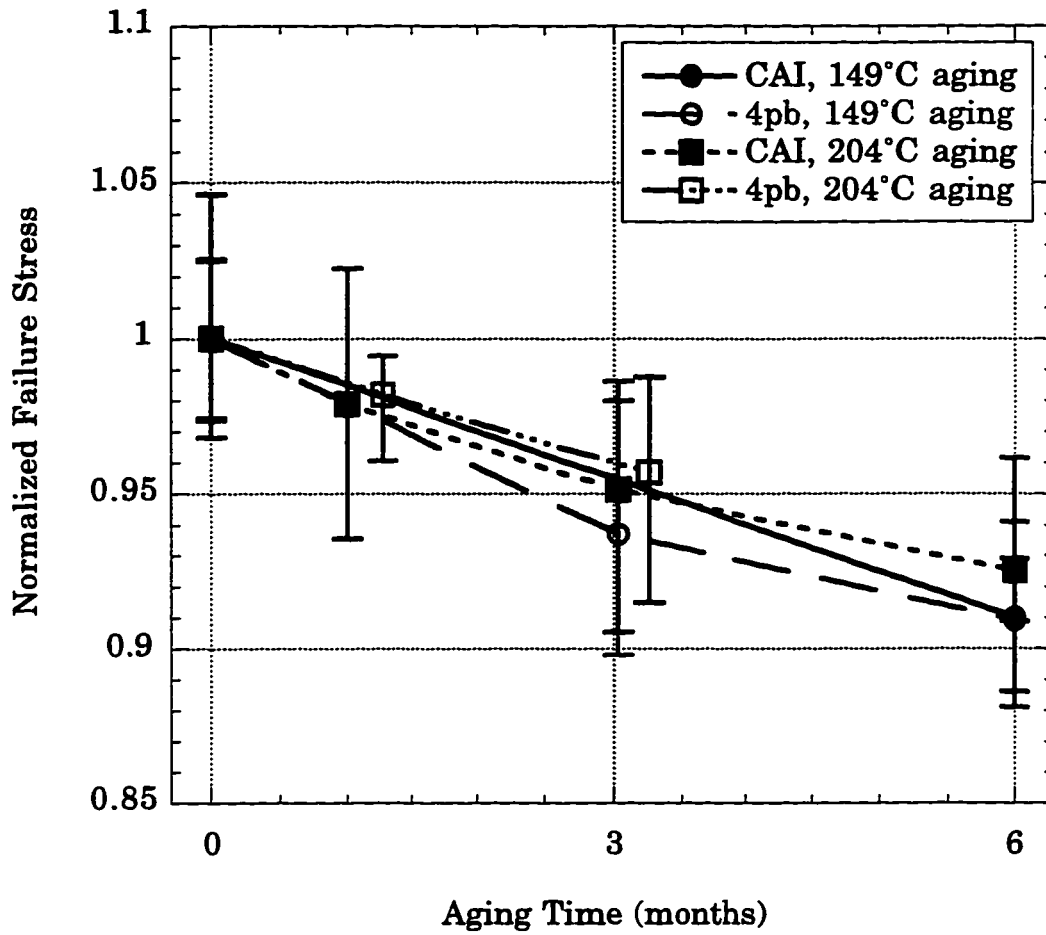


Figure 7.2 Normalized failure strength for IM7/K3B CAI and four-point-bend specimens

## Chapter 8

### CONCLUSIONS AND RECOMMENDATIONS

Determining the effects of elevated temperature aging on the durability of composite materials is important to the development of a passenger aircraft capable of supersonic cruise. The composite structure of such an aircraft will be subjected to low velocity impacts during the service life of the aircraft. The loss of strength caused by the impact of aged material is important to the design of the aircraft. This research has identified the significant factors of aging on durability, and their relative influences on strength loss.

An experimental program has been underway for many years at the University of Washington to determine the effect of aging on durability. The effect of time and temperature on the CAI strength and fracture toughness of IM7/5260 thermoset and IM7/K3B thermoplastic composites has been studied. An investigation of the chemical behavior during aging as relates to the structural properties of the material was also conducted.

Oxidation degradation grows into the surface of specimens from all surfaces exposed to air. The degradation growth was modeled using finite element methods. This finite element model can be used for complex geometries, and will be a useful tool in analyzing degradation of structural components.

The conclusions which can be drawn from this research address vital concerns about the durability of polymeric composite materials for use in elevated temperature environments. The data also raise questions which must be answered by further research. Knowledge and experience gained from this work will lead directly to new methods of investigation for answering these questions.

## 8.1 Material Properties Testing

Fracture toughness decreases at higher temperatures. Specimens tested at room temperature showed typical fracture growth characteristics for polymeric composites. However, specimens tested at elevated temperature are prone to an increasing fiber bridging influence. The test data was analyzed and a meaningful value, initial  $G_{Ic}$  at the crack tip, was found for mode I specimens. Other data proved to be of little use. The issue of excessive fiber bridging must be addressed with a full study of the experimental technique before any further fracture toughness testing is conducted at elevated temperature.

A discolored region was detected on mode II fracture surfaces near boundaries exposed to air during aging. The depth of this region grows with increasing aging time, following curves which can be modeled by diffusion/reaction equations. Discoloration depth grows faster parallel to the fibers, indicating that the chemical reaction occurs fastest along the fiber-matrix interface.

ESCA testing of aged IM7/K3B composites was unable to detect changes in the chemical structure of the matrix material. However, SIMS data showed conclusive proof of degradation in this material. The degradation was found on an ENF specimen aged at 149°C for two years. Microscopy studies show that the fracture surface of the material was in the interphase region between fiber and matrix. The bonds surrounding the nitrogen atom were broken, and the large PMDA type molecule was not observed in the spectrum. An extensive research program in this area would provide valuable data on the degradation process in K3B.

The  $T_g$  changes observed indicate that the material continues to cure during aging. The post-cure proceeds to completion within one month at 204°C, and more slowly at the lower temperatures. The  $T_g$  data also shows that physical aging occurs at higher temperatures. The only influence of these changes on durability is the increase in damage area for IM7/5260 specimens aged before impact. No influence was seen for IM7/K3B.

Degradation of the ply compressive strength dominates the aging effects on CAI strength. Physical aging, post-curing and stiffness changes are of second order importance. Further studies of the ply compressive strength of aged polymeric composites should be conducted to verify the data shown here. But the results of this study are conclusive.

## 8.2 CAI Strength

Results of CAI testing showed consistent decreases in strength from initial values with aging time. Degradation of IM7/5260 was temperature driven. At 149°C, CAI strength changes very little, while at 204°C the strength decreases 20% in only two months. CAI strength of IM7/K3B decreases for aging times up to six months, with little variation between specimens aged at different temperatures. After nine months of aging, the degradation of CAI strength proceeds at a slower rate. The temperature dependence is determined by the chemical reaction in the polymer, and should be investigated further for the K3B polyimide.

No changes were apparent in the damage size of IM7/K3B specimens impacted after aging. The bulk of the K3B polymer is unaffected by aging, and so the response to impact is the same for all specimens regardless of aging. IM7/5260 had large increases in the delamination size for aged material. The increases did not result in lower CAI strength however, because failure was dominated by the fiber damage around the impact point.

For specimens aged before impact, the change in CAI strength due to aging was less than for specimens impacted before aging. For the undamaged laminates of this study, the load bearing 0° plies were protected from oxidation until the degradation had grown through the outer 45° ply. After degradation reached the inner ply, the compressive strength decreased in a fashion similar to those specimens impacted before aging. The 0° ply began to degrade, and CAI strength decreased.

### 8.3 Compression Strength of Sandwich Panels

The structure used to build a production aircraft will be more complicated than the simple flat laminates studied. However, this research concludes that the effects of aging on sandwich or stiffened panels will be no different than for the simple geometry of a flat laminate. Residual stresses, expansion, stiffness changes, and all other variables dependent on structural configuration are of secondary importance. The basic ply property of compressive strength dominates the degradation. Predictions of the CAI strength of aged sandwich panels can be made directly using this research work.

## BIBLIOGRAPHY

- [1] Jones, R.M., Mechanics of Composite Materials, Hemisphere Publishing, New York, 1975.
- [2] Hoskin, B.C., Composite Materials for Aircraft Structure, AIAA, New York, 1984.
- [3] Poole, E.L., Lin, K.Y. and Backman, B.J, "Effects of aging on compressive strength of composites after impact," Proceedings of 35th SDM, Hilton Head SC, 1994.
- [4] Rosen, S.L., Fundamental Principles of Polymeric Materials, Wiley & Sons, New York, 1993.
- [5] Rodriguez, F., Principles of Polymer Systems, Hemisphere Publishing Corp., New York, 1989.
- [6] Koenig, J., Chemical Microstructure of Polymer Chains, John Wiley and Sons, New York, 1980.
- [7] Wilson, D., "Recent advances in polyimide composites," High Performance Polymers, Vol. 5, 1993, pp. 77-95.
- [8] DuPont, R-14800, Wilmington, Delaware, December 1990.
- [9] Dean, D., Miyase, A. and Geil, P.H., "The interaction of creep and physical aging in a semicrystalline thermoplastic matrix composite above  $T_g$ ," Journal of Thermoplastic Composite Materials, Vol. 5, April 1992, pp. 136-151.
- [10] Ma, C.M., Lee, C.L., Chang, M.J. and Tai, N.H., "Effect of physical aging on the toughness of carbon fiber-reinforced composites," Polymer Composites, Vol. 13, No. 6, 1992, pp.441-447.
- [11] Matsuoaka, S., Relaxation Phenomena in Polymers, Hanser Publishers, New York, 1992.
- [12] Sullivan, J.L., Blais, E.J. and Houston, D., "Physical aging in the creep behavior of thermosetting composites," Composites Science and Technology, Vol. 47, 1993, pp. 389-403.
- [13] Brinson, L.C. and Gates, T.S., "Effects of physical aging on long term creep of polymers and polymer matrix composites," International Journal of Solids and Structures, Vol. 32, No. 6, 1995, pp. 827-846.

- [14] Tuttle, M.E., Pasricha, A. and Emery, A.F., "The nonlinear viscoelastic-viscoplastic behavior of IM7/5260 composites subjected to cyclic loading," *Journal of Composite Materials*, Vol. 29, No. 15, 1995, pp. 2025-2046.
- [15] Boenig, H., Structure and Properties of Polymers, John Wiley and Sons, New York, 1973.
- [16] Cowie, J.M.G., Polymers: Chemistry & Physics of Modern Materials, Chapman and Hall, New York, 1991.
- [17] Boyd, J.D. and Chang, G.E., "Bismaleimide composite for advanced high-temperature applications," Presented at the 38th International SAMPE Symposium, May 10-13, Anaheim, CA, 1993.
- [18] Bowles, K.J., "Transverse flexural tests as a tool for assessing damage to PMR-15 composites from isothermal aging in air at elevated temperatures," *SAMPE Quarterly*, Vol. 24, No. 2, 1993, pp 49-53.
- [19] Mijovic, J., "Interplay of physical and chemical aging in graphite/epoxy composites," *Journal of Composite Materials*, Vol. 19, March 1985, pp. 178-191.
- [20] Hipp, R.C., Dow, M.B. et.al., "Thermal aging effects on candidate polymeric matrix composite materials for HSCT applications," McDonnell Douglas Aerospace, NASA Contract NAS1-18862.
- [21] Haskins, J.F., "Thermal aging," *SAMPE Journal*, Vol. 25, No. 2, Mar/April 1989, pp. 29-33.
- [22] Jayaraman, K., Reifsnider, K.L. and Swain, R.E., "Elastic and thermal effects in the interphase: Part I. Comments on characterization methods," *Journal of Composites Technology & Research*, Vol. 15, No. 1, Spring 1993, pp.3-13.
- [23] Nam, J.D. and Seferis, J.C., "Anisotropic thermo-oxidative stability of carbon fiber reinforced polymeric composites," *SAMPE Quarterly*, Vol. 24, No. 1, October 1992, pp. 10-18.
- [24] Skontorp, A., Wong, M.S. and Wang, S.S., "High-temperature anisotropic thermal oxidation of carbon-fiber reinforced polyimide composites," *Proceedings of ICCM-10*, Whistler, B.C., 1995.
- [25] Bowles, K.J., Jayne, D. and Leonhardt, T.A., "Isothermal aging effects on PMR-15 resin," *SAMPE Quarterly*, Vol. 24, January 1993, pp 2-9.

- [26] Salin, I.M., Seferis, J.C., Loechelt, C.L. and Rothschilds, R., "Time-temperature equivalence in thermogravimetry for BMI composites," SAMPE Quarterly, Vol. 24, No. 1, October 1992, pp. 54-63.
- [27] Hinkley, J.A. and Nelson, J.B., "Lifetime extrapolation of PMR-15 and LaRC-160 graphite composites," Journal of Advanced Materials, Vol. 25, No. 3, April 1994, pp45-48.
- [28] Shah, C.S., Patni, M.J. and Pandya, M.V., "Accelerated Aging and Life Time Prediction Analysis of Polymer Composites: a New Approach for a Realistic Prediction Using Cumulative Damage Theory," Polymer Testing, Vol. 13, No. 4, 1994, pp.295-320.
- [29] Miner, M.A., "Cumulative damage and fatigue," ASME Journal, Vol. 67, September 1945, p. A-159.
- [30] McManus, H.L., "Stress and Damage in Polymer Matrix Composite Materials Due to Material Degradation at High Temperatures," Proceedings of 35th SDM, Hilton Head, SC, 1994.
- [31] ASTM STP D5528-94A, "Standard test method for mode I interlaminar fracture toughness of unidirectional fiber-reinforced polymer matrix composites."
- [32] Martin, R.H., "Interlaminar fracture characterization: a current review," NASA CR 187573, 1991.
- [33] Slaton, D.B., " $G_{Ic}$  interlaminar fracture toughness of fiber-reinforced composites," Boeing Specification Support Standard 7273, Boeing Commercial Airplane Group, Seattle, October 1988.
- [34] Williams, J.G., "Large displacement and end block effects in the DCB interlaminar test in modes I and II," Journal of Composite Materials, Vol. 21, April 1987, pp. 330-347.
- [35] Kawada, H., Suguira, W., Miyao, K. and Hayashi, I., "Evaluation of mode I interlaminar fracture toughness in unidirectional GFRP at low temperature," Proceedings of ICCM-10, Whistler, B.C., 1995.
- [36] Poole, E.L. and Lin, K.Y., "Effects of isothermal aging on the toughness of polymeric composite materials," Proceedings of ICCM-10, Whistler BC, 1995.
- [37] Carpenter, S.A., Poole, E.L. and Lin, K.Y., "Surface degradation in graphite/polyimide composites at elevated temperature," Proceedings of 38th SDM, Orlando FL, 1997.

- [38] Seyler, Rickey J., ed. Assignment of the Glass Transition. ASTM, Baltimore, 1994.
- [39] Barr, T.L., Modern ESCA, CRC Press, Boca Raton, FL, 1994.
- [40] Beamson, G., and Briggs, D., High Resolution XPS of Organic Polymers, John Wiley & Sons, Chichester, 1992.
- [41] Shuart, M.J., "Failure of compression-loaded multidirectional composite laminates," *AIAA Journal*, Vol. 27, No. 9, 1989, pp. 1274-1279.
- [42] ASTM STP 790M-93, "Standard test method for flexural strength of advanced ceramics at ambient temperature."
- [43] Ghez, R., A primer of diffusion problems, Chapman and Hall, New York, 1985.
- [44] McManus, H.L. and Cunningham, R.A., "Coupled materials and mechanics analyses of durability tests for high temperature polymer matrix composites," to be published in an ASTM STP, 1996.
- [45] Finlayson, B.A., Numerical Methods for Problems with Moving Fronts, Ravenna Park Publishing, Seattle, 1992
- [46] Richards, L.A., "Capillary conduction of liquids in porous mediums", *Physics*, Vol. 1, 1931, pp. 318-333.
- [47] Warrick, A.W., "Numerical approximations of Darcian flow through unsaturated soil", *Water Resources* Vol. 27, No. 6, 1991, pp.1215-1222.
- [48] Miyazaki, T., Water Flow in Soils, Marcel Dekker, Hong Kong, 1993.
- [49] Holsapple, K.A., MacFRED finite element code, Department of Aeronautics and Astronautics, University of Washington.
- [50] Zienkiewicz, O.C. and Taylor, R.L., The Finite Element Method, Vol. 12, McGraw Hill, London, 1991.
- [51] Bickford, W.B., A First Course in the Finite Element Method, Irwin, Boston, 1990.
- [52] ACEE Composite Project Office, "Standard tests for toughened resin composites," RP-1092, NASA-LARC, Hampton, 1983.

- [53] Grande, D. H., "Advanced composite compression tests," Boeing Specification Support Standard 7260, Boeing Commercial Airplane Group, Seattle, December 1988.
- [54] ASTM STP D3878-87A, "Standard test method for compressive properties of unidirectional or crossply fiber-resin composites."
- [55] Jackson, W.C. and Poe, C.C. Jr., "The use of impact force as a scale parameter for the impact response of composite laminates," *Journal of Composites Technology & Research*, Vol. 15, 1993, pp. 282-289.
- [56] Clark, G., "Modelling of impact damage in composite laminates," *Composites*, Vol. 20, No. 3, May 1989, pp. 209-214.
- [57] Davies, G., Zhang, X., Zhou, G. and Watson, S., "Numerical modelling of impact damage," *Composites*, Vol. 25, No. 5, 1994, pp. 342-350.
- [58] Kwon, Y.S. and Sankar, B.V., "Indentation-flexure and low-velocity impact damage in graphite epoxy laminates," *Journal of Composites Technology & Research*, Vol. 15, No. 2, 1993, pp. 101-111.
- [59] Cairns, D.S. and Lagace, P.A., "Transient response of graphite/epoxy and Kevlar/epoxy laminates subjected to impact," *AIAA Journal*, Vol. 27, No. 11, May 1988, pp. 1590-1596.
- [60] Wu, H.T. and Springer, G.S., "Impact induced stresses, strains, and delaminations in composite plates," *Journal of Composite Materials*, Vol. 22, June 1988, pp. 533-560.
- [61] Dorey, G., "Relationship between impact resistance and fracture toughness in advanced composite materials," *Effect of Service Environment on Composite Materials*, AGARD CP 288, 1980.
- [62] Gosse, J.H. and Mori, P.B.Y., "Impact Damage Characterization of Graphite/Epoxy Laminates," *Proceedings of 3rd Technical Conference of American Society for Composites*, Seattle WA, 1988.
- [63] Wu, H.T. and Springer, G.S., "Measurements of matrix cracking and delamination caused by impact on composite plates," *Journal of Composite Materials*, Vol 22, June 1988, pp. 518-532.
- [64] Dan-Jumbo, E., Leewood, A.R. and Sun, C.T., "Impact damage characteristics of bismaleimides and thermoplastic composite laminates," *ASTM STP 1012*, 1989, pp. 356-372.

- [65] Hon, S. and Liu, D., "On the relationship between impact energy and delamination area," *Experimental Mechanics*, Vol. 13, 1989, pp. 115-120.
- [66] Cantwell, W.J. and Morton, J., "The impact resistance of composite materials - a review," *Composites*, Vol. 22, No. 5, September 1991, pp. 347-362.
- [67] Jegley, D.C., "Effect of low-speed impact damage and damage location on behavior of composite panels," TP-3196, NASA-LARC, Hampton, May 1992.
- [68] Bibo, G., Leicy, D., Hogg, P.J. and Kemp, M., "High-temperature damage tolerance of carbon fibre-reinforced plastics, Part 1: Impact characteristics," *Composites*, Vol. 25, No. 6, 1994, pp.414-424.
- [69] Chai, H. and Babcock, C.D., "Two-dimensional modelling of compressive failure in delaminated laminates," *Journal of Composite Materials*, Vol. 19, January 1984, pp. 67-98.
- [70] Shivakumar, K.N. and Whitcomb, J.D., "Buckling of a sublaminar in a quasi-isotropic composite laminate," *Journal of Composite Materials*, Vol. 19, January 1985, pp. 2-18.
- [71] Whitcomb, J. D. and Shivakumar, K. N., "Strain-energy release rate analysis of plates with postbuckled delaminations," *Journal of Composite Materials*, Vol. 23, July 1989, pp. 714-734.
- [72] Whitcomb, J.D., "Three-dimensional analysis of a postbuckled embedded delamination," *Journal of Composite Materials*, Vol. 23, September 1989, pp. 862-889.
- [73] Kassapoglou, C., "Buckling, post-buckling and failure of elliptical delaminations in laminates under compression," *Composite Structures*, No. 9, 1988, pp. 139-159.
- [74] Donaldson, S.L., "The effect of interlaminar fracture properties on the delamination buckling of composite laminates," *Composites Science and Technology*, Vol. 28, 1987, p. 33.
- [75] Shibaoka, Y., "On the buckling of an elliptic plate with clamped edge," *Journal of the Physical Society of Japan*, Vol. 11, No. 10, October, 1956, pp. 1088-1091.
- [76] Yin, W.L. and Jane, K.C., "Refined buckling and postbuckling analysis of two-dimensional delaminations," *International Journal of Solids and Structures*, Vol. 29, No. 5, 1992, pp. 591-610.

- [77] Barbero, E.J. and Reddy, J.N., "Modeling of delamination in composite laminates using a layer-wise plate theory," *International Journal of Solids and Structures*, Vol. 28, 1991, pp.373-388.
- [78] Gu, H. and Chattopadhyay, A., "A new higher-order plate theory in modeling delamination buckling of composite laminates," *Proceedings of 35th SDM*, Hilton Head, SC, 1994.
- [79] Cairns, D.S., Minguet, P.J. and Abdallah, M.G., "The influence of size and location on the response of composite structures with delaminations loaded in compression," *Proceedings of 35th SDM*, Hilton Head, SC, 1994.
- [80] Yin, W.L., "The effects of laminated structure on delamination buckling and growth," *Journal of Composite Materials*, Vol. 22, June 1988, pp.502-517.
- [81] Yin, W.L., Sallam, S.N. and Simitzes, G.J., "Ultimate axial load capacity of a delaminated beam-plate," *AIAA Journal*, Vol. 24, No. 1, January 1986, pp. 123-128.
- [82] Shu, D. and Mai, Y.W., "Buckling of delaminated composites re-examined," *Composites Science and Technology*, Vol. 47, 1993, pp. 35-41.
- [83] Kutlu, Z. and Chang, F.K., "Modeling compression failure of laminated composites containing multiple through-the-width delaminations," *Journal of Composite Materials*, Vol. 26, No. 3, 1992, pp. 350-387.
- [84] Guild, F.J., Hogg, P.J. and Prichard, J.C., "A model for the reduction in compression strength of continuous fibre composites after impact damage," *Composites*, Vol. 24, No. 4, 1993, pp. 333-339.
- [85] Ilcewicz, L.B., Dost, E.F. and Coggeshall, R.L. "A model for compression after impact strength evaluation," *Proceedings of the 21st International SAMPE Technical Conference*, 1989.
- [86] Dost, E.F., Ilcewicz, L.B. and Gosse, J.H., "Sublaminar stability based modeling of impact-damaged composite laminates," *Proceedings of 3rd Technical Conference of American Society for Composites*, Seattle WA, 1988.
- [87] Lin, K.Y. and Li, R., "Post impact compressive behavior of composites," *Proceedings of the 18th Congress of International Council of the Aeronautical Science*, Beijing China, 1992.

- [88] Allix, O. and Ladeveze, P., "Interlaminar interface modelling for the prediction of delamination," *Composite Structures*, Vol. 22, 1992, pp. 235-242.
- [89] Flanagan, G., "A general sublaminar analysis method for determining strain energy release rates in composites," *Proceedings of 35th SDM, Hilton Head, SC, 1994*.
- [90] Zhang, J., Soutis, C. and Fau, J. , "Strain energy release rate associated with local delamination in cracked composite laminates," *Composites*, Vol 25, No 9, 1994, p. 851.
- [91] Tan, S.C., Stress Concentration in Laminated Composites, Technomic Publishing Company, Lancaster, 1974.
- [92] Shuart, M.J., "Short-wavelength buckling and shear failures for compression-loaded composite laminates," *NASA TM-87640*, 1985.
- [93] Stevens, J. J., "Characterization of post-impact compressive behavior of composite laminates", M. S. Thesis, Department of Aeronautics and Astronautics, University of Washington, 1992
- [94] Post, D., "Moiré Interferometry," from *Handbook on Experimental Mechanics*, Prentice Hall, New Jersey, 1987
- [95] Post, D., "Optical interference for deformation measurements-classical, holographic and moiré interferometry," Mechanics of Nondestructive Testing, ed. Stinchcomb, W.W, New York: Plenum Press, 1980, pp. 1-53.
- [96] Klein, R.J. and Tuttle, M.E., "Strain measurements in composites subjected to compressive loading using moiré interferometry," *NASA-CR 62-7541*, April 1987.
- [97] Graesser, D. L., "Compression creep of filamentary composites," M. S. thesis, University of Washington, 1988.
- [98] Hamling, S.J., "Prediction of the compressive strength of composite sandwich panels with impact damage", M. S. Thesis, Department of Aeronautics and Astronautics, University of Washington, 1994
- [99] Parks, V.J., "Geometric Moiré," Handbook on Experimental Mechanics, Prentice Hall, New Jersey, 1987

## Appendix A

### SHADOW MOIRÉ

Shadow moiré is a type of geometric moiré, which utilizes the superposition of two grid patterns to form a third pattern. Parks presents a thorough description of the technique in [99], and a brief description is given here. The grid pattern consists of dark parallel lines, equally spaced. The distance between two lines is referred to as the pitch, and generally symbolized by  $g$ . One grid pattern, referred to as the specimen grating, is attached to the flat surface of the specimen to be analyzed. A similar grid pattern, referred to as the reference pattern, is held directly above the specimen grating. If the two gratings have the same pitch, then the specimen can be aligned so that the lines of one grating exactly cover the spaces of the other grating. The viewer sees a uniform dark field, or a null field.

During loading, the specimen surface moves relative to the reference grating. If the surface moves a distance  $g$ , the gratings will again align to form a dark field. If the surface moves a half integer of  $g$ , then the viewer will see a light field. The result is a series of light and dark bands. The dark bands are referred to as fringes. Each fringe represents a displacement of  $g$  relative to any neighboring fringe. The displacements are only in the direction perpendicular to the grating lines. Any movement parallel to these lines is undetected.

Shadow moiré measures out-of-plane displacements. A reference grating is placed just above the surface of the specimen. A light source is positioned with an angle  $\alpha$  relative to the viewer, as shown in Figure A.1. The light travels through the reference grating, reflects off of the specimen, and then passes through the grating again. The distance between the path of a beam of light traveling into and away from the reference grating is designated by  $e$ . This distance is equivalent to the in-plane displacement

described for geometric moiré. Varying  $e$  produces fringe patterns in the same way as for other types of geometric moiré.

The distance  $e$  is related to the out-of-plane displacement,  $z$ , by the geometric equation

$$\tan\alpha = \frac{e}{z}$$

Where  $z$  is the distance between the reference grating and the specimen surface. Since the total displacement in a moiré fringe pattern is simply equal to the pitch multiplied by the number of fringes,  $N$ , the distance  $z$  can be calculated from the fringe pattern by

$$z = \frac{gN}{\tan\alpha}$$

To prepare specimens for shadow moiré testing, the back surface is painted with a thin coating of reflective paint. Rather than calculate fringe gradients using the equation above, a calibration technique was used for each specimen. A reference cone was bonded to the surface, which had a known difference in height from the edge to the center peak. By counting the number of fringes appearing on this cone in the shadow moiré image, the out-of-plane displacement per fringe was determined. After the specimen was placed in the test fixture, a transparent grating of 100 lines per inch was placed just above the surface of the specimen. A point light source illuminated the specimen, and a camera was positioned to capture the image. Looking through the camera lens, the orientation of the grating was adjusted so that a null field was seen on the surface at zero load.

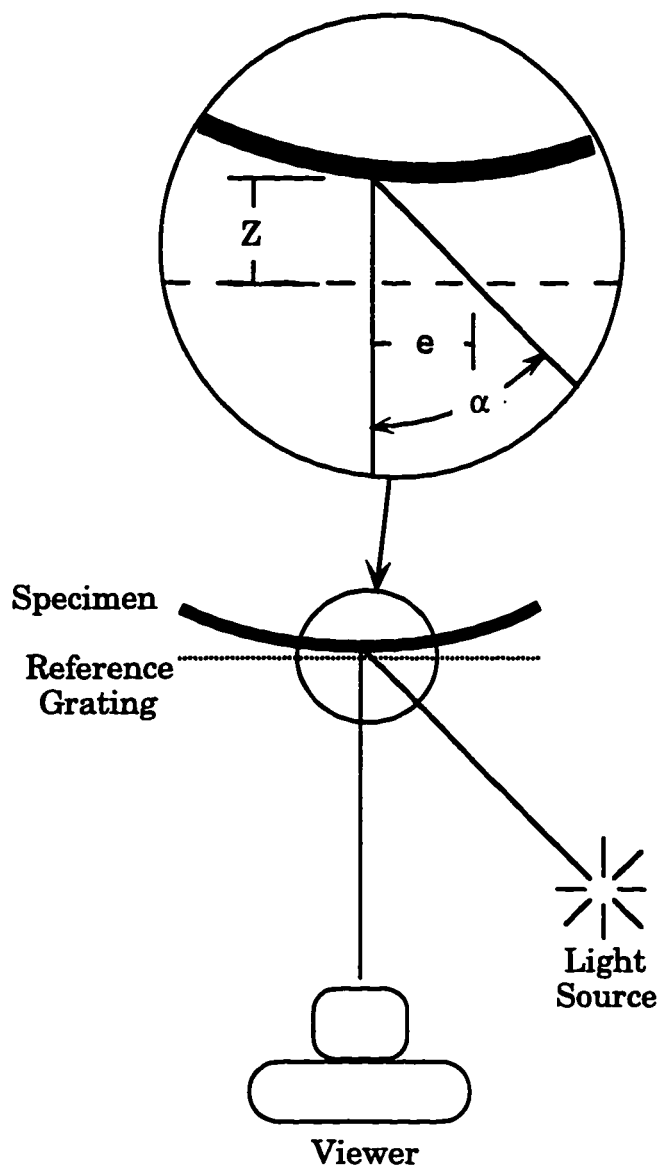


Figure A.1 Diagram of shadow moiré

## Appendix B

# MOIRE INTERFEROMETRY

### B.1 Theoretical background

In order to understand moiré interferometry, the interference pattern produced by intersecting beams of light must first be understood. The wave theory of light provides an explanation of the phenomenon. At some point a fixed distance away from a light source the strength of the wave disturbance is

$$A = a \cos^2 \pi \omega t \quad (\text{B-1})$$

where  $\omega$  is the frequency in cycles per second, equivalent to the speed of light divided by the wavelength of the light beam, and  $a$  is a constant. If the beam is collimated, the plane cross sections of the wave disturbance will have a constant strength. That is, the field strength at a fixed point in time will only vary with  $z$ , the distance from the light source.

When visible light travels through air, it has a frequency of approximately  $6 \times 10^{14}$  Hz. At this frequency, the oscillations are too quick to be detected by receivers such as photographic equipment or the human eye. Instead, it is the intensity of energy absorbed, averaged over time, that is measured. Electromagnetic theory shows that for light of the amplitude given in equation B-1, the intensity of the light wave is

$$I = a^2 \quad (\text{B-2})$$

and thus we have a measure of the wave disturbance strength that is independent of frequency and time.

Interference occurs when two beams with different phases overlap. Given two beams of equal intensity, shifted a distance  $S$  in phase, one beam can be described as having strength  $A_1$  as given in equation B-1, and the second beam will have a strength given by

$$A_2 = a \cos 2\pi(\omega t + S/\lambda) \quad (\text{B-3})$$

where  $\lambda$  is the wavelength of the beam. The intensity of the combined beams will be

$$I = 2a^2 (1 + \cos 2\pi S/\lambda) = 4a^2 \cos^2 \pi S/\lambda \quad (\text{B-4})$$

which is a fundamental relationship known as the intensity distribution for pure two beam interference. When the two beams are out of phase by an integer multiple of the wavelength,  $S/\lambda = 0, 1, 2, 3 \dots$ , then the intensity is a maximum and constructive interference occurs. If  $S/\lambda = 1/2, 3/2, 5/2 \dots$ , then the intensity is a minimum and destructive interference occurs. Even if the interference is impure, that is, the intensities of the interfering beams are not equivalent, the resulting interference patterns will still be quite strong. When the intensity of the two input beams differs by a factor of two, the difference in peak constructive and peak destructive interference is still an order of magnitude [95].

Fringe patterns are generated by two beams of light intersecting at an angle. Figure B.1 shows the intersecting region of two wave fronts with a relative angle of  $2\theta$ .  $A_1$  represents the amplitude of the light disturbance strength of the first wave train and  $A_2$  is the strength of the second wave train. Both waves have the same wavelength.

At point a in the fringe field, the two wave trains have the same amplitude. The phase difference is an integer multiple of the wavelength, and so constructive interference occurs. Since both waves travel with the same velocity and wavelength, the disturbance strength of both waves will be equal for all time, and this produces steady constructive interference. The same argument holds true for every point along the line a-b. At point c, the wave disturbance strength of the two beams is out of phase by an integer multiple of the wavelength, plus one half wavelength. This produces destructive interference. As with the constructive interference, the destructive interference is steady state, and exists on every point along c-d.

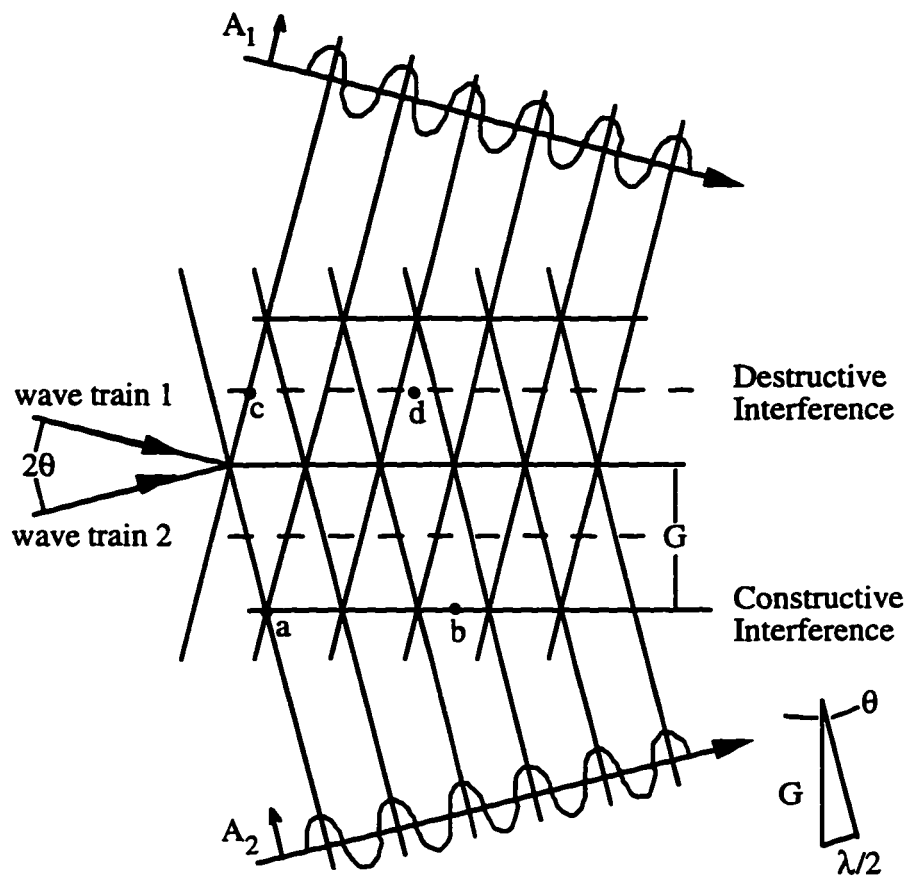


Figure B.1 Regions of constructive and destructive interference in space where two coherent beams intersect [94]

Extending these arguments to the full field of the intersecting beams, a series of constructive and destructive interference bands is generated. The intensity of the resultant light beam is a grid of bright bands, spaced a distance  $G$  apart. From the geometry of the figure,  $G$  is related to  $\theta$  by

$$\sin \theta = \frac{\lambda / 2}{G} \quad (\text{B-5})$$

which is used to find the frequency of the fringes, or fringe gradient. Fringe gradient is simply the inverse of  $G$ , and so the calculation is

$$F = 1/G = \frac{2}{\lambda} \sin \theta \quad (\text{B-6})$$

Since the wave trains are planes, the interference bands shown in Figure B.1 will be lines extending perpendicular to the plane of the paper. Such a pattern of light and dark bands is called a virtual grating.

The moiré interferometry method uses virtual and specimen gratings to create a pattern of two beam interference. This fringe pattern can be photographed, and then strains can be calculated by counting fringes. Figure B.2 shows a schematic diagram of an interferometer, and a general explanation follows.

The specimen grating is mounted on the surface of the specimen so that the grating will deform with the specimen during loading. A virtual grating is created at the surface of the specimen by two beams of intersecting light, A and B, as described above. The light waves both have a frequency of  $\lambda$ , and incidence angles of  $\alpha$  and  $-\alpha$ , respectively. The frequency of the virtual grating is governed by equation (B-6). The frequency of the specimen grating,  $f$ , is chosen to be one half the frequency of the virtual grating.

The beams emergent from the specimen grating are governed by the two-dimensional grating equation

$$\sin \beta_m = \sin (-\alpha) + m\lambda F/2 \quad (\text{B-7})$$

where  $m$  is the diffraction order of the beam. If no loading is applied to the specimen, the angle of emergent beam A' corresponds to the first order diffraction angle  $\beta_1$ . Substituting equation (B-6) into (B-7) shows the emergent angle to be zero. Likewise for emergent beam B', the angle is zero. The two coherent beams intersect with an angle difference of zero, and a uniform intensity field is produced.

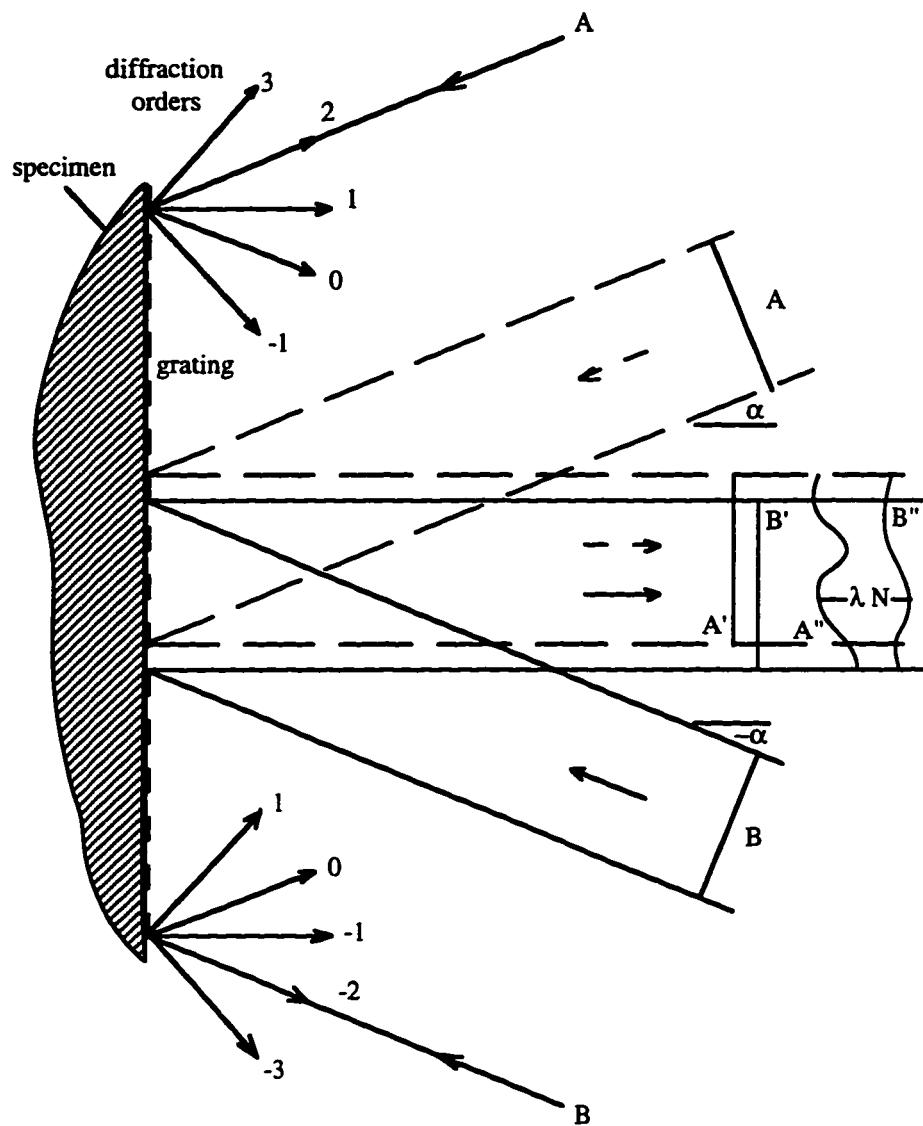


Figure B.2 Two beam interference resulting from diffraction of incident beams which produces the moiré image

When the specimen is deformed by a strain  $\epsilon$ , the grating frequency changes to

$$f = \frac{F/2}{1+\epsilon} \quad (\text{B-8})$$

Using this equation angle  $\beta_1$ , the emergent angle of beam A", will be

$$\beta_1 = -\frac{\lambda F \epsilon}{2} \quad (\text{B-9})$$

assuming  $\beta_1$  is a small angle and  $\epsilon \ll 1$ . Similarly, the emergent angle of B" will be

$$\beta_{-1} = \frac{\lambda F \epsilon}{2} \quad (\text{B-10})$$

Therefore, the emergent beams A" and B" have an angular separation of  $2\beta_1$ . A fringe pattern is formed, again governed by equation (B-6). Since the angle  $\beta$  is small,  $\sin \theta = \beta_1$  can be substituted into equation (B-6) to give

$$f = F\epsilon \quad (\text{B-11})$$

The frequency of the virtual reference grating,  $F$ , remains constant throughout the experiment, and so strain is directly proportional to the fringe gradient. Fringe gradient is simply  $\partial N/\partial x$ , where  $N$  is the fringe order, and so this value can be found from the density of the fringes in the moiré image.

## B.2 Experimental procedure

The general procedure for fabricating high frequency interferometric gratings is to form a mold, coat the mold with a thin metallic film, and then transfer the thin film to the specimen. To form the mold, a high resolution photographic plate, which is simply a glass plate coated with a photographic emulsion, is exposed to the interference pattern generated by two intersecting light waves. When the plate is developed, silver crystals

will form in the gelatin emulsion in regions exposed to constructive interference, while regions exposed to destructive interference remain clear. During drying, the gelatin shrinks much more in the clear regions, and so the surface of the dried gelatin is sinusoidal. The surface is then coated with a thin (60 nm) aluminum coating using vacuum deposition. The steps of this procedure are shown in Figure B.3. The gratings used in this research had a frequency of 600 lines/mm.

Once the grating is formed on the surface of the mold, it must be transferred to the specimen. First, it is important to have a very clean, smooth, specimen surface. Any grease or dirt on the surface results in a bad bond between the specimen and the grating, and the test data will be adversely effected. The surface must be smooth so that pockets of the epoxy adhesive do not form under the grating. This is because a thick region of epoxy could have strain gradients through the thickness, and therefore the strains measured by the grating would be different than the strains of the specimen surface.

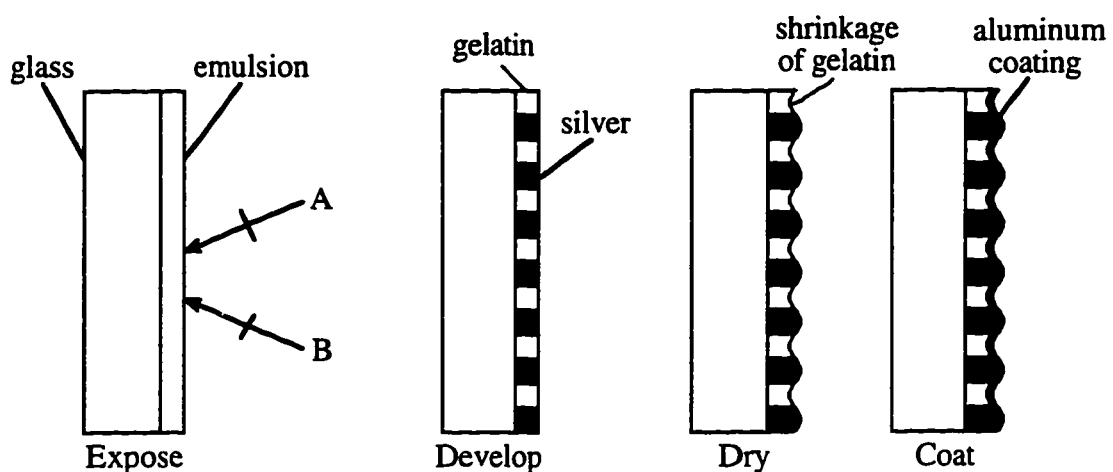


Figure B.3 Optical generation of a mold for producing specimen gratings [94]

An epoxy resin was used to fix the grating to the specimen surface. The resin and hardener were mixed, and then spun in a centrifuge to remove air bubbles. The epoxy was spread on the cleaned specimen, and the grating was slowly lowered onto the epoxy, being careful not to trap air beneath the grating. Once the grating had been positioned, it was pressed firmly onto the specimen. When all possible epoxy had been removed from between the specimen and grating, a weight was placed on top of the glass plate, clamped into place, and left overnight. A razor blade was used after this drying period to pry the glass plate away from the grating. Care was taken not to touch the exposed grating until after testing was complete. Figure B.4 shows the steps of this process.

For this research, an 8 mirror system was used to capture both vertical displacement,  $u$ , and horizontal displacement,  $v$ . The light source was a 35mW He-Ne laser, and a diagram of the set up is shown in Figure B.5. Before beginning the test, the mirrors and lenses were adjusted until the image in the camera lens showed a clean null displacement field. Then the compression testing procedure was followed as given in Section 6.1, except that the loading was halted at specific increments. While the loading was stopped, photographs of all three displacement fields were taken, and the loading was recorded. The load level increment was decreased as failure was approached, in order to provide greater detail of the critical loading near failure. After failure, one more picture was taken.

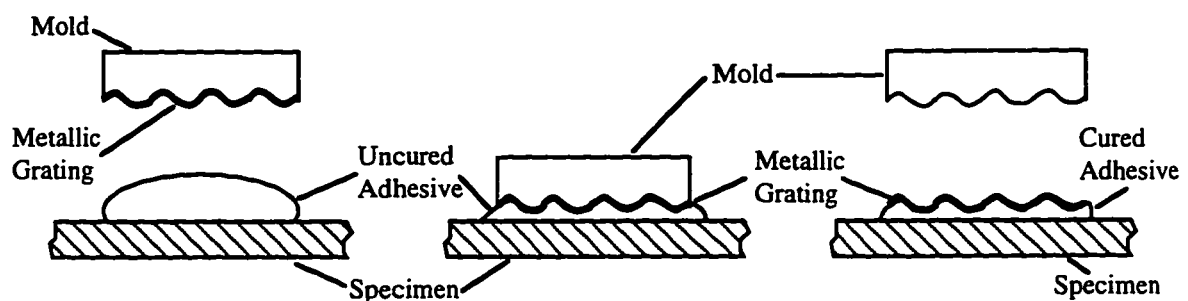


Figure B.4 Steps in transferring the thin metallic grating to the specimen surface [94]

The photographs could then be processed by computer scanning and data processing to produce strain field maps of the damage area under compressive stress. John Stevens performed this type of image processing in his Masters thesis [93]. A full description of the procedure is given in Stevens' thesis, but a brief description is included here.

The displacement fringe pattern image was photographed, and the developed negative was scanned into a personal computer at 1600 dpi. This computerized image was in gray scale mode, and contained large amounts of noise. A bitmap, black and white image with clearly defined fringes is necessary for the computer routines used to calculate the strain field, and so enhancement of the scanned images was necessary. Contrast and brightness were adjusted to provide greater distinction between fringes, and various filters were used to clarify and smooth the fringes. The reference line was measured to provide an accurate dimensional scale factor. Finally, the gray scale image was converted to bitmap black and white. Any remaining noise was removed pixel by pixel. A program developed by Doug Graesser [97] was then used to calculate strain data from the bitmap of the moiré fringe patterns. This data was then converted into color map using imaging software. The original moiré image and the calculated strain field image are shown in Figure B.6.

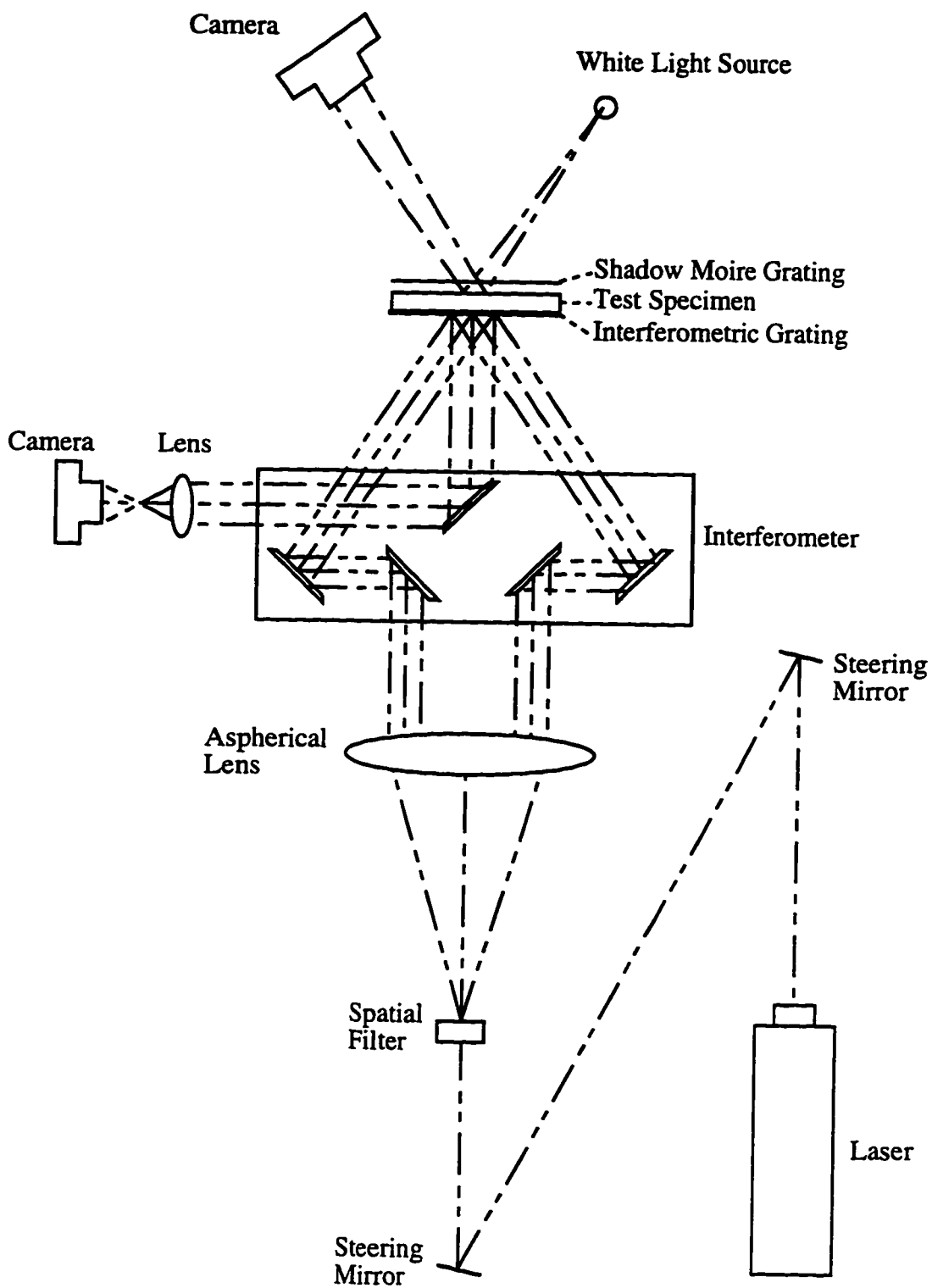


Figure B.5 Positioning of optical equipment used for moiré measurement of in-plane and out-of-plane displacement fields

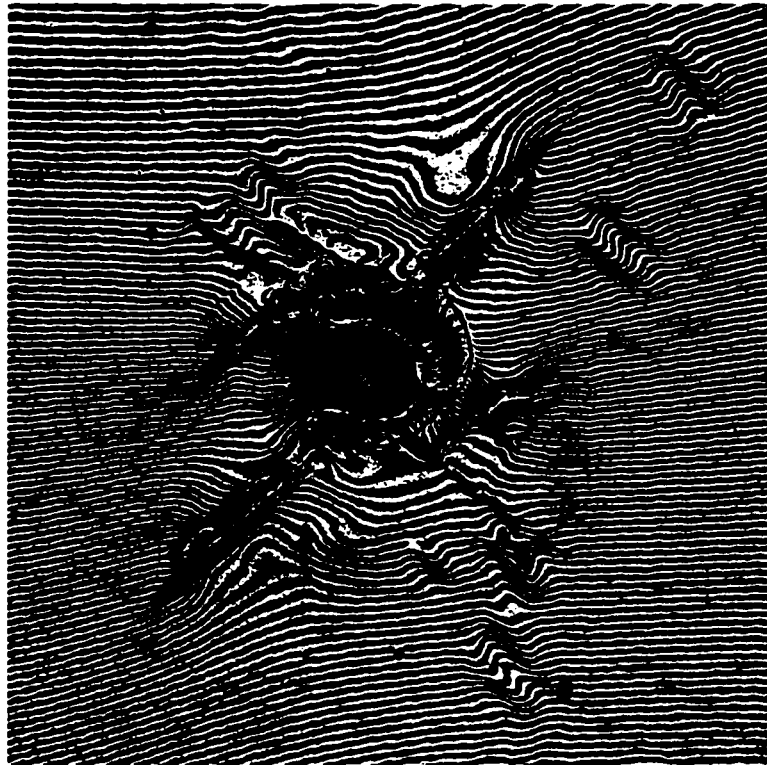


Figure B.6 Displacement fringes and the resulting strain field

## Appendix C

### FINITE ELEMENT SUBROUTINES

#### C.1 One dimensional degradation

```
c*****
c*****
c
  subroutine degrade(d,ul,xl,ix,tl,s,p,ndf,ndm,nst,isw,ql)
c
c one dimensional nonlinear diffusion/reaction element
c uses equations for flow through a porous media, the soil problem
c
c implicit double precision (a-h, o-z)
  common/input/in,io
  common/cdata/head,numnp,numel,nummat,nen,neq,ipr,ipd,itfl
  common/eldata/dm,nn,ma,mct,iel,nel
  character*4 prbwd,code
  character*80 head
  dimension d(1),ul(1),xl(ndm,1),ix(nen+1,1),tl(1),s(nst,1),p(1)
  $      ,shp1(2,3),sg(2),wg(2),sig(3),eps(3),ql(nen,1)
  $      ,dsdp(3),sat(3),diff(3)
  save
c go to correct array processor
  issw=isw
  if(isw.eq.9) issw=7
  goto(1,2,3,4,5,3,3) issw
c read in material data
  1 read(in,*) d(1),d(3),d(4),d(7),d(8)
  write(io,1000) d(1),d(3),d(4),d(7),d(8)
  if(io.ne.9) write(9,1000) d(1),d(3),d(4),d(7),d(8)
  iprin=0
  d(5)=d(4)*d(3)
  d(6)=d(4)-1
  return
c check the mesh
  2 call ckisop(ix,xl,shp,ndm)
  return
c compute the stiffness matrix
  3 l=nel-1
c get gauss points, if necessary
  if(l.ne.lint.and.l.eq.2) call gaus1d(l,lint,sg,wg)
c first zero s and calculate length
  do 310 i=1,nst
```

```

do 310 j=1,nst
310 s(i,j)=0.
xlen=0.
do 320 i=1,ndm
320 xlen=xlen+(xl(i,2)-xl(i,1))**2
xlen=2*(xlen**0.5)/d(1)
do 330 i=1,nel
diff(i)=1/((1+d(3)*(d(7)-ul(i))**d(4))**d(8))
330 dsdp(i)=d(5)*(d(7)-ul(i))**d(6)/((1+d(3)*(d(7)-ul(i))**d(4))**2)
c time step estimate, equals zero at t=0
if(issw.eq.7) then
d(18)=(xlen**2)*0.125*(dsdp(1)+dsdp(2))
return
endif
c direct calculation for two noded element
if(nel.eq.2) then
s(1,1)=(diff(1)+diff(2))*dm/xlen
s(1,2)=-s(1,1)
s(2,2)=s(1,1)
s(2,1)=s(1,2)
else
30 do 300 l=1,2
call shpbar(sg(1),xl,shp1,xsj,ndm,nel,.false.)
c check jacobian determinant
if(xsj.le.0) then
prbwd=code(nn)
call ShowAlert(3,'**Fatal Error: Element '//prbwd//
$ ' has a negative or zero jacobian! Check it out.**')
call stopit
endif
c assemble stiffness from integrals and material properties
xsj=xsj*wg(1)*d(1)*abs(dm)
do 300 j=1,3
dnx=shp1(1,j)*xsj
do 300 k=1,3
dndn=dnx*shp1(1,k)
do 300 i=1,3
300 s(j,k)=s(j,k)+dndn*shp1(3,i)*diff(i)
endif
c calculate the force matrix
if(isw.eq.6) then
do 360 j=1,nel
do 360 k=1,nel
360 p(j)=p(j)-s(j,k)*ul(k)
endif
return
c calculate coordinates, gradients, fluxes, and forces

```

```

4 xlen=0.
  do 420 i=1,ndm
420 xlen=xlen+(xl(i,2)-xl(i,1))**2
    xlen=xlen**0.5
    do 430 i=1,nel
430 sat(i)=1/(1+d(3)*(d(7)-ul(i))**d(4))
      if (nel.eq.2) then
        eps(1)=(ul(2)-ul(1))/xlen
        sig(1)=-eps(1)*d(1)
        eps(2)=(sat(2)-sat(1))/xlen
        sig(2)=-eps(2)*d(1)
      else
        alph=0.
        do 440 i=1,ndm
440  alph=alph+(xl(i,3)-xl(i,1))**2
          alph=alph**0.5/xlen
          eps(1)=(-1.5*ul(1)-0.5*ul(2)+2*ul(3))/(2*alph-0.5)/xlen
          eps(2)=(0.5*ul(1)+1.5*ul(2)-2*ul(3))/(-2*alph+1.5)/xlen
          eps(3)=(ul(2)-ul(1))/xlen
          sig(1)=-d(1)*eps(1)
          sig(2)=-d(1)*eps(2)
          sig(3)=-d(1)*eps(3)
        endif
c nodal stresses loaded into ql array
        do 460 i=1,3
460 ql(i,1)=sig(i)
        return
c put consistent mass in s, lumped mass in p
5 xlen=0.
    do 520 i=1,ndm
520 xlen=xlen+(xl(i,2)-xl(i,1))**2
      xlen=dm*(xlen**0.5)
      xmas=xlen/300
      do 530 i=1,nel
        p(i)=0.0
        dsdp(i)=d(5)*(d(7)-ul(i))**d(6)/((1+d(3)*(d(7)-ul(i))**d(4))**2)
        do 530 j=1,nel
530 s(i,j)=0.0
          if(nel.eq.3) then
            alph=0.0
            do 550 i=1,ndm
550  alph=alph+(xl(i,3)-xl(i,1))**2
              alph=(alph**0.5)/xlen
              s(1,1)=xmas*((84*alph-15)*dsdp(1)+(3-12*alph)*dsdp(2)
                $      +(48*alph-8)*dsdp(3))
              s(2,1)=xmas*((3-12*alph)*dsdp(1)+(12*alph-9)*dsdp(2)-4*dsdp(3))
              s(3,1)=xmas*((48*alph-7)*dsdp(1)-5*dsdp(2)+(32*alph-8)*dsdp(3))
            endif
          endif
        enddo
      enddo
    enddo
  enddo

```

```

    s(2,2)=xmas*((12*alph-9)*dsdp(1)+(69-84*alph)*dsdp(2)
$   +54*dsdp(3))
    s(3,2)=xmas*4*(-dsdp(1)+(10-12*alph)*dsdp(2)
$   +(6-8*alph)*dsdp(3))
560 s(3,3)=xmas*8*((12*alph-3)*dsdp(1)+(9-12*alph)*dsdp(2)
$   +(40-48*alph)*dsdp(3))/3
    s(1,2)=s(2,1)
    s(1,3)=s(3,1)
    s(2,3)=s(3,2)
    else
    s(1,1)=xlen*(dsdp(1)+dsdp(2))/3)/4
    s(2,1)=xlen*(dsdp(1)+dsdp(2))/12
    s(2,2)=xlen*(dsdp(1)/3+dsdp(2))/4
    s(1,2)=s(2,1)
    endif
    do 580 i=1,nel
    do 580 j=1,nel
580 p(i)=p(i)+s(i,j)
    return
c.... formats
1000 format(/5x,//
$ 10x,'      diffusion      ',2x,e14.6/
$ 10x,'      alpha        ',2x,e14.6/
$ 10x,'      n            ',2x,e14.6/
$ 10x,'      shift         ',2x,e14.6/
$ 10x,'      lamda         ',2x,e14.6/)
end

```

## C.2 Two dimensional degradation

```

c*****
c*****
c
c   subroutine degrade(d,ul,xl,ix,tl,s,p,ndf,ndm,nst,isw,ql)
c
c nonlinear diffusion for orthotropic materials
c uses equations for flow through a porous media, the soil problem
c no convection terms, 2-d, cartesian coordinates
c
c implicit double precision (a-h, o-z)
common/input/in,io
common/cdata/head,numnp,numel,nummat,nen,neq,ipr,ipd,itfl
common/eldata/dm,nn,ma,mct,iel,nel
common/tr/tr51(1,5),tr64(4,6),tr84(4,9),tr88(8,8)
character*4 prbwd,code
character*80 head

```

```

dimension d(1),ul(1),xl(ndm,1),ix(nen+1,1),tl(1),s(nst,1),p(1),
$ shp(3,9),sg(9),tg(9),wg(9),sig(4),eps(4),ql(nen,1),lchec(2),
$ dsdp(9),sat(9),diff(9)
save
data lchec/-1,-4/
c go to correct array processor
issw=isw
if(isw.eq.9) issw=7
goto(1,2,3,4,5,3,7) issw
c read in material data
1 read(in,*) d(1),d(2),d(3),d(4),d(7),d(8)
write(io,1000) d(1),d(2),d(3),d(4),d(7),d(8)
if(io.ne.9) write(9,1000) d(1),d(2),d(3),d(4),d(7),d(8)
iprin=0
d(5)=d(3)*d(4)
d(6)=d(4)-1
return
c check the mesh
2 call ckisop(ix,xl,shp,ndm)
return
c compute the stiffness matrix
3 l=1
if(nel.ge.4) l=2
if(nel.ge.7) l=3
c get gauss points, if necessary
if(dm.lt.0) then
if(lint.gt.0.or.lint.ne.lchec(1)) call gaustri(l,lint,sg,tg,wg)
else
if(lint.lt.0.or.lint.ne.l*1) call gaus2d(l,lint,sg,tg,wg)
endif
do 330 i=1,nel
330 diff(i)=1/((1+d(3))*(d(7)-ul(i))**d(4))**d(8))
c loop over all gauss points
30 do 300 l=1,abs(lint)
if(dm.gt.0) then
call shape(sg(l),tg(l),xl,shp,xsj,ndm,nel,ix,.false.)
else
call shptri(sg(l),tg(l),xl,shp,xsj,ndm,nel,ix,.false.)
endif
c check jacobian determinant
if(xsj.gt.0) goto 34
if(xsj.eq.0) then
prbwd=code(nn)
call ShowAlert(3,'**Fatal Error: Element '//prbwd//
$ ' has a zero jacobian! Check it out.**')
call stopit
else

```

```

        if(xsj.lt.0.and.l.eq.1) then
            do 340 i=1,nel
340      xl(2,i)=-xl(2,i)
            goto 30
            else
                prbwd=code(nn)
                call ShowAlert(3,'**Fatal Error: Element '//prbwd//'has a ch
$ange of sign of its jacobian in its interior! Check it out.**')
                call stopit
            endif
        endif
c assemble stiffness from integrals and material properties
34 xsj=xsj*wg(1)*abs(dm)
    do 300 j=1,nel
        dnx=d(1)*shp(1,j)*xsj
        dny=d(2)*shp(2,j)*xsj
        do 300 k=1,nel
            dnnx=dnx*shp(1,k)
            dnnny=dny*shp(2,k)
            do 300 i=1,nel
300      s(j,k)=s(j,k)+(dnnx*shp(3,k)+dnnny*shp(3,k))*diff(i)
c calculate the force matrix
        do 360 j=1,nel
            do 360 k=1,nel
360      p(j)=p(j)-s(j,k)*ul(k)
        return
c calculate coordinates, gradients, fluxes, and forces
4 l=1
    if(nel.ge.4) l=2
    if(nel.ge.7) l=3
c get gauss points, if necessary
    if(dm.lt.0) then
        if(lint.gt.0.or.lint.ne.lchec(l)) call gaustri(l,lint,sg,tg,wg)
        else
            if(lint.lt.0.or.lint.ne.l*1) call gaus2d(l,lint,sg,tg,wg)
        endif
c loop over all gauss points
    do 420 i=1,nel
420      sat(i)=1/(1+d(3)*(d(7)-ul(i))**d(4))
        do 400 l=1,abs(lint)
            if(dm.gt.0) then
                call shape(sg(l),tg(l),xl,shp,xsj,ndm,nel,ix,.false.)
            else
                call shptri(sg(l),tg(l),xl,shp,xsj,ndm,nel,ix,.false.)
            endif
            if(xsj.lt.0) xsj=-xsj
c gradients

```

```

    do 430 i=1,4
430 eps(i)=0.
    do 440 j=1,nel
        eps(1)=eps(1)+shp(1,j)*ul(j)
        eps(2)=eps(2)+shp(2,j)*ul(j)
        eps(3)=eps(3)+shp(1,j)*sat(j)
440 eps(4)=eps(4)+shp(2,j)*sat(j)
c fluxes
    sig(1)=-d(1)*eps(1)
    sig(2)=-d(2)*eps(2)
    sig(3)=(sig(1)**2+sig(2)**2)**0.5
    sig(4)=90
    if(sig(1).ne.0) sig(4)=57.29578*atan(sig(2)/sig(1))
c nodal stresses loaded into ql array
    do 400 i=1,4
    do 400 j=1,nel
    if(nel.le.5) then
        ql(j,i)=ql(j,i)+tr51(l,j)*sig(i)
    elseif(nel.eq.6.and.dm.lt.0) then
        ql(j,i)=ql(j,i)+tr64(l,j)*sig(i)
    else
        ql(j,i)=ql(j,i)+tr84(l,j)*sig(i)
    endif
400 continue
    return
c put consistent mass in s, lumped mass in p
    5 l=1
    if(nel.ge.4) l=2
    if(nel.ge.7) l=3
c get gauss points, if necessary
    if(dm.lt.0) then
        if(lint.gt.0.or.lint.ne.lchec(l)) call gaustri(l,lint,sg,tg,wg)
    else
        if(lint.lt.0.or.lint.ne.l*1) call gaus2d(l,lint,sg,tg,wg)
    endif
    do 510 i=1,nel
510 dsdp(i)=d(5)*(d(7)-ul(i))**d(6)/((1+d(3))*(d(7)-ul(i))**d(4))**2)
c loop over all gauss points
    50 do 500 l=1,abs(lint)
    if(dm.gt.0) then
        call shape(sg(l),tg(l),xl,shp,xsj,ndm,nel,ix,.false.)
    else
        call shptri(sg(l),tg(l),xl,shp,xsj,ndm,nel,ix,.false.)
    endif
c check jacobian determinant
    if(xsj.gt.0) goto 54
    if(xsj.eq.0) then

```

```

prbwd=code(nn)
call ShowAlert(3,**Fatal Error: Element '//prbwd//
$      ' has a zero jacobian! Check it out.**')
call stopit
else
if(xsj.lt.0.and.l.eq.1) then
do 520 i=1,nel
520  xl(2,i)=-xl(2,i)
goto 50
else
prbwd=code(nn)
call ShowAlert(3,**Fatal Error: Element '//prbwd//'has a ch
$ange of sign of its jacobian in its interior! Check it out.**')
call stopit
endif
endif
c fill in upper triangular part of consistent mass
54 xsj=xsj*wg(1)*abs(dm)
do 500 j=1,nel
bn=shp(3,j)*xsj
do 500 k=1,nel
bnbn=bn*shp(3,k)
do 500 i=1,nel
500 s(j,k)=s(j,k)+bnbn*shp(3,i)*dsdp(i)
c lumped mass matrix
do 580 i=1,nel
do 580 j=1,nel
580 p(i)=p(i)+s(i,j)
return
c time step estimate
7 do 720 i=1,nel
720 avgdsdp=avgdsdp+d(5)*(d(7)-ul(i))**d(6)/
$      ((1+d(3))*(d(7)-ul(i))**d(4))**2)
avgdsdp=avgdsdp/nel
delx12sq=(xl(1,1)-xl(1,2))**2
dely12sq=(xl(2,1)-xl(2,2))**2
delx32sq=(xl(1,3)-xl(1,2))**2
dely32sq=(xl(2,3)-xl(2,2))**2
h12sq=delx12sq+dely12sq
h32sq=delx32sq+dely32sq
d12=(d(1)*delx12sq+d(2)*dely12sq)/h12sq
d32=(d(1)*delx32sq+d(2)*dely32sq)/h32sq
hsize1=h12sq/d12
hsize2=h32sq/d32
d(18)=avgdsdp*max(hsize1,hsize2)
return
c.... formats

```

```
1000 format(/5x,/  
$ 10x,'      x-diffusion ',2x,e14.6/  
$ 10x,'      y-diffusion ',2x,e14.6/  
$ 10x,'      alpha      ',2x,e14.6/  
$ 10x,'      n          ',2x,e14.6/  
$ 10x,'      shift      ',2x,e14.6/  
$ 10x,'      lamda     ',2x,e14.6/  
end
```

## CURRICULUM VITAE

January 1997

Name: Eric Luther Poole

Title: Ph. D. Candidate      Department of Aeronautics and Astronautics  
University of Washington

Address and Phone:      222 Cypress Point Drive  
Palm Beach Gardens, FL 33418, USA  
(561) 626-7993

Date and Place of Birth:      21 February 1968  
Kailua, Hawaii, USA

### Education:

Name of Institution	Location	From-To	Degree	Date
Renssalaer Poly. Inst.	Troy, NY	8/86-6/88	none	-
U. of Florida	Gainesville, FL	8/88-6/91	B. A.	6/91
U. of Florida	Gainesville, FL	8/88-6/91	B. S.	12/91
U. of Washington	Seattle, WA	9/91-6/93	M. S.	6/93
U. of Washington	Seattle, WA	6/93-12/96	Ph. D.	12/96

### Major Subjects:

Undergraduate:      Aerospace Engineering, Russian Language  
Graduate:      Structural Mechanics  
Doctoral Thesis:      Durability of Composite Structures

### Publications:

Poole, E. L. and Lin, K. Y., "Effects of Isothermal Aging on the Toughness of Polymeric Composite Materials," Proceedings of ICCM-10, Whistler B.C., Canada, August 1995.

Poole, E. L., Lin, K. Y. and Backman, B. F., "Effects of Aging on Compressive strength of Composites after Impact," Proceedings of 35th SDM, Hilton Head, SC, April 1994.